



Calhoun: The NPS Institutional Archive DSpace Repository

Theses and Dissertations

1. Thesis and Dissertation Collection, all items

2004-09

Optimal trajectory reconfiguration and retargeting for the X-33 reusable launch vehicle

Shaffer, Patrick J.

Monterey California. Naval Postgraduate School

<http://hdl.handle.net/10945/1347>

This publication is a work of the U.S. Government as defined in Title 17, United States Code, Section 101. Copyright protection is not available for this work in the United States.

Downloaded from NPS Archive: Calhoun



<http://www.nps.edu/library>

Calhoun is the Naval Postgraduate School's public access digital repository for research materials and institutional publications created by the NPS community.

Calhoun is named for Professor of Mathematics Guy K. Calhoun, NPS's first appointed -- and published -- scholarly author.

**Dudley Knox Library / Naval Postgraduate School
411 Dyer Road / 1 University Circle
Monterey, California USA 93943**



**NAVAL
POSTGRADUATE
SCHOOL**

MONTEREY, CALIFORNIA

THESIS

**OPTIMAL TRAJECTORY RECONFIGURATION AND
RETARGETING FOR THE X-33 REUSABLE
LAUNCH VEHICLE**

by

Patrick J. Shaffer

September 2004

Thesis Advisor:
Second Reader:

I. Michael. Ross
David B. Doman

Approved for public release; distribution is unlimited

THIS PAGE INTENTIONALLY LEFT BLANK

REPORT DOCUMENTATION PAGE

Form Approved OMB No. 0704-0188

Public reporting burden for this collection of information is estimated to average 1 hour per response, including the time for reviewing instruction, searching existing data sources, gathering and maintaining the data needed, and completing and reviewing the collection of information. Send comments regarding this burden estimate or any other aspect of this collection of information, including suggestions for reducing this burden, to Washington headquarters Services, Directorate for Information Operations and Reports, 1215 Jefferson Davis Highway, Suite 1204, Arlington, VA 22202-4302, and to the Office of Management and Budget, Paperwork Reduction Project (0704-0188) Washington DC 20503.

1. AGENCY USE ONLY (Leave blank)	2. REPORT DATE	3. REPORT TYPE AND DATES COVERED
	September 2004	Master's Thesis
4. TITLE AND SUBTITLE: Optimal Trajectory Reconfiguration And Retargeting For The X-33 Reusable Launch Vehicle.		5. FUNDING NUMBERS
6. AUTHOR(S) Patrick J. Shaffer, CDR, USN		
7. PERFORMING ORGANIZATION NAME(S) AND ADDRESS(ES) Naval Postgraduate School Monterey, CA 93943-5000		8. PERFORMING ORGANIZATION REPORT NUMBER
9. SPONSORING /MONITORING AGENCY NAME(S) AND ADDRESS(ES) AFRL/VACA Wright Patterson AFB, OH		10. SPONSORING/MONITORING AGENCY REPORT NUMBER
11. SUPPLEMENTARY NOTES The views expressed in this thesis are those of the author and do not reflect the official policy or position of the Department of Defense or the U.S. Government.		
12a. DISTRIBUTION / AVAILABILITY STATEMENT Approved for public release; distribution is unlimited		12b. DISTRIBUTION CODE
13. ABSTRACT (maximum 200 words) This thesis considers the problem of generating optimal entry trajectories for a reusable launch vehicle following a control surface failure. The thesis builds upon the work of Dr. David Doman, Dr. Michael Oppenheimer and Dr. Michael Bolender of the Air Vehicles Directorate, Air Force Research Lab Dayton Ohio. The primary focus of this work is to demonstrate the feasibility of inner loop reconfiguration and outer loop trajectory retargeting and replanning for the X-33 reusable launch vehicle (RLV) following the imposition of a control surface failure. The trajectory generation model employs path constraints generated by an AFRL trim deficiency algorithm coupled with an inner loop control allocator and aerodynamic database that captures the full 6-DOF vehicle aerodynamic effects while utilizing an outer loop 3-DOF model. The resulting optimal trajectory does not violate the trim deficiency constraints and provides additional margins for trajectories flown during failure conditions. The footprints generated by the thesis show that contemporary footprint analysis for vehicles experiencing control surface failures are overly optimistic when compared to those footprints that consider vehicle aerodynamic stability and realistic landable attitudes at the threshold of the landing runway. The results of the thesis also show the performance reductions resulting from decoupling the inner and outer loop and that trajectories can be generated to the landing runway without using a region of terminal area energy management.		
14. SUBJECT TERMS Reentry, X-33, Trajectory, Optimal, Replanning, Retargeting		15. NUMBER OF PAGES 151
16. PRICE CODE		
17. SECURITY CLASSIFICATION OF REPORT Unclassified	18. SECURITY CLASSIFICATION OF THIS PAGE Unclassified	19. SECURITY CLASSIFICATION OF ABSTRACT Unclassified
20. LIMITATION OF ABSTRACT UL		

THIS PAGE INTENTIONALLY LEFT BLANK

Approved for public release; distribution is unlimited

**OPTIMAL TRAJECTORY RECONFIGURATION AND RETARGETING FOR
THE X-33 REUSABLE LAUNCH VEHICLE**

Patrick J. Shaffer
Commander, United States Navy
B.S., Old Dominion University, 1988

Submitted in partial fulfillment of the
requirements for the degrees of

**ASTRONAUTICAL ENGINEER
AND
MASTER OF SCIENCE IN ASTRONAUTICAL ENGINEERING**

from the

**NAVAL POSTGRADUATE SCHOOL
September 2004**

Author: Patrick J. Shaffer

Approved by: I. M. Ross
Thesis Advisor

David B. Doman
Second Reader/Co-Advisor

Anthony J. Healey
Chairman, Department of Mechanical and Astronautical
Engineering

THIS PAGE INTENTIONALLY LEFT BLANK

ABSTRACT

This thesis considers the problem of generating optimal entry trajectories for a reusable launch vehicle following control surface failures. The thesis builds upon the work of Dr. David Doman, Dr. Michael Oppenheimer and Dr. Michael Bolender of the Air Vehicles Directorate, Air Force Research Lab Dayton Ohio. The primary focus of this work is to demonstrate the feasibility of inner loop reconfiguration and outer loop trajectory retargeting and replanning for the X-33 reusable launch vehicle (RLV) following the imposition of a control surface failure. The trajectory generation model employs path constraints generated by an AFRL trim deficiency algorithm coupled with an inner loop control allocator and aerodynamic database that captures the full 6-DOF vehicle aerodynamic effects while utilizing an outer loop 3-DOF model. The resulting optimal trajectory does not violate the trim deficiency constraints and provides additional margins for trajectories flown during failure conditions. The footprints generated by the thesis show that contemporary footprint analysis for vehicles experiencing control surface failures are overly optimistic when compared to those footprints that consider vehicle aerodynamic stability and realistic landable attitudes at the threshold of the landing runway. The results of the thesis also show the performance reductions resulting from decoupling the inner and outer loop and that trajectories can be generated to the landing runway without using a region of terminal area energy management.

THIS PAGE INTENTIONALLY LEFT BLANK

TABLE OF CONTENTS

I.	INTRODUCTION	1
	A. HISTORICAL BACKGROUND.....	1
	B. THE X-33 PROGRAM.....	2
	1. X-33 Mission Description	3
	2. X-33 Vehicle Description.....	5
	C. IMPLICATIONS OF CONTROL SURFACE FAILURES	7
II.	APPROACH.....	9
	A. GENERAL APPROACH DISCUSSION.....	9
	B. REDUCED-ORDER DYNAMICAL MODEL.....	9
	1. Coordinate Systems	9
	2. Equations of Motion	10
	a. <i>Kinematics</i> :.....	10
	b. <i>Dynamics</i> :.....	10
	3. The State Vector.....	12
	4. The Control Vector	12
	C. 4-DOF MODEL.....	13
	D. ATMOSPHERIC MODEL	14
	E. GRAVITATIONAL MODEL.....	16
	F. X-33 AERODYNAMIC MODEL.....	16
	1. Mach Breakpoints.....	17
	2. AFRL PLP Control Allocation Model	17
	3. Trajectory Replanning Algorithm.....	20
	4. Failure Mode	21
	5. Failure Mode Effects.....	21
	6. Modeling Trim Deficiency.....	25
III.	THE OPTIMAL CONTROL PROBLEM.....	29
	A. OPTIMAL CONTROL THEORY	29
	1. Preliminaries	29
	2. Solution Methodology	31
	3. DIDO	32
	4. Optimality	32
	5. Feasibility.....	33
	6. Scaling and Balancing	33
	B. REENTRY VIEWED AS AN OPTIMAL CONTROL PROBLEM	35
IV.	APPLICATIONS	39
	A. FOOTPRINT DETERMINATION.....	39
	B. LANDING AT A SPECIFIC FIELD WITHIN THE FOOTPRINT	39
V.	RESULTS	43
	A. DISCUSSION	43
	B. FOOTPRINT ANALYSIS FOR NOMINAL AND STUCK FLAP TRAJECTORIES	44

1.	Aerodynamic Considerations.....	44
2.	Footprint Observations and Conclusions	45
3.	Maximum Downrange	47
	a. <i>Mach-Altitude Profile</i>	48
	b. <i>Trajectory in Cartesian Coordinates</i>	48
	c. <i>Velocity Profiles</i>	52
	d. <i>Flight Path and Azimuth Angle</i>	52
	e. <i>Vertical Speed Profile</i>	55
	f. <i>Body Frame Normal Force</i>	55
	g. <i>Controls</i>	58
	h. <i>Pseudo Controls</i>	59
	i. <i>Trim Deficiency</i>	61
	j. <i>Optimality Analysis</i>	61
	k. <i>Feasibility</i>	66
4.	Minimum Downrange.....	67
	a. <i>Mach-Altitude Profile</i>	67
	b. <i>Trajectory in Cartesian Coordinates</i>	67
	c. <i>Velocity Profile</i>	71
	d. <i>Flight Path and Azimuth Angle</i>	72
	e. <i>Vertical Speed Profile</i>	74
	f. <i>Body Frame Normal Force</i>	76
	g. <i>Controls</i>	78
	h. <i>Pseudo Controls</i>	79
	i. <i>Trim Deficiency</i>	80
	j. <i>Optimality Analysis</i>	81
	k. <i>Feasibility</i>	84
5.	Minimum /Maximum Crossrange.....	85
	a. <i>Mach-Altitude Profile</i>	85
	b. <i>Trajectory in Cartesian Coordinates</i>	86
	c. <i>Velocity Profile</i>	88
	d. <i>Flight Path and Azimuth Angles</i>	89
	e. <i>Vertical Speed Profiles</i>	90
	f. <i>Normal Force Profiles</i>	91
	g. <i>Controls</i>	92
	h. <i>Pseudo Controls</i>	93
	i. <i>Trim Deficiency</i>	94
	j. <i>Optimality Analysis</i>	95
	k. <i>Feasibility</i>	97
C.	TRAJECTORY TO A SPECIFIED FIELD.....	97
1.	Endpoint Conditions and Cost Function	97
2.	Profiles for a Failure-Mode Trajectory to a Specified Field.....	99
	a. <i>Mach-Altitude Profile</i>	99
	b. <i>Trajectory in Cartesian Coordinates</i>	100
	c. <i>Velocity Profile</i>	105
	d. <i>Flight Path and Azimuth Angle</i>	106

e.	<i>Body Frame Normal Force</i>	107
f.	<i>Vertical Speed Profile</i>	109
g.	<i>Controls</i>	111
h.	<i>Pseudo Controls</i>	112
i.	<i>Trim Deficiency</i>	114
j.	<i>Optimality Analysis</i>	115
k.	<i>Feasibility Analysis</i>	119
D.	DIDO PERFORMANCE	120
V.	FUTURE WORK	125
A.	CONVERSION TO SI UNITS	125
B.	DATA SMOOTHING	125
C.	TRIM DEFICIENCY MAPPING	125
D.	CLOSED LOOP IMPLEMENTATION	126
E.	OPTIMIZING THE DIDO CODE FOR SPEED	126
F.	FULL 6-DOF MODEL WITH INNER AND OUTER LOOP COUPLING	126
LIST OF REFERENCES		127
INITIAL DISTRIBUTION LIST		131

THIS PAGE INTENTIONALLY LEFT BLANK

LIST OF FIGURES

Figure 1	X-33 Flight Phases (from Ref. 5).....	4
Figure 2	Representative X-33 Mission Profiles (from Ref. 5).....	5
Figure 3	X-33 Vehicle Depiction (from Ref 1)	6
Figure 4	X-33 Simulation Coordinate System	10
Figure 5	Trajectory Optimization Feasibility Error Estimation	14
Figure 6	Plot of Density vs. Altitude (from AFRL atmosphere model).....	15
Figure 7	Plot of Speed of Sound vs. Altitude (from AFRL atmosphere model).....	16
Figure 8	AFRL Control Allocator	20
Figure 9	Trajectory Replanning	21
Figure 10	X-33 Trimmable Values for Angle of Attack.(from Ref 19.).....	22
Figure 11	X-33 Trimmable Values of Angle of Attack following a Dual Stuck Flap Failure (failed at 26 degrees up). (from Ref. 19).	23
Figure 12	X-33 Pitch Deficiency Following a Stuck Right Rudder (15 degrees).....	24
Figure 13	X-33 Pitch Deficiency Following a Stuck Flap (at -15 degrees).....	25
Figure 14	Table Curve 3D Trim Deficiency Data for a Dual Stuck Flap Failure (26 degrees).....	26
Figure 15	Trim Deficiency Fitted with 10th order Chebyshev Polynomial.....	27
Figure 16	Comparison of Nominal and Stuck-Flap (+26°) Footprints	46
Figure 17	Contraction of Failure Stuck-Flap (+26°) Trajectory Footprint	47
Figure 18	Maximum Downrange Mach-Altitude Profile.....	48
Figure 19	Downrange Profile for Maximum Downrange Trajectories.....	49
Figure 20	Cross Range Profiles for Maximum Downrange Trajectories.....	50
Figure 21	Terminal Maneuver for Max Downrange Trajectories.....	51
Figure 22	Altitude Profiles for Max Downrange Trajectories	51
Figure 23	Velocity Profiles for Max Downrange Trajectories.....	52
Figure 24	Flight Path Angle Profiles for Max Downrange Trajectories	53
Figure 25	Azimuth Angle Profile for Max Downrange Trajectories	54
Figure 26	Vertical Speed Profiles for Nominal and Failed Trajectories (Max Downrange).....	55
Figure 27	Normal Force ($n_z - 1$) vs. Time for Vehicle with Stuck Flaps.....	56
Figure 28	Normal Force ($n_z - 1$) vs. Downrange Distance for Vehicle with Stuck Flaps.....	56
Figure 29	Normal Force ($n_z - 1$) vs. Time for Nominal Vehicle	57
Figure 30	Delta Normal Force($n_z - 1$) vs. Downrange Distance for Nominal Vehicle ..	57
Figure 31	Angle of Attack Profiles for Max Downrange Trajectories.....	58
Figure 32	Bank Angle Profiles for Max Downrange Trajectories	59
Figure 33	Angle of Attack Rate Profiles for Maximum Downrange Trajectories	60
Figure 34	Bank Angle Rate Profiles for Maximum Downrange Trajectories	60
Figure 35	Trim Deficiency Map for Max Downrange Trajectories	61
Figure 36	Hamiltonian for Max Downrange Nominal Trajectory	62

Figure 37	Hamiltonian for Vehicle with (26 deg) Stuck Flaps	63
Figure 38	Constrained Pseudo Controls for (26 deg) Stuck Flap Trajectory	63
Figure 39	Upper and Lower Bounded Bank Angle Rate for (26 degree) Stuck Flap Trajectory	64
Figure 40	Bank Angle Rate and Associated Dual for (26 deg) Stuck Flap Trajectory	65
Figure 41	Angle of Attack Rate and Associated Dual for (26 degree) Stuck Flap Trajectory	65
Figure 42	DIDO and Propagated Controls (DIDO controls are denoted by discrete points)	66
Figure 43	Mach-altitude Profiles for Minimum Downrange Trajectory	67
Figure 44	Downrange Distance Profiles for Minimum Downrange Trajectories	68
Figure 45	Crossrange Profiles for Minimum Downrange Trajectories	69
Figure 46	Altitude Profile for Minimum Downrange Trajectories	70
Figure 47	Terminal Altitude Maneuver for Minimum Downrange Trajectories	70
Figure 48	Velocity Profiles for Minimum Downrange Trajectories	71
Figure 49	Terminal Velocity Profile for Minimum Downrange Trajectories	72
Figure 50	Flight Path Angle Profile for Min Downrange Trajectories	73
Figure 51	Azimuth Angle Profile for Min Downrange Trajectories	73
Figure 52	Vertical Speed Profiles (vs. Downrange Distance) for Minimum Downrange Trajectories	74
Figure 53	Vertical Speed Profiles (vs. time) for Nominal and Failed Trajectories, Minimum Downrange	75
Figure 54	Body Frame Normal Force ($n_z - 1$), Stuck Flap Minimum Downrange Trajectory	76
Figure 55	Body Frame Normal Force ($n_z - 1$), Nominal Minimum Downrange Trajectory	77
Figure 56	Angle of Attack Profile, Minimum Downrange Trajectories	78
Figure 57	Bank Angle Profile, Minimum Downrange Trajectories	78
Figure 58	Angle of Attack Rate Profile, Minimum Downrange Trajectories	79
Figure 59	Bank Angle Profile, Minimum Downrange Trajectories	79
Figure 60	Trajectory Trim Deficiencies, Minimum Downrange Trajectories	80
Figure 61	Hamiltonian for Nominal Minimum Downrange Trajectory	81
Figure 62	Constrained Flight Path Angle and Associated Dual, Nominal Minimum Downrange Trajectory	82
Figure 63	Constrained Angle of Attack Rate and Associated Dual, Nominal Minimum Downrange Trajectory	82
Figure 64	Hamiltonian for Stuck Flap, Minimum Downrange Trajectory	83
Figure 65	Constrained Flight Path Angle and Associated Dual, Stuck Flap Minimum Downrange Trajectory	83
Figure 66	Constrained Angle of Attack Rate and Associated Dual, Stuck Flap Minimum Downrange Trajectory	84
Figure 67	DIDO and Propagated Controls for Stuck Flap, Minimum Downrange Trajectory (DIDO controls are denoted by discrete points)	85
Figure 68	Downrange Distance Profiles for Maximum Crossrange Trajectories	86
Figure 69	Downrange Distance Profile for Maximum Crossrange Trajectories	87

Figure 70	Crossrange Distance Profile for Maximum Crossrange Trajectories	87
Figure 71	Altitude Profile for Maximum Crossrange Trajectories	88
Figure 72	Velocity Profile for Maximum Crossrange Trajectories	88
Figure 73	Flight Path Angle Profile for Maximum Crossrange Trajectories.....	89
Figure 74	Azimuth Angle Profile for Maximum Crossrange Trajectories	89
Figure 75	Vertical Speed Profiles for Maximum Crossrange Trajectories	90
Figure 76	Normal Force ($n_z - 1$) for Nominal Maximum Crossrange Trajectory.....	91
Figure 77	Normal Force($n_z - 1$) for Stuck Flap, Maximum Crossrange Trajectory	91
Figure 78	Angle of Attack Profile for Maximum Crossrange Trajectories	92
Figure 79	Bank Angle Profile for Maximum Crossrange Trajectories	92
Figure 80	Angle of Attack Rate Profile for Maximum Crossrange Trajectories	93
Figure 81	Bank Angle Rate Profiles for Maximum Crossrange Trajectories	93
Figure 82	Trim Deficiencies for Maximum Crossrange Trajectories	94
Figure 83	Hamiltonian for Stuck Flap, Maximum Crossrange Trajectory	95
Figure 84	Hamiltonian for Nominal Maximum Crossrange Trajectory.....	95
Figure 85	Bank Angle Rate and Dual for Stuck Flap Max Crossrange Trajectory.....	96
Figure 86	DIDO and Propagated Controls for Stuck Flap Max Crossrange Trajectory (DIDO controls are denoted by discrete points)	97
Figure 87	Mach-altitude Profile for Stuck Flap Trajectory to Specified Field	99
Figure 88	Downrange Profile for Stuck Flap Trajectory to Specified Field (Flaps Stuck at 26 degrees).....	100
Figure 89	Crossrange Profile for Stuck Flap Trajectory to Specified Field (Flaps Stuck at 26 degrees).....	101
Figure 90	Altitude Profile for Stuck Flap Trajectory to Specified Field.....	101
Figure 91	Three Dimensional Trajectory Depiction (not to scale) for Failed Vehicle (Flaps Stuck at 26 degrees).....	102
Figure 92	Quiver Plot (not to scale) for Failed Vehicle Trajectory to Specified Field (Flaps Stuck at 26 degrees).....	103
Figure 93	Ground Track Plot (not to scale) of Failed Vehicle Trajectory to Specified Field (Flaps Stuck at 26 degrees).....	104
Figure 94	Velocity Profile for Failed Vehicle Trajectory to Specified Field.....	105
Figure 95	Flight Path Angle Profile for Failed Vehicle Trajectory to a Specified Field	106
Figure 96	Azimuth Angle Profile for Failed Vehicle Trajectory to a Specified Field...106	
Figure 97	Normal Force($n_z - 1$) and Angle of Attack Profile for Failed Vehicle Trajectory to Specified Field	107
Figure 98	Normal Force($n_z - 1$) and Angle of Bank Profile for Failed Vehicle Trajectory to Specified Field	108
Figure 99	Vertical Speed Profile for Failed Vehicle Trajectory to Specified Field.....109	
Figure 100	Vertical Speed Profile (vs. time) for Failed Vehicle Trajectory to Specified Field	110
Figure 101	Angle of Attack Profile for Failed Vehicle Trajectory to Specified Field.....111	
Figure 102	Angle of Bank Profile for Failed Vehicle Trajectory to Specified Field.....111	

Figure 103	Angle of Attack Rate Profile for Failed Vehicle Trajectory to Specified Field	112
Figure 104	Bank Angle Rate for Failed Vehicle Trajectory to Specified Field.....	113
Figure 105	Trim Deficiency Profile for Failed Vehicle Trajectory to Specified Field....	114
Figure 106	Hamiltonian for Failed Vehicle Trajectory to Specified Field (Flaps Stuck at 26 degrees)	115
Figure 107	FPA and Associated Dual for Failed Vehicle Trajectory to Specified Field (Flaps Stuck at 26 degrees).....	116
Figure 108	Bank Angle Rate and Associated Dual for Failed Vehicle Trajectory to Specified Field (Flaps Stuck at 26 degrees).....	117
Figure 109	Angle of Attack Rate and Associated Dual for Failed Vehicle Trajectory to Specified Field (Flaps Stuck at 26 degrees).....	118
Figure 110	Scaled DIDO and Propagated States, Failed Vehicle Trajectory to Specified Field (DIDO controls are denoted by discrete points).....	119
Figure 111	Downrange and Crossrange Error, Nominal Trajectory	121
Figure 112	Altitude Error vs. Nodes	121
Figure 113	Time to Reach a Solution, Nominal Trajectory for Pentium 4, 2.0 Ghz processor using Windows 2000.....	122
Figure 114	Convergence of Down and Cross Ranges for Near Optimal Solutions	123
Figure 115	Altitude Convergence for Near Optimal Trajectory	123

LIST OF TABLES

Table 1.	Flight Test Trajectory Matrix (from Ref. 5)	5
Table 2.	Numerical Trim Deficiency Constraint Results for 80 nodal Points	115

THIS PAGE INTENTIONALLY LEFT BLANK

ACKNOWLEDGMENTS

One of the very first things I remember as a child was the television feed from the Apollo landing on the moon. From then on, I wanted to be an astronaut. But as time and chance happen along the way, I never got to the stars but am perfectly satisfied with being a Naval Flight Officer for the last 14 years. I am grateful to the United States Navy and to the taxpayers that fund the Naval Postgraduate School for the opportunity to study the science and art of Space Systems Engineering.

My faith in God has sustained me throughout the years but I would not have been able to achieve the tiniest of success without the support from my family, friends and colleagues who I note below.

To my father, Joe Shaffer, who inspired me to fly Navy. All the countless hours I spent as a boy looking through cruise books from aircraft carriers with names like Intrepid, Forrestal and Independence helped fuel my desire to become a member of naval aviation. My father continues to inspire me by showing that it is the hard work and the character of a man that is best remembered and not the credentials he carries,

To my mother who nurtured me and gave me unconditional love while holding down the house while my father was away at sea longer than he was home.

To my wife Denise, who said she'd follow me wherever I went (and she did). You are my partner, friend, confidant and without your support I would have never made it this far. The job of a Navy wife is not easy although you made it look so. Thank you for holding down the fort and for being an exceptional mother to our four children.

To Mike Ross – you are the Buddha. Your tutelage, patience, optimism and talent are infectious. Thank you for all of your time explaining simple things to knuckleheads like me. And yes – I too now view life as an optimal control problem.

To Dave Doman and Mike Oppenheimer of the Air Force Research lab in Dayton, thanks for giving me your valuable time and sharing your expertise to help me understand complex concepts. It was a pleasure working with you and I hope that our paths will cross again in the near future.

THIS PAGE INTENTIONALLY LEFT BLANK

I. INTRODUCTION

A. HISTORICAL BACKGROUND

As early as 1931, Dr. Eugen Sänger conceived of an aerovehicle that could achieve low-earth orbit (LEO) and return to earth like a glider. The Sänger Silverbird was advocated as a hypersonic vehicle that could deliver an 8300 pound payload into LEO and return to earth in an unpowered glide. Alternatively, the Silverbird (or its military incarnation, the Amerika Bomber) could deploy a 1600-pound payload into a suborbital trajectory from a launch point halfway around the globe and return to its origination by skip-gliding or dynamic soaring [ref 25].

The problem of extreme reentry heating was severely underestimated by Sänger and conclusions from NACA Ames reentry studies in the 1950's led to the abandonment of skip gliding or dynamic soaring because there was no contemporary technological solution to mitigate the severe heating during reentry. Later manned missions such as Apollo overcame the reentry heating problem by employing a vehicle that used an ablative heat shield to protect the payload and followed a steep ballistic reentry trajectory. Unfortunately this type of technology, while effective, did not allow for reusable vehicles.

Interest in reusable spacecraft resulted in the development of the space shuttle which makes use of advanced materials and controls technologies to fly trajectories which keep the shuttle within a very narrow reentry corridor to limit the heating and dynamic pressure effects of the entry trajectory thereby ensuring a successful landing [ref. 22]. These reentry trajectories are computed offline for a variety of initial conditions and then stored in the shuttle's computer where they can then be accessed by the guidance computer. The generation of these trajectories represents a significant effort and is supported by a large body of work from contemporary optimal control research.

Reusable launch vehicles are being pursued as a low-cost alternative to expendable launch vehicles and the shuttle. The concept of a reusable launch vehicle that can achieve LEO using a single stage is seen as a technology that can significantly reduce

the cost of access to space as well as improving the frequency of access to space. The employment of autonomous, reusable launch vehicles requires additional control robustness to replace the human's place in the loop. The guidance and control of these autonomous reusable launch vehicles mandate new guidance strategies that are able to identify and adapt to vehicle failures during the trajectory and still return to earth safely.

An important class of failures that concern reentry trajectories are those control surface failures which affect the vehicle's aerodynamic characteristics and controllability. The nominal reentry trajectories are designed assuming the vehicle's original aerodynamic characteristics and can no longer be assumed valid following a control surface failure. The challenge is to reconfigure the inner loop control algorithm, determine the new aerodynamic characteristics of the failed vehicle and to generate a new trajectory using the new aerodynamic data to direct the vehicle to a landing point using a modified performance criterion.

This thesis demonstrates the application of a pseudospectral method to determine the optimal entry trajectory for the X-33 for nominal conditions as well as for off-nominal conditions caused by vehicle control surface failures. Actual X-33 aerodynamic data is used in a reduced-order dynamical model to generate the trajectories. Feasibility, optimality and various performance metrics of the pseudospectral approach are investigated and quantified.

B. THE X-33 PROGRAM

The X-33 was a half-scale technology demonstrator of a potential future Reusable Launch Vehicle (RLV) [ref 24]. The prime contractor for the 1.2 billion dollar program was Lockheed Martin who called the full-scale vehicle VentureStar. The X-33 was to provide data that would lead to the full development of a single stage to orbit (SSTO) vehicle that would dramatically lower the cost of access to space through SSTO and minimal time between missions. The X-33 represented cutting edge technology in all design aspects, from its linear aerospike engines to its composite fuel tanks. The vehicle can reach altitudes of 50 miles and hypersonic speeds. The design turn around time for this vehicle was 7 days with an eventual turn around goal of two days. The program was

expected to begin full flight demonstration in 1999 but was discontinued in 2001 after technology maturation difficulties. The X-33 remains a desirable vehicle to study because of the large amount of performance data available and because of its multiple redundant control surfaces allows for the investigation of a considerable variety of recoverable control surface failures and their impacts upon entry trajectories.

1. X-33 Mission Description

The X-33 was designed to demonstrate the ability to carry a small payload to low earth orbit, return safely to earth, and undergo minimal preparations in order to be ready for another mission. The vehicle was to be launched from Edwards Air Force Base and is potentially recoverable at a number of suitable fields. The proposed flight test program utilized several ascent trajectory profiles terminating at Malstrom Air Force Base, Montana or Michael Army Air Field, Utah.

The typical X-33 mission begins with a powered ascent that achieves a given Mach and altitude at main engine cutoff (MECO). The vehicle performs some activity on orbit, transitions and enters the atmosphere passing through several intermediate flight stages ultimately ending at landing and rollout. Figure 1 details the various X-33 mission phases as well as the effectors that are used to control the vehicle. While Figure 1 shows a reaction control system (RCS) available during the entry phase, this thesis assumes that no RCS present during the entry portion of the mission. The weight on wheels (WOW) and rollout mission phase are not considered in the trajectory generation.

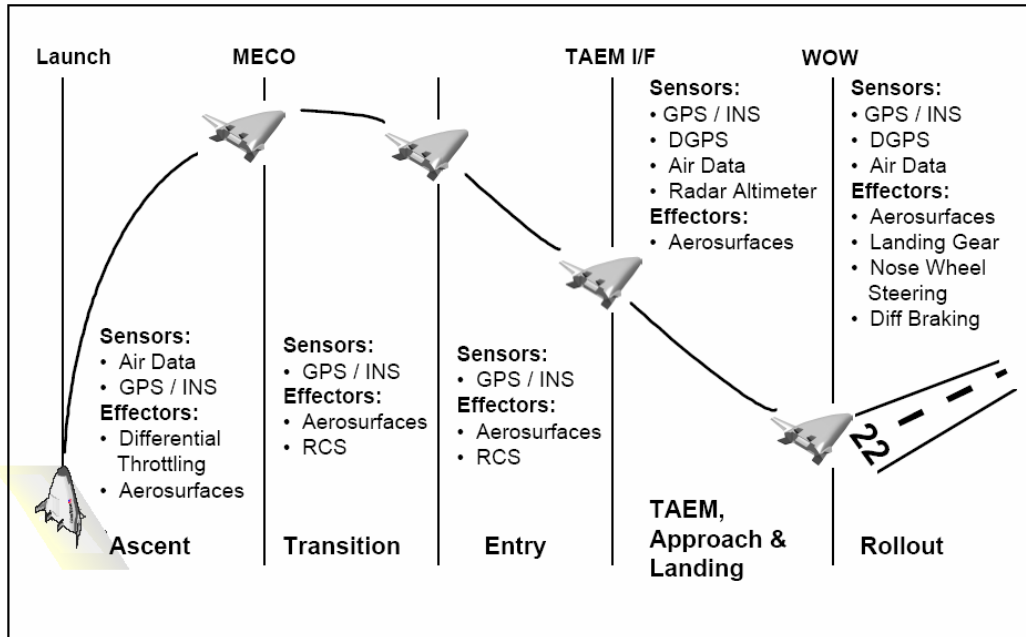


Figure 1 X-33 Flight Phases (from Ref. 5)

Figure 2 depicts typical X-33 mission profiles with recoveries at both fields. Notice that the ascent profiles and the entry initial conditions differ significantly for each mission.

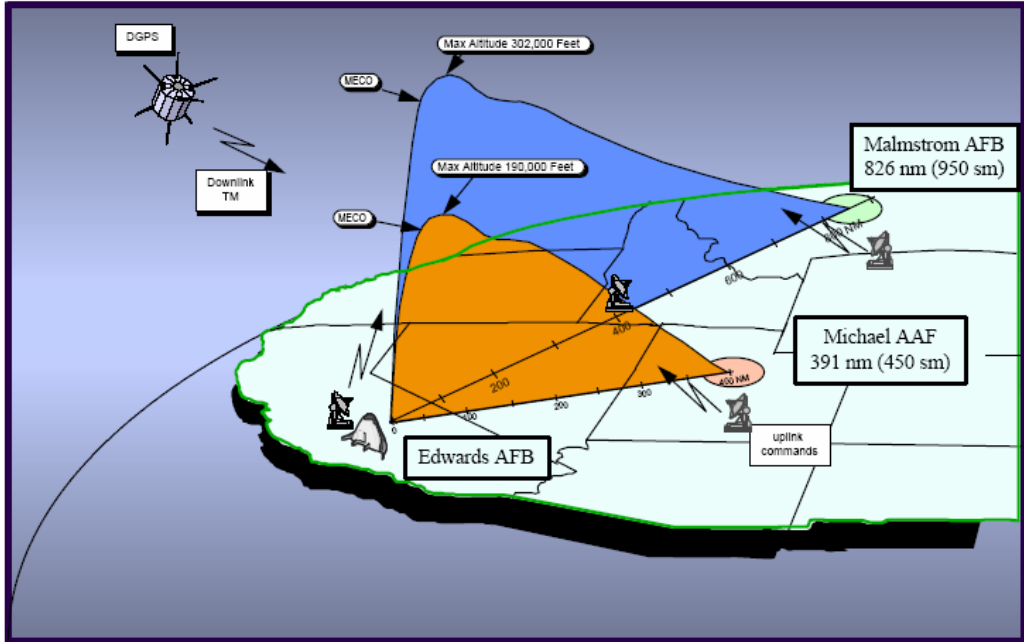


Figure 2 Representative X-33 Mission Profiles (from Ref. 5)

A partial list of mission profiles is shown in Table 1. The Mach number and maximum altitude are used as initial conditions for the trajectory optimization routines.

Flight No.	Trajectory Designation	Landing Site	Dist nm	Mach No.	Max Alt. k Feet	Time MECO	asmg	Q	Q Alpha	Heat Rate	Test Objectives
1	9a-2 Benign	Michael	391	8.84	186	239	4.11	196	4864	17.27	Aero plume interactions, Structural interactions, Thrust Vector Control Verification Installed Isp
2	9d-1 Transition	Michael	391	10.66	186	197	4.11	404	6286	24.14	Shock-Shock interactions Boundary layer transition
3	7b-1 Max Heating	Michael	391	8.97	189	221	4.11	239	6576	27.29	TPS panel thermal properties Aircraft-Like Operational Efficiency
4	9c-2 Real Gas	Michael	391	10.21	189	204	4.11	399	6006	22.12	Real Gas Effects Verification Aircraft-Like Operational Efficiency Verification 48 hour turn-around
5*	7b-1 Max Heating	Michael	391	8.97	189	221	4.11	239	6576	27.29	TPS panel thermal properties / support structure
6	7d Real Gas	Malmstrom	826	12.64	302	208	4.03	342	7080	37.05	Real Gas Effects Verification - Surface catalysis with atomic oxygen
7*	7d Real Gas	Malmstrom	826	12.64	302	208	4.03	342	7080	37.05	- Effects on pitch moment
8-15	As Required	Michael / Malmstrom	391/ 826								Repeat flights as required to acquire additional data

Table 1. Flight Test Trajectory Matrix (from Ref. 5)

2. X-33 Vehicle Description

The X-33 is a lifting body with four sets of aerosurfaces: rudders, body flaps, and inboard and outboard elevons. The vehicle also has a reaction control system (RCS) for use in unpowered flight at low dynamic pressure. For powered flight, the vehicle uses

aerospike engines with thrust vectoring for pitch and roll control and differential thrust for yaw control [ref 28]. Figure 3 depicts the general X-33 configuration and identifies the vehicle's control surfaces.

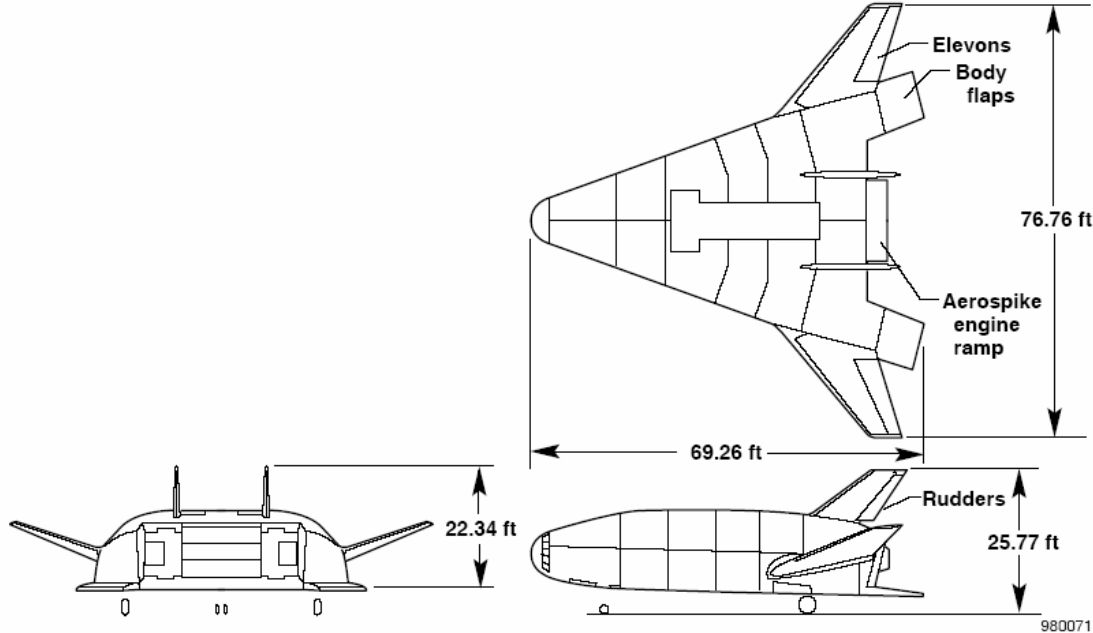


Figure 3 X-33 Vehicle Depiction (from Ref 1)

The vehicle gross liftoff weight is 280,000 pounds. The vehicle weight after MECO is approximately 78,000 pounds.

The control surfaces deflection vector, also known as the effector vector, is identified by the Greek letter δ whose elements are identified as

$$\delta = [\text{Relevon}_{\text{in}} \quad \text{Relevon}_{\text{out}} \quad \text{Lelevon}_{\text{in}} \quad \text{Lelevon}_{\text{out}} \quad \text{Flap}_R \quad \text{Flap}_L \quad \text{Rudder}_R \quad \text{Rudder}_L]^T \quad (1.1)$$

The X-33 control surfaces have maximum and minimum deflections in degrees as shown by the vectors below:

$$\delta_{\text{min}} = [-30 \quad -30 \quad -30 \quad -30 \quad -15 \quad -15 \quad -60 \quad -30]^T \quad (1.2)$$

$$\delta_{\text{max}} = [30 \quad 30 \quad 30 \quad 30 \quad 26 \quad 26 \quad 30 \quad 60]^T \quad (1.3)$$

Locked control surface failures are modeled by replacing elements of (1.2) and (1.3) that correspond to the failed surfaces, with the positions of the failed surfaces.

C. IMPLICATIONS OF CONTROL SURFACE FAILURES

Many published works deal with the subject of reconfigurable control following a control surface failure of the vehicle at some point in its mission. The significance of reconfigurable control is that it allows the inner loop to compensate for the changed aerodynamics of the vehicle and maintain controllability. For many cases, reconfigurable inner loop control is insufficient to continue safe flight and a new trajectory based on knowledge of the type of failure and the resulting changes in the constraints on the state, cost, control and path arguments to the optimal trajectory problem must be computed. The replanned trajectory has the ability to continue the mission from the point of failure and on to landing thus saving the vehicle and crew which would have otherwise been lost as a result of the failure. The availability of an online algorithm such as the AFRL trim deficiency algorithm provides the outer loop with the feasible range of Mach and angle of attack combinations *throughout the trajectory* as well as the full 6-DOF effects of the X-33 aerodynamic model for use in coefficients of lift and drag calculations for the *remainder of the trajectory*.

The thesis model uses a pseudospectral method to determine the optimal entry trajectory subject to appropriate constraints such as normal load and trim deficiency. The approach assumes online identification of the failure. Following the failure identification and characterization, the new effector vectors containing the upper and lower control surface bounds are passed to the trim deficiency algorithm which determines the new feasible ranges of Mach number and angle of attack as well as optimized effector displacement vectors for given Mach-dependent angle of attack requests. These values are passed to the trajectory algorithm as a path constraint to be used while determining the optimal trajectory. An additional function of the trim deficiency algorithm queries the vehicle aerodynamic database to provide new vehicle coefficients of lift and drag in Mach-alpha space. The outer loop dynamical model employs reduced-order equations of motion that use interpolated table lookups to determine the appropriate lift and drag

coefficients derived from the vehicle state (based on angle of attack and Mach number). Once a control surface failure is detected and identified, the aerodynamic table is changed to reflect the new vehicle aerodynamics from the perspective of the reduced order dynamical model.

II. APPROACH

A. GENERAL APPROACH DISCUSSION

The model used in this thesis uses a reduced-order dynamical model that queries the vehicle full order aerodynamic model in order to capture the full 6-DOF model characteristics. A flat stationary earth in Cartesian coordinates is used in order to better understand and visualize the interactions between the different components of the optimization routine.

B. REDUCED-ORDER DYNAMICAL MODEL

1. Coordinate Systems

The simulation uses a three-dimensional Cartesian local horizon coordinate system that chooses as its origin the vehicle's position at the beginning of its unpowered descent or at the point in the descent at which a failure is identified. The positional elements are expressed as pure states in the easily recognized forms of x (downrange), y (crossrange), and z (altitude). The coordinate sign convention is the usual xyz sign convention where altitude decreasing moving "down", and down range increases to the "right" when viewing the xz plane from the side. The y axis is the cross product of the z and x axes. Full treatment of dynamical formulations in other coordinate systems can be found in Rea [ref. 7]. Figure 4 shows the coordinate system used in the reentry simulation.

where γ = flight path angle, the angle made by the velocity vector and the x-y plane.

β = azimuth angle, the angle made by the projection of the velocity vector onto the Newtonian x-z plane and the Newtonian x-axis. (This is used interchangeably with heading angle since we are dealing with a flat earth)

ϕ = bank angle, the angle made by the lift vector from vertical.

V = velocity magnitude

α = vehicle angle of attack

The body axes are depicted in blue; the Newtonian Frame is in black. The velocity vector and its projections are red. The lift and drag vectors are colored orange. The vehicle is assumed to be in coordinated flight (trimmed in yaw, no sideslip).

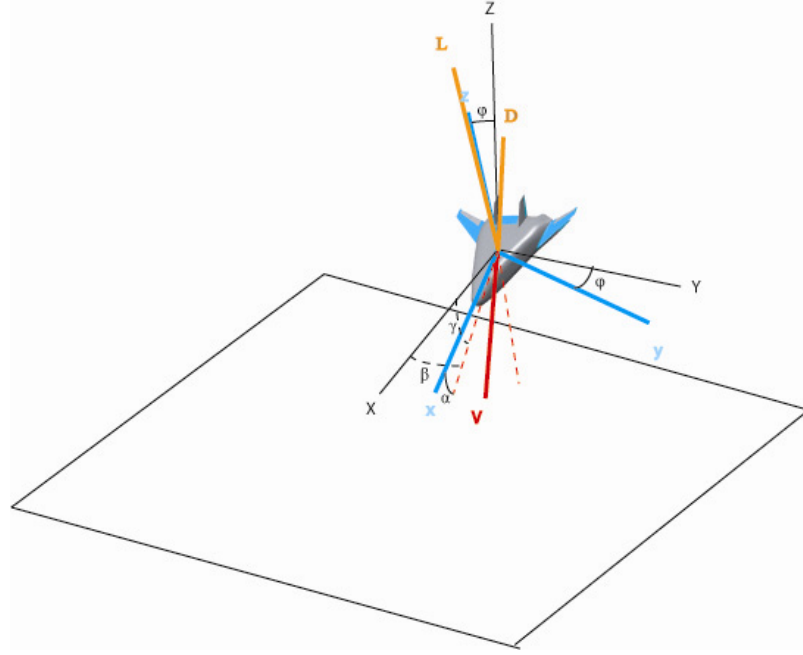


Figure 4 X-33 Simulation Coordinate System

2. Equations of Motion

The equations of motion are a simplified version of the traditional spherical earth equations of motion. There are six equations representing the kinematics and the 3DOF dynamics of the problem as adapted from Wiesel [ref. 6]. These equations of motion are shown below:

a. Kinematics:

$$\dot{x} = V \cos \beta \cos \gamma \quad (1.4)$$

$$\dot{y} = V \sin \beta \cos \gamma \quad (1.5)$$

$$\dot{z} = V \sin \gamma \quad (1.6)$$

b. Dynamics:

$$\dot{V} = -\frac{D}{m} - g \sin \gamma \quad (1.7)$$

$$\dot{\gamma} = \frac{L \cos \phi}{mV} - \frac{g \cos \gamma}{V} \quad (1.8)$$

$$\dot{\beta} = \frac{L \sin \phi}{mV} \quad (1.9)$$

The expressions for the lift and drag forces come directly from fundamental aerodynamics, repeated here for completeness.

$$L = \frac{1}{2} C_L A_{ref} \rho V^2 \quad (1.10)$$

$$D = \frac{1}{2} C_D A_{ref} \rho V^2 \quad (1.11)$$

In a full 6-DOF model the coefficients of lift and drag, $C_L(\alpha, M, \sigma, \delta), C_D(\alpha, M, \sigma, \delta)$ are functions of several variables: α is the vehicle's angle of attack, M is the Mach number, σ is the sideslip angle and δ is the control surface deflection vector previously discussed. The reduced order model employed by this thesis assumes that the coefficients of lift and drag are functions of the state variables *only*:

$$C_D, C_L = f(M, \alpha) \quad (1.12)$$

Additionally Mach number and atmospheric density are functions of altitude:

$$M = M(z) \quad (1.13)$$

$$\rho = \rho(z) \quad (1.14)$$

This simplified assumption is valid because the model performs a table lookup of the lift and drag coefficients that were obtained from a full order model that uses the vehicle flight condition and the optimized effector displacement vector as arguments to interpolate an aerodynamic data table for the vehicle. The resulting coefficients of lift and drag from wing, body and trim effects are summed and incorporated into the table. The effector displacement is an implicit argument in the algorithm's coefficients of lift and drag determination. The use of the optimized effector vector effectively decouples the outer loop from the inner loop.

3. The State Vector

The state vector is chosen to fully represent the state of the system in question at any instant. Using the flat earth coordinate system, the position of the vehicle can be represented by

$$\begin{bmatrix} x \\ y \\ z \end{bmatrix} \quad (1.15)$$

where

$$\begin{aligned} x &:= \text{downrange distance in feet} \\ y &:= \text{crossrange distance in feet} \\ z &:= \text{altitude in feet} \end{aligned}$$

The velocity of the vehicle is represented in spherical coordinates:

$$\begin{aligned} V &:= \text{the magnitude of the velocity in ft/sec} \\ \gamma &:= \text{the flight path angle (FPA) in radians} \\ \beta &:= \text{the azimuth angle, in radians} \end{aligned}$$

These three state variables when coupled with the positional information comprise the state vector:

$$\underline{x} = \begin{bmatrix} x \\ y \\ z \\ V \\ \gamma \\ \beta \end{bmatrix} \quad (1.16)$$

4. The Control Vector

The control vector for this problem is the vector whose elements are the controllable parameters of the system. For a vehicle trimmed in yaw, the coefficients of lift and drag and therefore x and z motion, are determined by the vehicle's angle of attack.

The vehicle's bank angle when combined with angle of attack determines the vehicle's cross range motion. Since reentry is accomplished dead-stick there is no thrust control variable. A suitable candidate for the control vector is therefore

$$\underline{u} = \begin{bmatrix} \alpha \\ \sigma \end{bmatrix} \quad (1.17)$$

α := the vehicle angle of attack
 σ := the vehicle bank angle

This type of control is also called *inertialess control* [ref. 20]

C. 4-DOF MODEL

The inertialess controller can be adapted to more accurately model the physical system by recognizing that physical actuators are *rate limited*. Inertia can be added to the system by imposing realistic rate constraints on the actuators. This is accomplished by incorporating the elements of the control vector in Equation (1.17) into the state vector in Equation(1.16). The new state vector becomes an 8-element vector.

$$\underline{x} = \begin{bmatrix} x \\ y \\ z \\ V \\ \gamma \\ \beta \\ \alpha \\ \sigma \end{bmatrix} \quad (1.18)$$

The new control vector components are now the rates of the previous control vector's components in Equation(1.17).

$$\underline{u} = \begin{bmatrix} \dot{\alpha} \\ \dot{\sigma} \end{bmatrix} \quad (1.19)$$

This alternative formulation is provides a more realistic model by preventing unlimited control surface deflection rates. Note that while the physical controls remain α and σ , the algorithm uses the rates of these variables in its optimization. This dynamical model is called a “4-DOF” model because it provides additional fidelity beyond the 3-DOF model. The full 4-DOF trajectory optimization algorithm is shown in Figure 6

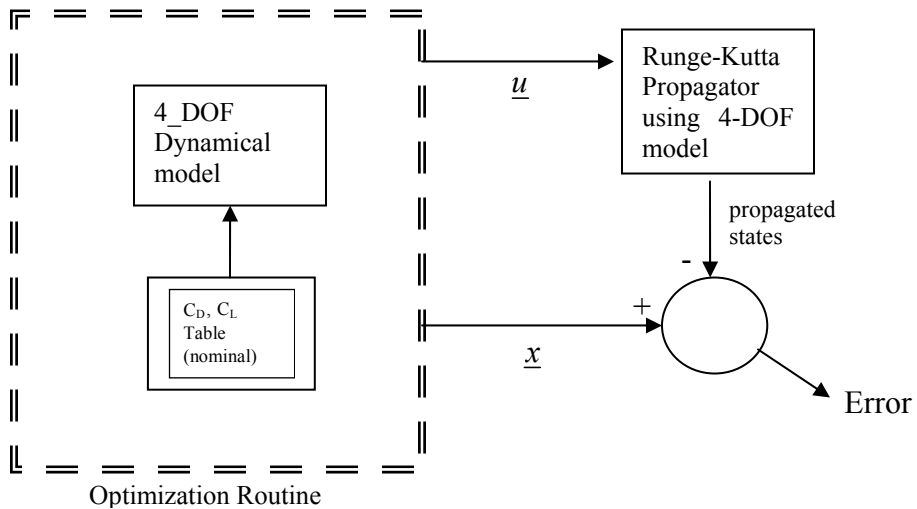


Figure 5 Trajectory Optimization Feasibility Error Estimation

The magnitude of the error shown in Figure 5 is used to choose the size of the nodes computed in the psuedospectral method. The number of nodes is increased until the error between the propagated states and optimal states is acceptable. Accuracy comes at a cost; the larger number of nodes significantly increases algorithm execution time.

D. ATMOSPHERIC MODEL

An AFRL atmospheric model which generates speed of sound and air density for a given an altitude is used. The outputs of the atmospheric model are combined with the vehicle velocity to determine the vehicle’s Mach number to be used in the aerodynamic

table lookups as well as the control allocator and trajectory path constraints. Figure 6 and Figure 7 depict the model's variance of the speed of sound and atmospheric density as a function of altitude. The atmospheric model is a combination of exponential functions separated by discrete altitude breakpoints.

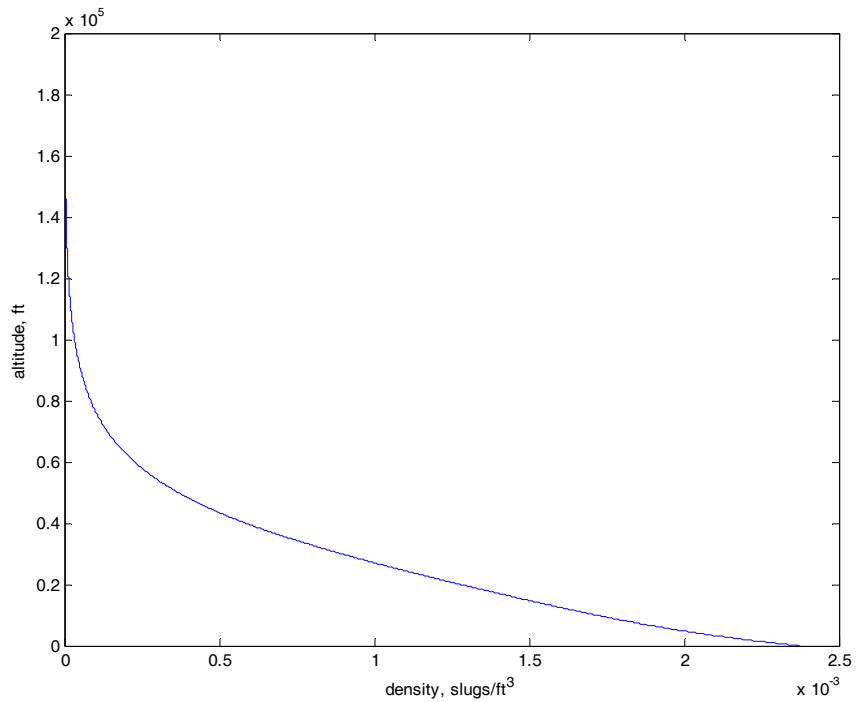


Figure 6 Plot of Density vs. Altitude (from AFRL atmosphere model)

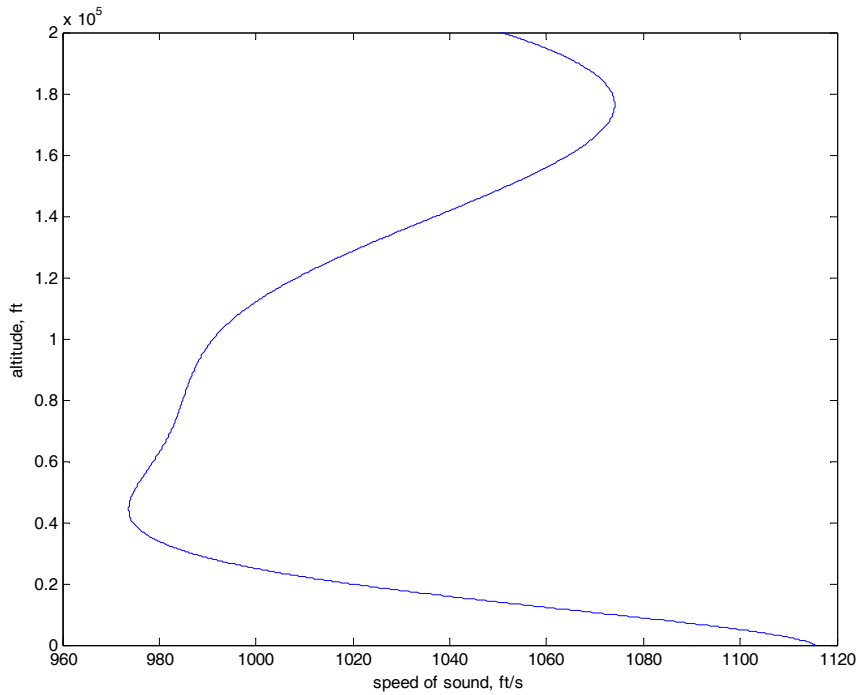


Figure 7 Plot of Speed of Sound vs. Altitude (from AFRL atmosphere model)

E. GRAVITATIONAL MODEL

The gravitational model used is a low order model that uses a constant gravitational acceleration which is assumed to always act in the negative z direction. The decision to use a simplistic model is based primarily on the desire to remove additional complications and observe the simulation dynamics in as pure a manner as possible.

F. X-33 AERODYNAMIC MODEL

This thesis considers the atmospheric entry of the X-33 reusable launch vehicle following a mission in low-earth orbit. The computed trajectory is an unpowered descent to a known landing field. The trajectory exposes the vehicle to full ranges of Mach and angle of attack. To accurately model the aerodynamic performance of the X-33, the trajectory code utilizes a dynamic linked library (dll) developed by Dr. David Doman of the Air Force Research Laboratory (AFRL) consisting of compiled C++ code that queries X-33 aerodynamic data derived from the full MAVERIC simulation. The file,

x33aero.dll, determines the full order aerodynamic characteristics including wing-body and trim effects from an input vector consisting of Mach number, angle of attack and control effector position. Since the position of the control effectors is arbitrary for any given desired angle of attack, two-dimensional tables of total lift and drag coefficients in Mach-alpha space are generated using another AFRL code that uses a piecewise linear programming (PLP) algorithm to determine the optimal control allocation of the vehicle's control surfaces (i.e., control induced moments balance the moments generated by the wing-body with minimum control deflection in a 1-norm sense) to achieve a desired angle of attack. The optimal control allocation is not directly used by the outer loop trajectory generator, but the resulting coefficients of lift and drag derived from the optimized control effectors for a given commanded angle of attack and Mach are used in the outer loop.

1. Mach Breakpoints

The X-33 aerodynamic data covers a range of angles of attack in increments of one degree from -10 to 50 degrees over a discrete Mach range given by [0 0.3 0.6 0.8 0.9 0.95 1.05 1.15 1.46 2.01 2.75 3.49 4.75 6 10 20]. This discrete Mach interval is used in the compiled C++ code referenced by the DIDO dynamics function. The aerodynamic database output is in the body frame, so an appropriate transformation to a Newtonian frame is necessary in order to analyze the trajectory. The normal force path constraints can be analyzed in the body frame.

2. AFRL PLP Control Allocation Model

The AFRL control allocation algorithm is used to trim the vehicle as well as computed the lift and drag estimates for the lift in any configuration. The algorithm assumes that the vehicle is in symmetric flight (sideslip angle is zero) and the resulting lateral wing-body force and moment coefficients are zero. By assuming a zero magnitude body-axis angular velocity, the wing-body pitching moment of the vehicle becomes a function of Mach number and angle of attack. This allows for the necessary conditions to rotationally trim the vehicle that the moments resulting from the control surface deflections must be equal and opposite that of those produced by the wing-body [ref. 22]

$$\begin{bmatrix} C_{l_\delta}(M, \alpha, \underline{\delta}) \\ C_{m_\delta}(M, \alpha, \underline{\delta}) \\ C_{n_\delta}(M, \alpha, \underline{\delta}) \end{bmatrix} = \begin{bmatrix} 0 \\ -C_{m_o}(M, \alpha) \\ 0 \end{bmatrix}$$

Where l, m, n denote the roll, pitch and yaw axis, C_{i_δ} is the moment coefficient caused by the control surface deflection about either the l, m or n axis. M is the Mach number, α is the angle of attack and $\underline{\delta}$ is the control surface deflection vector caused by the eight individual vehicle control surfaces.

The first task of the control allocator determines the optimum effector displacement that results in minimum control deficiency. The full description is contained in reference 22 and repeated here for completeness. The full set of control surface deflections for the X-33 can be represented by the eight-element effector displacement vector previously identified in equation (1.1). This vector is subject to the limits of equations (1.2) and (1.3) or a subset thereof for control surface failures. The control allocation problem uses an iterative algorithm that queries the full 6-DOF X-33 aerodynamic database. The piecewise linear constrained control allocation problem is

$$\text{Min}_{\underline{\delta}} J_D = |C_{l_\delta}(M, \alpha, \underline{\delta})| + |C_{m_\delta}(M, \alpha, \underline{\delta})| + |C_{n_\delta}(M, \alpha, \underline{\delta})| + |C_{m_o}(M, \alpha)|$$

$$\text{subject to } \underline{\delta}_{lower} \leq \underline{\delta} \leq \underline{\delta}_{upper}$$

Notice that the upper and lower bounds on $\underline{\delta}$ are dependant upon the operating mode of the vehicle. A vehicle operating under nominal conditions has the full range of deflections available while a vehicle operating with a control surface failure has a subset of the nominal displacement vector's range.

A nonzero value of J_D means there is insufficient control power to rotationally trim the vehicle (it is trim deficient), and the vehicle will depart controlled flight. The trim deficient regions in Mach-alpha space can be mapped and identified as “keep-out” zones for the outer loop trajectory algorithm. If the control allocation algorithm is able to

rotationally trim the vehicle, any excess control power can be used to maneuver the vehicle. The control allocator employs a second control allocation optimization algorithm to minimize the deviation from a minimum trim-drag condition. This condition is represented by an eight-element preference vector set to zero. The second optimization is

$$\text{Min}_{\underline{\delta}} J_S = \left\| \underline{W} (\underline{\delta} - \underline{\delta}_p) \right\|_1$$

$$\text{subject to } \underline{\delta}_{lower} \leq \underline{\delta} \leq \underline{\delta}_{upper}$$

$$\left| C_{l_\delta} (M, \alpha, \underline{\delta}) \right| = 0$$

$$\left| C_{m_\delta} (M, \alpha, \underline{\delta}) \right| = 0$$

$$\left| C_{n_\delta} (M, \alpha, \underline{\delta}) \right| = 0$$

In the case where the vehicle is operating with excess control power, the effector displacement vector is the output of the second optimization routine, otherwise $\underline{\delta}$ minimizes the trim deficiency. The effector displacement vector that is the solution of the control allocator is represented as $\underline{\delta}^*$ to delineate it from the infinite combination of control surface deflections that are available to achieve the same desired control but are not optimized for either trim deficiency or minimum trim-drag.

Given $\underline{\delta}^*(\alpha, M)$ (from the control allocation algorithm), the X-33 aerodynamic database is queried over the Mach-alpha grid to generate the wing-body and trim lift and drag coefficients. These coefficients when summed together represent the total lift and drag coefficients. The use of the control allocator solution effectively decouples the trajectory generation algorithm from the inner loop and allows the lift and drag coefficients to be functions of angle of attack and Mach number. Effector displacement remains an implicit argument and allows for the full 6-DOF model's behavior to be captured by a lower order model. The outer loop equation (1.12) is elaborated using the lift and drag coefficients as the sum of the wing-body coefficients plus the effector-dependent trim coefficients using the control allocator solution.

$$\begin{aligned}
C_L(M, \alpha) &= C_{L_o}(M, \alpha) + C_{L_\delta}(M, \alpha, \underline{\delta}^*(M, \alpha)) \\
C_D(M, \alpha) &= C_{D_o}(M, \alpha) + C_{D_\delta}(M, \alpha, \underline{\delta}^*(M, \alpha))
\end{aligned} \tag{1.20}$$

The relationships in (1.20) hold for a vehicle in symmetric flight and can be stored in an aerodynamic lookup table for each Mach and angle of attack combination subject to the limits on the effector displacement vector dictated by the presence of nominal or failure conditions. Each failure condition requires a separate run of the control allocator. A block model implementation of the control allocator is depicted in Figure 8

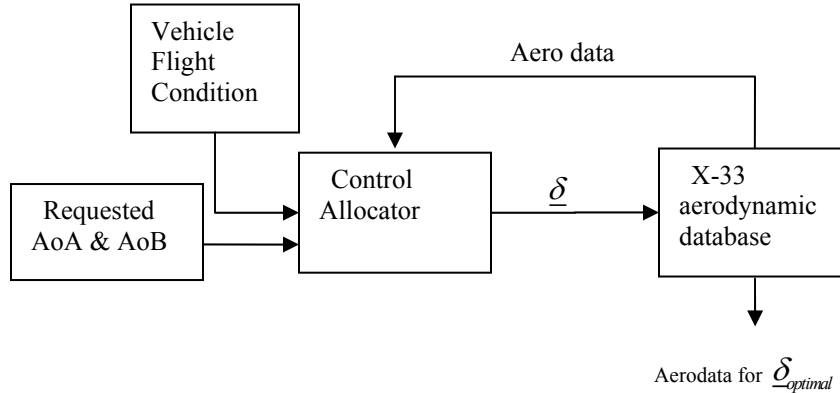


Figure 8 AFRL Control Allocator

3. Trajectory Replanning Algorithm

The vehicle is assumed to operate in the nominal condition until a failure has been identified through some online fault detection or identification algorithm at which point the lift and drag table corresponding to the failed vehicle configuration is generated. An approximate block diagram of the guidance loop is shown in Figure 9

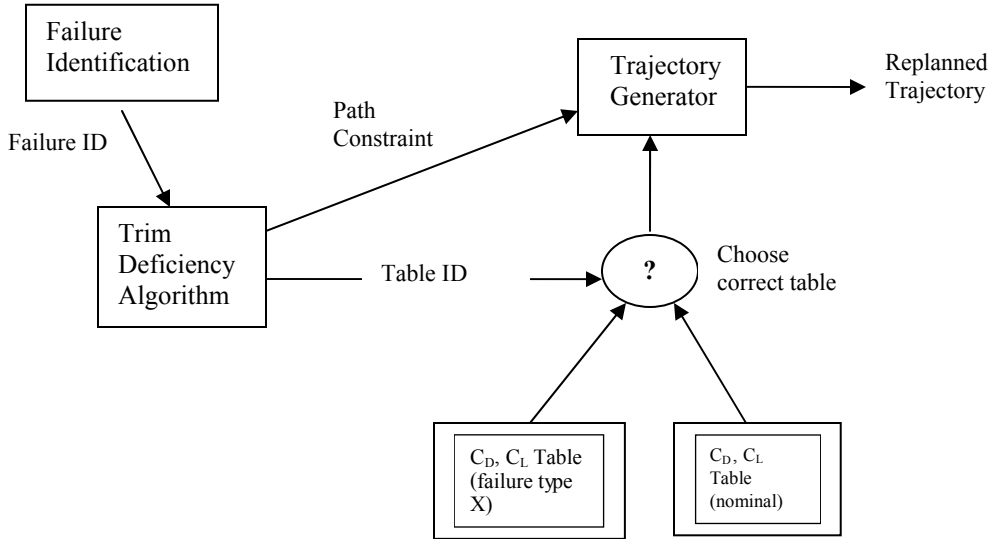


Figure 9 Trajectory Replanning

4. Failure Mode

Once a failure has been identified, the PLP control allocator generates a new set of control deflections for the failed vehicle and uses the aerodynamic database to determine the new trim lift and drag contributions. In the process of computing the control deflections for the failed vehicles, points in the Mach-alpha envelope for which the vehicle cannot be trimmed are identified. These trim deficiency regions must be avoided and are thus used as path constraints for the trajectory replanning. The trajectory aerodynamic data table is changed to one appropriate for the vehicle in the current failed condition and a new trajectory is generated for the new aerodynamics and path constraints.

5. Failure Mode Effects

The trim deficiency path constraint on the available range of angle of attacks for a given Mach number requires that the vehicle must be rotationally trimmable (assuming no side slip) for a given angle of attack. When the vehicle operates in a nominal configuration it is capable of trimming over a full range of angle of attack, however, when the vehicle experiences control degradation, its available range of angles of attack may be severely reduced. Doman, et al. [ref 19] give full treatment of this subject. Figure

10 depicts the available values of angle of attack that will allow for a rotationally trimmed vehicle experiencing no failures. Notice that because the maximum trim deficiency value is on the order of machine precision so that the entire range of combinations of angles of attack and Mach numbers is considered to be available in the nominal (unfailed) case.

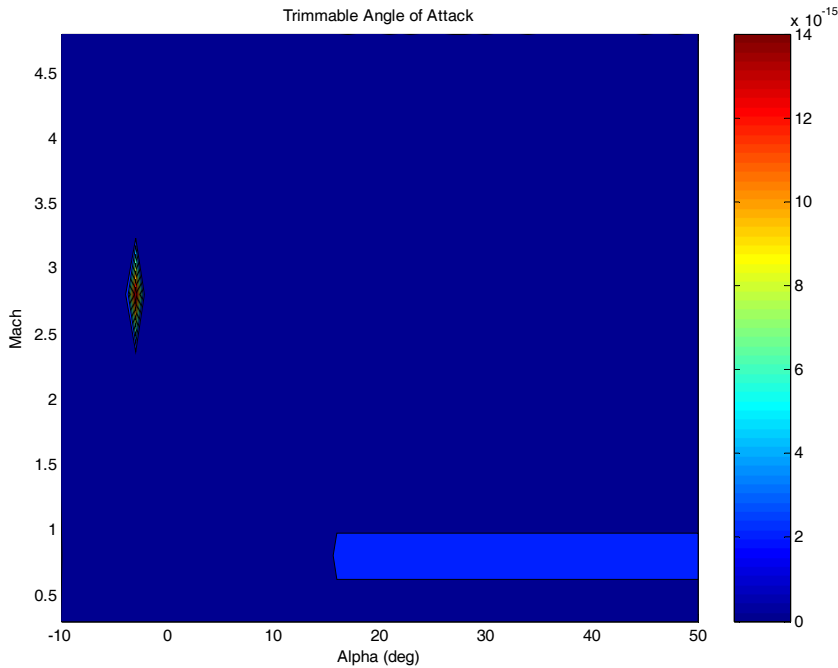


Figure 10 X-33 Trimmable Values for Angle of Attack.(from Ref 19.)

Figure 11 shows an example of the constrained Mach-alpha envelope available to the X-33 following a dual body flap failure (stuck at 26 degrees up). Notice that the envelope describing allowable angles of attack (in dark blue) previously depicted in Figure 10 is now severely reduced. Angles of attack other than those contained within the dark blue region will place the vehicle in an attitude where it is not trimmable in pitch (pitch deficient) and therefore uncontrollable. This establishes a restricted region that feasible trajectories must avoid. In other words, the trajectory must have a clear path in Mach-alpha space from the initial conditions to the final conditions. A clear path is defined as a path from one point defined by the flight condition (Mach-alpha) to another point (Mach-alpha) with no intervening regions of unacceptable trim deficiency. Should

a path cross into or through a region of pitch deficiency, the trajectory becomes infeasible because the vehicle is no longer rotationally trimmable and therefore uncontrollable.

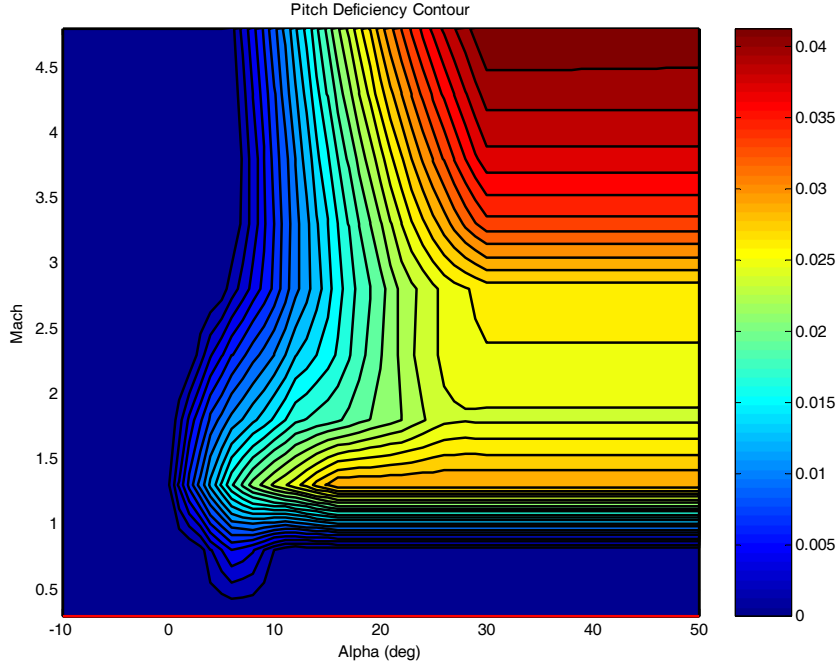


Figure 11 X-33 Trimmable Values of Angle of Attack following a Dual Stuck Flap Failure (failed at 26 degrees up). (from Ref. 19).

A feasible solution, if it exists, must be found using these new path constraints. The allowable range of angle-of-attack can be determined in a manner similar to the previous method used to generate the lift and drag tables using the AFRL X-33 aerodynamic database and control allocator. The result is a dataset that accurately describes the trim deficiency as a function of Mach number and angle of attack (the vehicle's flight condition). This dataset is the output of the AFRL trim deficiency algorithm which also determines the new coefficients of lift and drag for the failed condition using the new optimized effector displacement vector.

Some failures will have very restrictive path limits for feasible trajectories while others may have no clear path. Figure 12 shows a failure where the vehicle is free to operate in a high Mach flight condition but cannot safely land. Figure 13 depicts a failure where the vehicle is limited to slower speeds and alpha ranges to safely land.

Note that the previous discussion does not consider any other limitations such as normal force, heating or dynamic pressure on the trajectory. These constraints will further reduce the area available to a clear path for a feasible trajectory. In some cases, the additional constraints will completely eliminate a clear path and render trajectory infeasible. It is easier to visualize the optimal trajectory with constraints as a region through Mach-alpha space for which the vehicle must be rotationally trimmable. If a failure impinges on this corridor and prevents a clear path through to landing, then there are no feasible trajectories available.

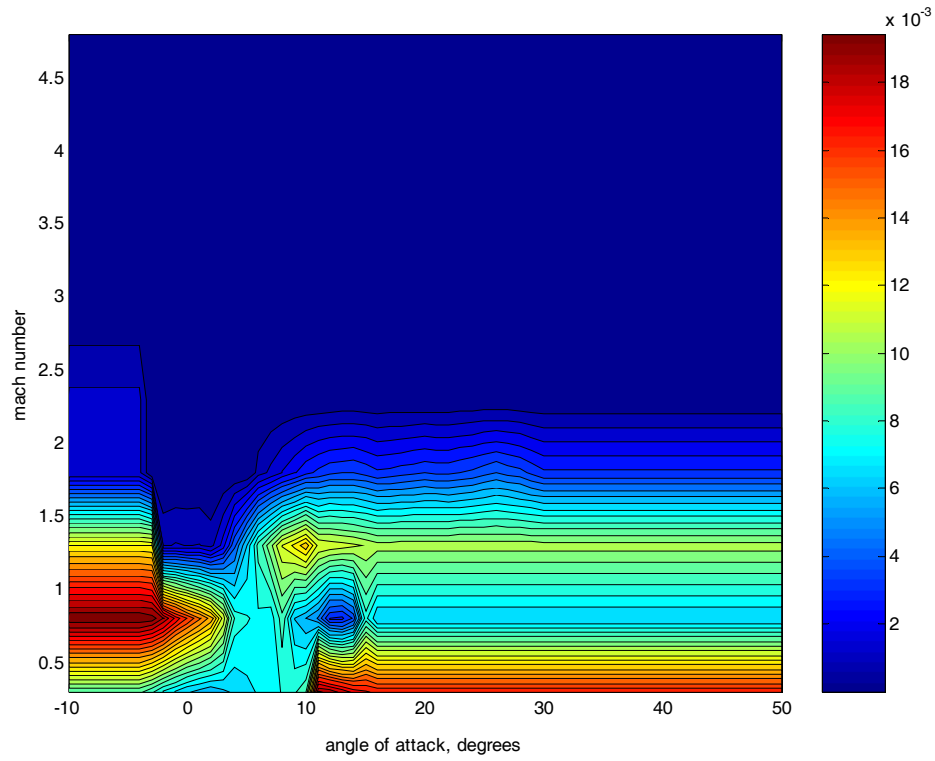


Figure 12 X-33 Pitch Deficiency Following a Stuck Right Rudder (15 degrees)

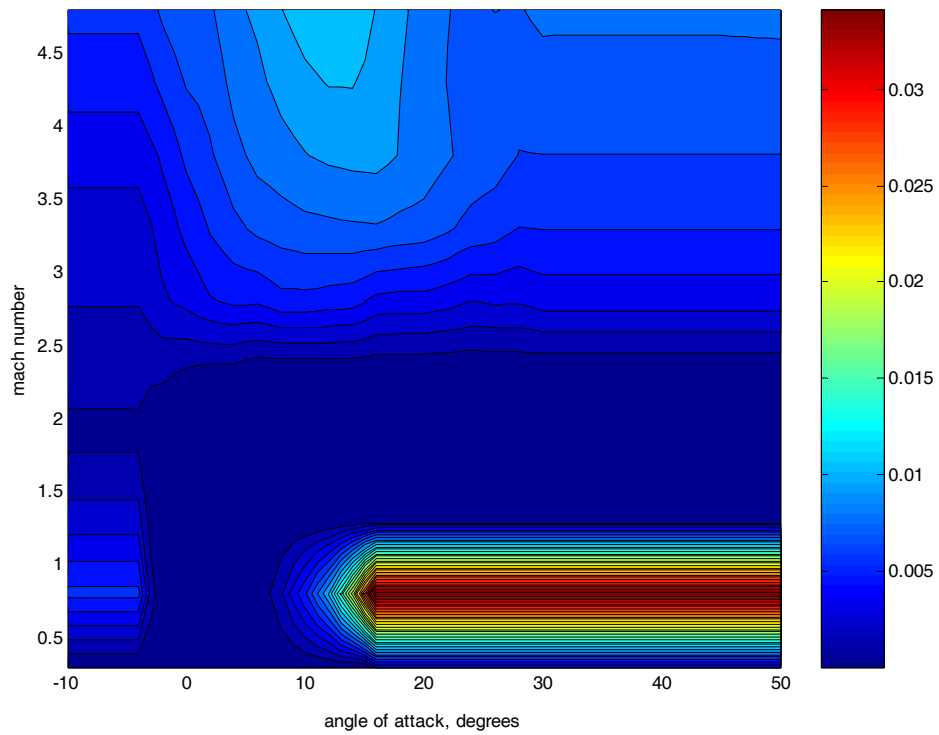


Figure 13 X-33 Pitch Deficiency Following a Stuck Flap (at -15 degrees)

6. Modeling Trim Deficiency

As the previous graphs of failure modes show, the trim deficiency can be modeled as a function of two variables:

$$d = f(M, \alpha) \quad (1.21)$$

The function, f , can be determined from various fits to the trim deficiency data. This thesis uses the Table Curve 3D software, version 4.0 by Systat Software (www.systat.com) to generate MATLAB function codes that approximate the data generated by the trim deficiency routines. Table Curve 3D is very robust and can apply and analyze the fits of over 9000 equation types to the fitted data in short order. An example of the raw data from the trim deficiency code imported into Table Curve 3D is shown in Figure 14

Trim Deficiency in Mach-Alpha Space

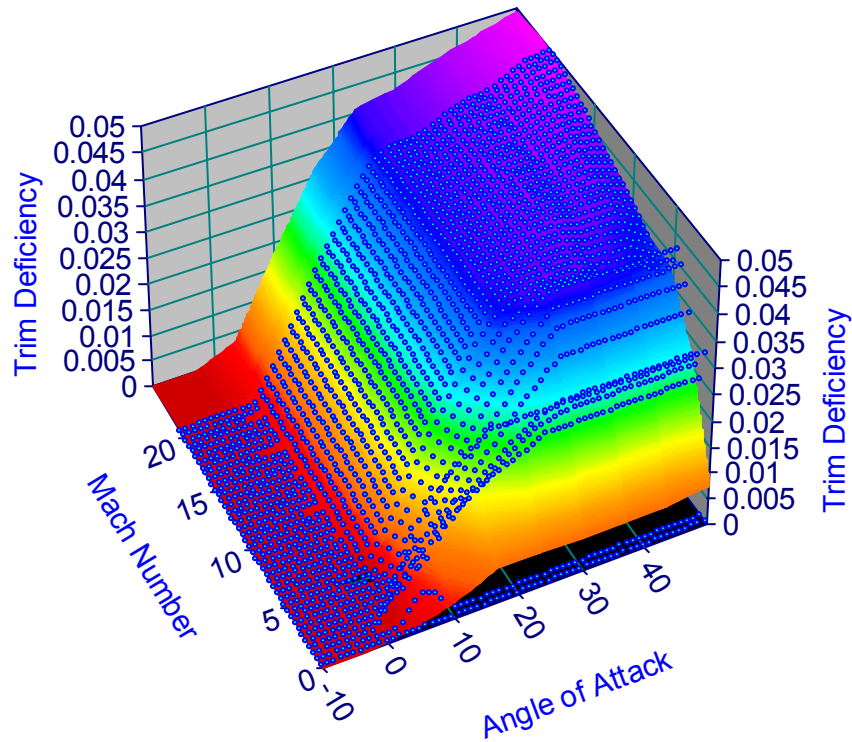


Figure 14 Table Curve 3D Trim Deficiency Data for a Dual Stuck Flap Failure (26 degrees)

A 10th order Chebyshev polynomial produces a very good data fit. The function generated by the Table Curve 3D code was used in the path function file of the DIDO code. The path function file combined with appropriate bounds on the path prevents the selection of combinations of Mach and angle of attack that exceed a given trim deficiency. An important selection criterion for the fitted curve is the function's behavior at the boundaries of the Mach-alpha envelope. Some fitting functions that showed good residuals for the data were rejected out of hand because the low Mach and angle of attack data fits were very poor. It is more important that the fitting function models the data within the feasible ranges of trim deficiency than for ranges where feasible trajectories do not exist. Mismatched data for extreme trim deficient regions can be tolerated but it is

essential that the fit near the transition from zero trim deficiency to positive trim deficiency be as good as possible.

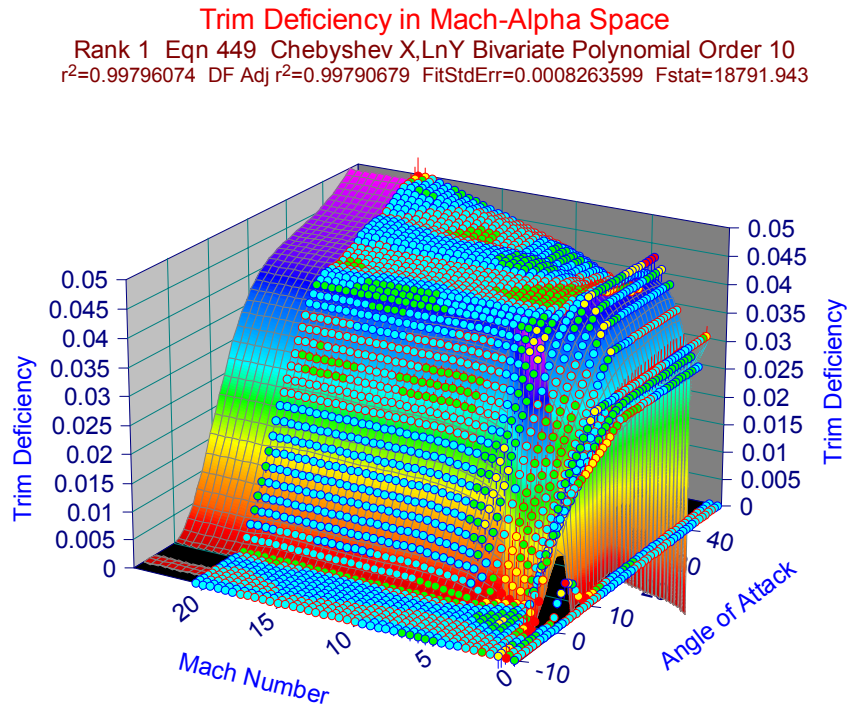


Figure 15 Trim Deficiency Fitted with 10th order Chebyshev Polynomial

The trim deficiency can also be modeled as a pure table lookup which queries the tablular data from the trim deficiency algorithm. This approach is more accurate than the fitted function but was omitted from this study because of the inherent execution penalties resulting from a 3-dimensional table lookup. The feasibility of following a trim deficiency path constraint is shown by projecting the trajectory into Mach-alpha space along with the trim-deficiency contour plot and verifying that the trajectory does not violate the path constraints. The feasibility can also be shown by inspection of the numerical trim deficiency data for the trajectory.

THIS PAGE INTENTIONALLY LEFT BLANK

III. THE OPTIMAL CONTROL PROBLEM

A. OPTIMAL CONTROL THEORY

The following sections summarize the general optimal control problem formulation and the two known methods of generating solutions.

1. Preliminaries

Nearly any trajectory generation problem can be posed as an optimal control problem and the problem considered by this thesis is no exception. Given a system with dynamic constraints

$$\dot{\underline{x}} = \underline{f}(\underline{x}, \underline{u}, \tau) \quad (1.22)$$

where

$$\begin{aligned} \underline{f} &:= \text{vector of functions that describe the dynamics of the system} \\ \underline{x} &:= \text{vector of states that fully describe the system at any } \tau \\ \underline{u} &:= \text{vectors of control variables} \\ \tau &:= \text{an independent variable (usually time)} \end{aligned}$$

The system is subjected to additional constraints to include the path constraint:

$$\underline{h}_l \leq \underline{h}(\underline{x}, \underline{u}, t) \leq \underline{h}_u, \quad (1.23)$$

where

$$\begin{aligned} \underline{h} &:= \text{vector of functions describing the path constraints} \\ \underline{h}_l &:= \text{vector of lower path bounds} \\ \underline{h}_u &:= \text{vector of upper path bounds} \end{aligned}$$

and boundary conditions

$$\underline{e}_l \leq \underline{e}(\underline{x}(\tau_0), \underline{x}(\tau_f), \tau_0, \tau_f) \leq \underline{e}_u \quad (1.24)$$

where

$\underline{e}(x(\tau_0), \tau_0)$:= vector of initial boundary conditions (at τ_0)

$e(x(\tau_f), \tau_f)$:= vector of final boundary conditions (at τ_f)

\underline{e}_l := vector of lower bounds

\underline{e}_u := vector of upper bounds

The system also has bounds on the control and state variables represented by

$$\underline{x}_l \leq \underline{x}(\tau) \leq \underline{x}_u \quad (1.25)$$

$$\underline{u}_l \leq \underline{u}(\tau) \leq \underline{u}_u \quad (1.26)$$

where

$\underline{x}(\tau)$:= state vector at any instance of τ

$\underline{u}(\tau)$:= control vector at any instance of τ

$\underline{x}_l, \underline{x}_u$:= vectors of lower and upper state bounds

$\underline{u}_l, \underline{u}_u$:= vectors of lower and upper control bounds

The bounds on the state and control vectors can be thought of connecting the physical system being modeled to the mathematical model used to solve the optimal control problem. For example, if the control is acceleration, no physically realizable device produces infinite acceleration and we therefore may choose to limit the control to a sensible value. Similarly, if one element of the state vector is velocity, we may choose to limit the velocity to one that is within the design limits of the physical system. Imposing constraints on the state and control vectors may not be necessary in all cases but the resulting optimal solution of unbounded states or controls needs to be given a hard reality check when realizing a physical implementation of the optimal solution.

An optimal control problem seeks to determine the solution of the preceding dynamical system with its bounds and constraints to minimize a given performance index. The performance index is mathematically defined below:

$$J(\underline{x}(\tau), \underline{u}(\tau), \tau_0, \tau_f) = E(\underline{x}(\tau_0), \underline{x}(t_f), \tau_0, \tau_f) + \int_{\tau_0}^{\tau_f} F(\underline{x}(\tau), \underline{u}(\tau), \tau) d\tau \quad (1.27)$$

where

E := scalar cost function evaluated at the boundaries

F := scalar cost function evaluated over the entire interval

When J consists of only E , the cost function is in Mayer form. When J consists of only F , the cost function is in Lagrange form. When both E and F are present, the cost function is in Bolza form.

The general optimal control problem is fully posed in the following manner:

$$\min_u J(\underline{x}(\tau), \underline{u}(\tau), \tau_0, \tau_f) = E(\underline{x}(\tau_0), \underline{x}(t_f), \tau_0, \tau_f) + \int_{\tau_0}^{\tau_f} F(\underline{x}(\tau), \underline{u}(\tau), \tau) d\tau$$

subject to $\dot{\underline{x}} = \underline{f}(\underline{x}, \underline{u}, \tau)$

$$\underline{h}_l \leq \underline{h}(\underline{x}, \underline{u}, \tau) \leq \underline{h}_u$$

$$\underline{e}_l \leq \underline{e}(\underline{x}(\tau_0), \underline{x}(t_f), \tau_0, \tau_f) \leq \underline{e}_u$$

$$\underline{x}_l \leq \underline{x}(\tau) \leq \underline{x}_u$$

$$\underline{u}_l \leq \underline{u}(\tau) \leq \underline{u}_u$$

The formulation of the system as represented in the state vector, the appropriate choice of the dynamical equations, and the selections of the constraints and bounds forms the basis of the fully posed optimal control problem

2. Solution Methodology

Once the problem has been properly formulated there are two general methods available to solve the optimal control problem, direct and indirect [ref. 27]. Indirect methods tend to generate fast solution times and greater accuracy but are considerably more difficult to formulate and are very sensitive to the initial guess [ref. 27]. Formulation of the indirect method can be exceedingly difficult in situations where the

dynamics functions are not pure functions but instead rely on numerical data such as the aerodynamic lookup tables used in this thesis.

Direct methods reduce the optimal control problem to a single large Nonlinear Programming (NLP) problem. The strengths of the indirect methods are that the formulation is significantly easier and the methods are relatively insensitive to the initial guess. A particular drawback of direct methods is large execution times. When direct methods are used, there are tradeoffs between execution time and accuracy. An increase in the size of the NLP program does not necessarily yield a proportional increase in solution accuracy or solution time. This drawback inhibits real time optimal control using direct methods for certain problems such as are considered in this thesis; however, as computing power continues to increase, the potential for real-time optimal control will soon be realized.

3. DIDO

This thesis uses the DIDO numerical dynamic optimization software developed by I.M. Ross and F. Fahroo of the Naval Postgraduate School. DIDO employs a direct Legendre psuedospectral technique that uses the NLP solver SNOPT. The reader is referred to References 12 through 17 for a full description of the Legendre psuedospectral method. This thesis shows another application of DIDO in solving optimal trajectory problems.

4. Optimality

Since the formulation of a problem using a direct Legendre psuedospectral method does not determine the adjoint equations, another tool must be employed to link the solutions generated by indirect methods and direct methods. The Covector Mapping Theorem (CMT) provides this link and is fully explained in Reference 8. The implications of the CMT allow a determination of the optimality of a given solution by comparing the costates of the solution to the Karush-Kuhn-Tucker (KKT) multipliers. Every time a state or control becomes bounded, the corresponding costate should follow the KKT conditions as if they were the KKT multipliers. Additional evidence of optimality can be obtained by investigating the solution's Hamiltonian and the final value

of the cost function. These necessary conditions may be easily obtained from the DIDO solution and provide insight into the optimality of the DIDO generated solution.

5. Feasibility

Because the DIDO solution is based upon the controls for a discretized set of points determined by the Legendre polynomials used in the solution, the DIDO solution may not possess the desired accuracy at the final endpoint. Since the accuracy of a DIDO solution is a function of the number of nodes evaluated in the solution space, all DIDO solutions should be evaluated for feasibility. This is usually accomplished by comparing the DIDO solution to a separate solution using the DIDO controls propagated by a Runge Kutta ODE solver such as MATLAB's ODE45. The error between the propagated states and the DIDO-derived states gives some measure of confidence of the accuracy of the DIDO solution. The required accuracy is determined by the application, for example while the downrange accuracy of a 20-node DIDO solution reentry trajectory is 0.0001% of the propagated downrange distance, it still may be inaccurate enough to prevent a feasible landing at the desired field. Feedback may be able to overcome this inaccuracy provided the solution update is achieved at a reasonable rate. Another guard against inaccuracies in a trajectory is to provide additional margins when defining the endpoint conditions.

6. Scaling and Balancing

While direct methods are relatively insensitive to the initial guess, a well-formulated problem can be completely ruined by improper scaling and balancing of the variables and constants used in the computation. Ross [ref 21] notes the effect of improper scaling on the DIDO solution. It should be noted that *mks* units are a much better choice of units and are preferred to English units from a computational viewpoint because *mks* units are direct combinations of distance, mass and time base units and thus easily scaled while some English units have no direct equivalent.

The intent of scaling and balancing is to avoid the problems associated with variables whose range exceeds that of numerical precision (about 16 significant figures on a Pentium-class PC). A proper scaled problem scales the variables to a range of 0 to 1. While it is not necessary to be exactly within this range, it is clear that variables of the

same order of magnitude avoid problems associated with computing ill-conditioned matrices resulting from numerical imprecision. The general approach to scaling the problem variables is as follows:

The fundamental units in any system of measure traditionally cover mass, time and distance. Other units such as area, volume and velocity are derived from these fundamental units. Consider the initial condition for the third element of the state vector, altitude. The initial altitude is 125,000 feet while the final altitude is 500 feet. Additionally, the initial downrange distance is at the origin of the coordinate system while the expected maximum downrange is nearly 4,000,000 feet. A scaled distance unit is created by applying a *scale factor* to the state variables.

$$\tilde{x} = \frac{x}{DU}$$

$$\tilde{y} = \frac{y}{DU}$$

$$\tilde{z} = \frac{z}{DU}$$

Where DU represents the scaling of the distance unit. To scale a variable that represents velocity notice that

$$velocity = \frac{\text{distance}}{\text{time}}$$

To scale velocity, simply divide by the velocity scaling factor.

$$\tilde{V} = \frac{V}{VelUnit} = \frac{V}{\left(\frac{DU}{TU}\right)} = V\left(\frac{TU}{DU}\right)$$

Similarly, the scaling factors for acceleration and force are

$$AcelUnits = \frac{DU}{(TU)^2};$$

$$ForceUnits = MU\left(\frac{DU}{(TU)^2}\right)$$

Arbitrarily choosing DU=100,000 ft and TU= 50 seconds for this problem scales the state variables as shown:

$$\begin{aligned} \begin{bmatrix} x_i \\ y_i \\ z_i \\ V_i \end{bmatrix} &= \begin{bmatrix} 0 \\ 0 \\ 200,000 \text{ ft} \\ 8000 \text{ ft/sec} \end{bmatrix} \rightarrow \begin{bmatrix} \tilde{x}_i \\ \tilde{y}_i \\ \tilde{z}_i \\ \tilde{V}_i \end{bmatrix} = \begin{bmatrix} 0 \\ 0 \\ 1 \\ 2 \end{bmatrix} \\ \begin{bmatrix} x_f \\ y_f \\ z_f \\ V_f \end{bmatrix} &= \begin{bmatrix} 4,000,000 \text{ ft} \\ 0 \\ 500 \text{ ft} \\ 250 \text{ ft/sec} \end{bmatrix} \rightarrow \begin{bmatrix} \tilde{x}_i \\ \tilde{y}_i \\ \tilde{z}_i \\ \tilde{V}_i \end{bmatrix} = \begin{bmatrix} 20 \\ 0 \\ 0.0025 \\ 0.0625 \end{bmatrix} \end{aligned}$$

After scaling, the range of distances falls between 0 and twenty for down range and between 0 and 2 for velocity. The problem should also be balanced, that is all path constraints should be as close to the same order of magnitude. While this may not be possible, every attempt should be made to balance the problem as well as to scale it.

B. REENTRY VIEWED AS AN OPTIMAL CONTROL PROBLEM

After scaling and balancing, the atmospheric entry (or reentry) can be formulated as an optimal control problem.

The reentry problem considers a vehicle entering the atmosphere from an initial position, presumably near LEO and seeks to generate an optimal trajectory that brings it to a final state specified by an endpoint condition. The trajectory may not violate the path constraints which limit heating rate, normal force, and axial force (dynamic) pressure. The optimal trajectory seeks to minimize a performance index which is generally a function of the state of the vehicle. Typical performance indices for reentry are maximizing downrange, maximizing cross range, minimizing control effort, or some weighted combination of these indices.

The trajectory is also subject to dynamic constraints which describe the dynamics of the system. As discussed in the previous section, this thesis uses a simple dynamic model that retains the benefits of a higher fidelity model by including the effects of trim lift and drag and using table lookups into a high-fidelity aerodynamic database.

For a typical trajectory that seeks to determine the maximum downrange value for an entering vehicle, the cost function is simply a Mayer cost:

$$J(\underline{x}(t), \underline{u}(t), t_0, t_f) = -x_f$$

Time is the independent variable for this problem. A Lagrange component of the cost can be included as desired. The initial boundary conditions for a representative mission are

$$\underline{e}(x(t_0), t_0) = \underline{x}_i = \begin{bmatrix} x_i \\ y_i \\ z_i \\ V_i \\ \gamma_i \\ \beta_i \\ \alpha_i \\ \sigma_i \end{bmatrix} = \begin{bmatrix} 0 \\ 0 \\ 125,000 \text{ ft} \\ \text{Mach 8} \\ -1.3 \text{ deg} \\ 0 \\ 0 \\ 0 \end{bmatrix}$$

The endpoint equation does not need to fully describe the state vector, only the conditions that are necessary for a safe transition and landing. The manifold can be simple such as:

$$e(x(t_f), t_f) = \begin{bmatrix} z_f \\ V_f \end{bmatrix} = \begin{bmatrix} 500 \text{ ft} \\ \text{Mach 0.15} \end{bmatrix}$$

The vector above does not specify the final angles of attack or bank and it is possible that the vehicle could arrive at the ending manifold in an unrecoverable position (high angles of attack and bank along with large vertical speed). To prevent this from occurring, it is good practice to fully specify these variables as well as the associated acceptable range of values at the end point. Initial trajectories computed appear to be feasible trajectories but

upon closer inspection met the end point manifold with vertical speeds exceeding 20,000 feet per minute. The endpoint manifold was then modified to an endpoint set limited to vertical speeds between $-1500 \text{ ft/min} \leq \dot{z} \leq 500 \text{ ft/min}$.

The path constraints are derived primarily from the design and mission considerations of the vehicle.

$$\begin{bmatrix} -3g \\ -\infty \end{bmatrix} \leq \begin{bmatrix} \text{normal force}(t) \\ \text{trim def}(t) \end{bmatrix} \leq \begin{bmatrix} 6g \\ 0 \end{bmatrix}$$

There are limits placed on the state vector and controls

$$\begin{bmatrix} -\infty \text{ ft} \\ -\infty \text{ ft} \\ 0 \text{ ft} \\ 0 \text{ ft/s} \\ -\frac{\pi}{2} \text{ rad} \\ -\infty \text{ rad} \\ -10 \text{ deg} \\ -\frac{\pi}{2} \text{ rad} \end{bmatrix} \leq \underline{x} \leq \begin{bmatrix} \infty \text{ ft} \\ \infty \text{ ft} \\ \infty \text{ ft} \\ \infty \text{ ft/sec} \\ \frac{\pi}{2} \text{ rad} \\ \infty \text{ rad} \\ 50 \text{ deg} \\ \frac{\pi}{2} \text{ rad} \end{bmatrix} \quad \text{and} \quad \begin{bmatrix} -40 \frac{\text{deg}}{\text{sec}} \\ -40 \frac{\text{deg}}{\text{sec}} \end{bmatrix} \leq \underline{u} \leq \begin{bmatrix} 40 \frac{\text{deg}}{\text{sec}} \\ 40 \frac{\text{deg}}{\text{sec}} \end{bmatrix}$$

The limits that have values of plus and minus infinity represent states without hard limits and are not truly constraints upon the state vector. The constraint on the altitude component of the state vector is imposed to prevent premature contact with the ground.

THIS PAGE INTENTIONALLY LEFT BLANK

IV. APPLICATIONS

A. FOOTPRINT DETERMINATION

The first step in determining the vehicle performance begins with investigating the nominal (unfailed) case. A rough vehicle footprint can be established by changing the cost functions to include various combinations of the form

$$M = Ax(\text{end}) + By(\text{end})$$

Where $A + B = 1$ and $0 \leq A \leq 1$; $0 \leq B \leq 1$.

$x(\text{end})$ and $y(\text{end})$ are the final values of downrange and crossrange.

The constants for cost function used to determine the maximum downrange are simply $A=1$ it follows, therefore that $B=0$. Note that when $A=-1$, minimum downrange is implied. The constants for cost function used to determine the maximum crossranges are simply $B=1$ it follows, therefore that $A=0$. Note that when $B=-1$, minimum crossrange is implied, which for the nominal case should be symmetric about the x axis.

B. LANDING AT A SPECIFIC FIELD WITHIN THE FOOTPRINT

Once the rough limits of the footprint have been established, the vehicle should be able to land at any field within the footprint. In order to recover the vehicle at a specific field, the conditions at the landing threshold that lead to a “successful” landing must be strictly defined. Original runs that specified a small subset of the state vector at the endpoint led to unsatisfactory conditions at the landing threshold. Consider the endpoint conditions specified by

$$e(\underline{x}_f, t_f) = \begin{bmatrix} z_f \\ V_f \end{bmatrix}$$

Optimal trajectories can be generated which meet these endpoint conditions; however, the vehicle state may be such that a successful landing is not possible given the practical limitations of the vehicle. Original trajectories which used the previous endpoint condition appeared reasonable until the vertical speed at the landing threshold

was investigated. Some trajectories hit the landing threshold with vertical speeds in excess of 4000 feet/sec. Clearly, this is an unrecoverable attitude- the vehicle passes through the endpoint on its way to its final resting place at the bottom of a very deep crater instead of the end of the runway. Another consideration is angle of bank. Hitting the terminal conditions with strong left drift and extreme right bank angle can be disastrous. Limits on the bank angle are clearly needed. The endpoint conditions that specify a landable attitude have now grown to

$$e(x_f, \dot{x}_f, t_f) = \begin{bmatrix} z_f \\ V_f \\ \dot{z}_f \\ \phi_f \end{bmatrix}$$

Notice that angle of attack is not specified in the endpoint conditions and there is a chance that the vehicle could be near stall. The endpoint conditions as stated above are insufficient to hit a specified point along the trajectory. The landing field is specified by Cartesian coordinates x, y, z as well as a runway heading, specified by the azimuth angle, β . Notice that in the flat earth model, the altitude of the field is assumed to be zero but is not necessarily zero. Endpoint conditions for landing at fields with nonzero elevations are simply accommodated as

$$z_f = z_{field} + z_{offset}$$

The new endpoint conditions for landing at a specified field in a landable vehicle attitude are now specified as

$$e(x_f, \dot{x}_f, t_f) = [x_f \quad y_f \quad z_f \quad \dot{z}_f \quad V_f \quad \beta_f \quad \phi_f]^t$$

The runway heading for the selected landing field can have significant effect on the trajectory because reversing direction requires considerable energy loss during the trajectory. It is entirely possible that a footprint generated with loosely specified endpoint conditions does not contain interior points for feasible trajectories when the

endpoint conditions are more fully specified (such as a runway heading 180 degree from the original vehicle azimuth).

THIS PAGE INTENTIONALLY LEFT BLANK

V. RESULTS

A. DISCUSSION

The following sections discuss the footprint and individual trajectory analysis for several cost functions. Unless otherwise specified, the trajectories for both failed and nominal vehicles use the same initial conditions of

$$e(x_i, t_i) = [x_i \ y_i \ z_i \ V_i \ \gamma_i \ \beta_i \ \alpha_i \ \phi_i]^T$$

With the following values

$$e(x_i, t_i) = [0 \text{ ft} \ 0 \text{ ft} \ 125 \text{ kft} \ \text{Mach 8} \ -1.3^\circ \ 0^\circ \ 0^\circ \ 0^\circ]^T$$

These initial conditions correspond to a point on the entry trajectory after the peak heating and dynamic pressure and are suitable for failure as the vehicle can begin to use its control surfaces to control the trajectory. The initial condition for the angle of attack may be too shallow based on previous work, but it is of little consequence for studying the effects of failure on trajectory replanning and retargeting.

The endpoint conditions for both trajectories are of the form

$$e(x_f, t_f) = [x_f \ y_f \ z_f \ \dot{z}_f \ V_f \ \beta_f \ \phi_f]^T$$

With the following values

$$e(x_f, t_f) = [\text{free} \ \text{free} \ \text{free} \ -500 \pm 1000 \text{ ft/min} \ \text{Mach } 0.15 \pm 0.003 \ \text{free} \ 0 \pm 20^\circ]^T$$

Both vehicles observe a normal force constraint of 3 ± 6 g's. The vehicle experiencing a control surface failure must observe the trim deficiency path constraint while the nominal vehicle is unconstrained by trim deficiency because as shown in Figure 10, the vehicle has adequate control power to trim over the entire flight envelope.

Once the rough footprint boundaries are established for the vehicle experiencing control surface failures, the algorithm's ability to generate trajectories to a specific

landing field and its associated runway is demonstrated. For this case, the Cartesian coordinates and azimuth are no longer free and are replaced with the field x y coordinates, an altitude corresponding to 500 feet above the ground and a corresponding runway azimuth.

B. FOOTPRINT ANALYSIS FOR NOMINAL AND STUCK FLAP TRAJECTORIES

An approximate footprint for the nominal and stuck-flap trajectories can be determined by choosing the cost functions corresponding to minimum and maximum down range distance as well as minimum and maximum cross range distance. The four points form an approximate boundary of the footprint and feasible trajectories to the interior points of the polygon formed by these boundary points should exist. Note that feasible trajectories to exterior points are not ruled out but should be proven for each case. Additional boundary points can be determined by varying the A and B terms in the previous equation $M = Ax(end) + By(end)$.

1. Aerodynamic Considerations

The introduction of a control surface failure can drastically change the aerodynamics of the vehicle. The coefficients of lift and drag for the vehicle experiencing a stuck flap have changed significantly. The constraints on angle of attack resulting from the trim deficiency requirements produce a vehicle which may look the same but flies considerably different. The footprints for the failed and normal trajectories should appear different because of the different aerodynamic configurations and Mach-alpha combinations.

Despite the aerodynamic changes of the failed vehicle, its performance should be a *subset* of the nominal vehicle's performance. This is a valid assumption because the control surface failures encountered in flight limit the control surface deflections to a subset of their nominal values. In other words, the nominal vehicle can fly the same profile as a vehicle with control surface failures simply by voluntary limiting the unfailed control surface deflections to those of the vehicle with the failures. The only difference

becomes semantic; the nominal vehicle “simulates” the failure while the vehicle with the actual failure has no choice but to fly (if it can) with the current failed conditions

2. Footprint Observations and Conclusions

Figure 16 shows the footprints for four selected trajectories: nominal, stuck flap failure with loosely specified endpoint conditions, stuck flap failure with tightly specified endpoint conditions and stuck flap failure with tightly specified endpoint conditions and trim deficiency path constraint. Several things are readily apparent:

a. The footprints for vehicles with failures have *better* minimum downrange performance than that of the nominal vehicle. This was surprising but can be explained by the control allocation algorithm. Recall that for a given Mach-alpha pair, the control allocator computes a vector of control deflections that simultaneously balance the moments produced by the wing-body and minimize the 1-norm of the control deflection vector. Changing the preference vector to maximize trim-drag or control deflections within the control allocator can solve this particular issue; however, the differences in the footprints are indicative of greater problems associated with having the outer loop decoupled from the inner loop.

b. There is great variance between the three footprints of the failed vehicles. The largest footprint for the failed vehicles represents the traditional footprint for a failed vehicle as found in the literature. One such approach to determining this footprint uses Vinh’s [Ref 23] equations. The footprint uses loosely specified end point conditions (altitude and airspeed), and does not prevent the angle of attack-Mach combination from entering regions of the flight envelope where the vehicle cannot achieve moment equilibrium due to a lack of control power. As such, the larger footprint depicts where the “pieces fall” since in the early moments following a failure, the trajectory would violate the trim deficiency constraint and the vehicle would become uncontrollable and break up.

c. The effect of more restrictive endpoint conditions further reduces the footprint. The third largest footprint represents the footprint for the trajectory for the failed vehicle that observes the trim deficiency path constraint. While this trajectory appears to be sufficient, further inspection reveals that the endpoint conditions are met

with a vertical speed of nearly 20,000 feet per minute. The vehicle meets the endpoint conditions on its way to a deep crater as there is insufficient remaining altitude to slow the rate of descent to an acceptable level. The smallest footprint represents a trajectory for the failed vehicle with tightly specified endpoint conditions that limit the vertical speed and angle of bank to levels that permit landing. This footprint for a “landable vehicle” in the failed condition is 1% of the area of the largest failed footprint and shows that trajectories generated using energy analysis with loosely specified endpoint conditions and without trim deficiency path constraints result in overly optimistic footprint estimates.

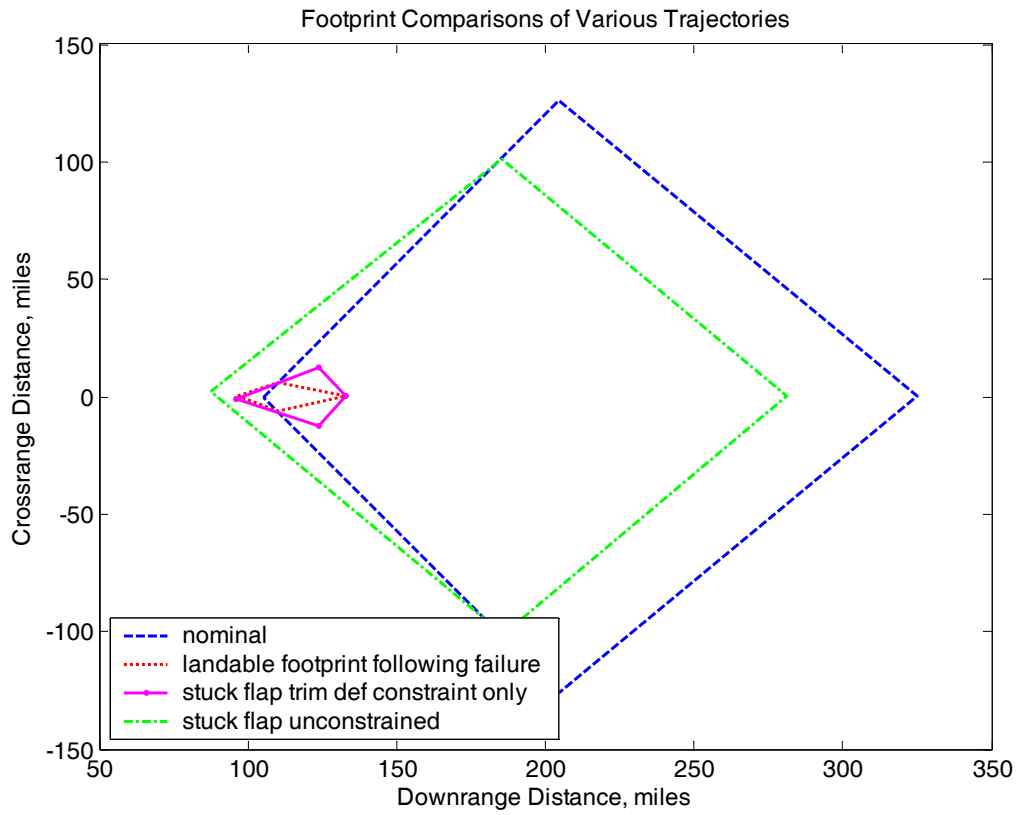


Figure 16 Comparison of Nominal and Stuck-Flap ($+26^\circ$) Footprints

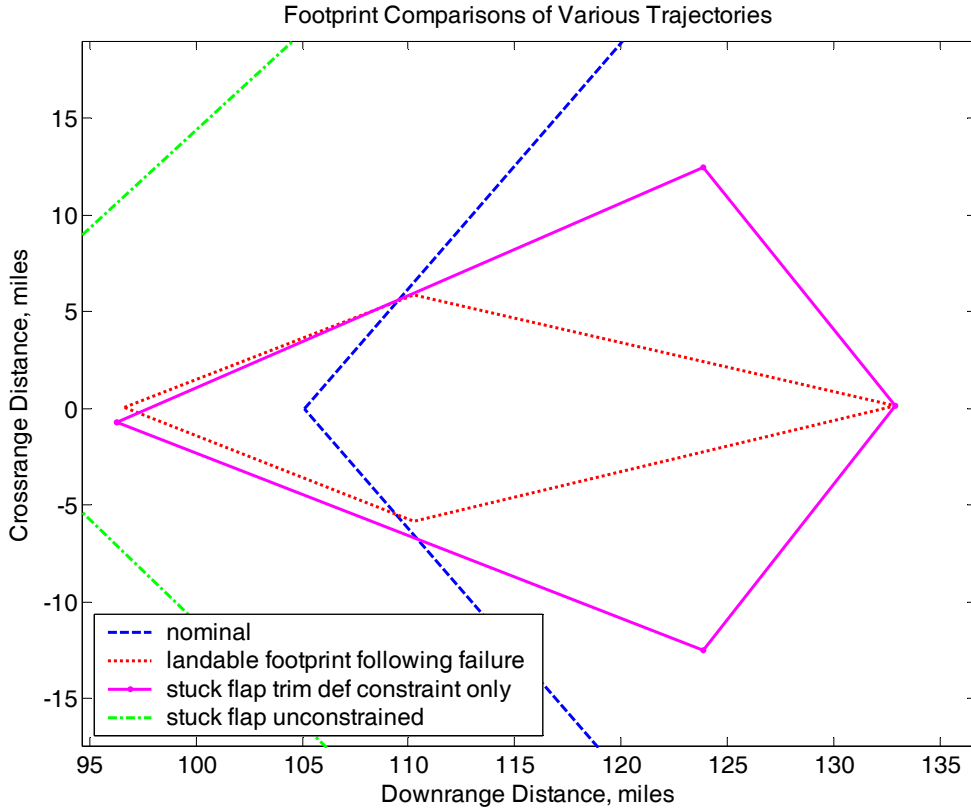


Figure 17 Contraction of Failure Stuck-Flap ($+26^\circ$) Trajectory Footprint

The difference between a “landable” and “unlandable” footprint is shown in Figure 17. Notice that the introduction of vertical speed into the endpoint set reduces the footprint noticeably. Landable footprints result from trajectories with endpoint conditions that allow a safe transition from the landing threshold to weight on wheels and rollout that are within the vehicle and payload performance parameters.

3. Maximum Downrange

The following trajectories for the nominal and failed vehicle were conducted as part of the rough footprint analysis. The performance criterion for these trajectories was to maximize the downrange position at the end of the trajectory. The following trajectory analysis is a detailed comparison of the nominal and failed vehicle trajectories for each associated cost function.

a. Mach-Altitude Profile

The Mach-altitude profiles for both trajectories are shown in Figure 18 . Notice that the nominal trajectory trades excess speed for altitude. At the top of the zoom climb, the vehicle assumes the best lift/drag configuration and continues to the surface. The trajectory for the vehicle with the stuck flap is prevented from using the same combination of angle of attacks as the normal because of the imposed trim deficiency requirement. The trajectory does use the largest allowable angle of attack but this is insufficient to produce the zoom climb observed in the nominal trajectory.

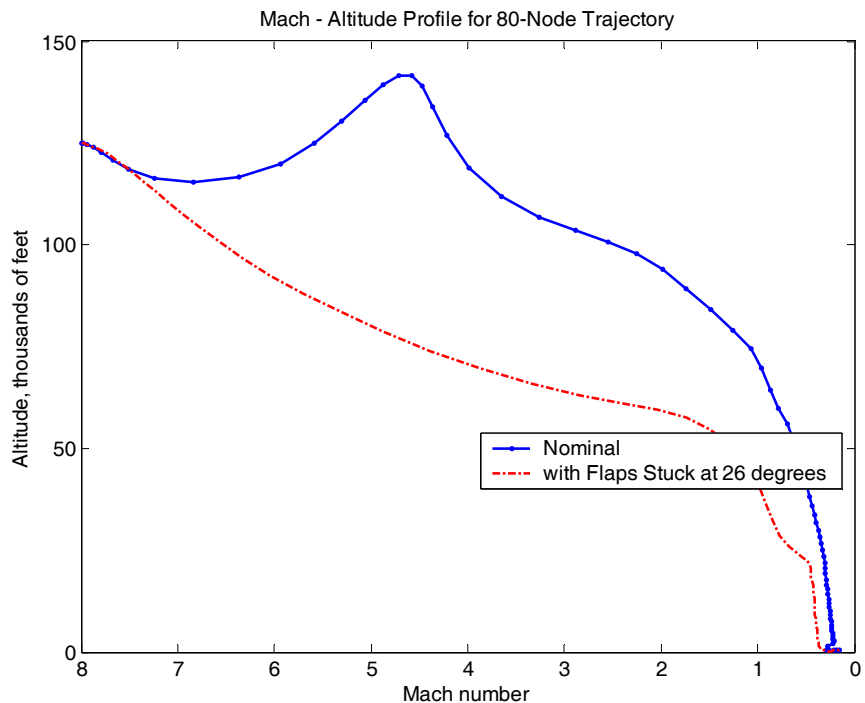


Figure 18 Maximum Downrange Mach-Altitude Profile

b. Trajectory in Cartesian Coordinates

Figures 19-22 depict the Cartesian coordinates of the trajectory. The x , y , and z coordinates are direct results of the controls and the time of their applications. The only performance measure for these trajectories is to maximize the downrange (x). There is no limit placed on crossrange (y) and the altitude must meet the endpoint condition of 500 feet.

The downranges for the failed and nominal trajectories differ by nearly 200 miles. This is not unreasonable considering that the symmetrical flap failure drastically increases the drag on the vehicle. This drag when combined with the imposed trim deficiency path constraint considerably slows the vehicle and prevents it from trading altitude for velocity. The total trajectory time of flight is much shorter.

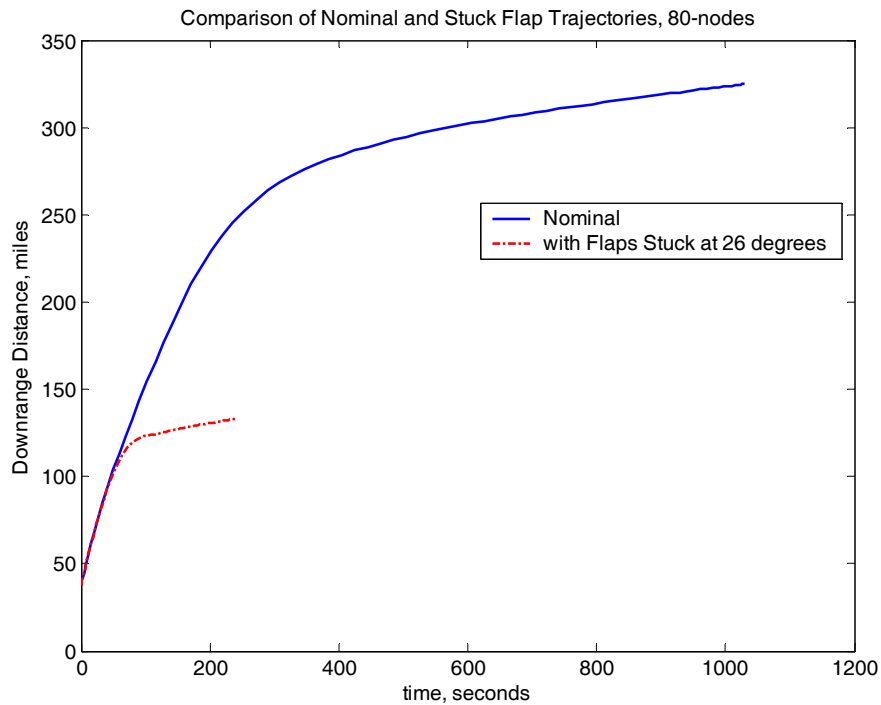


Figure 19 Downrange Profile for Maximum Downrange Trajectories

The crossrange profiles of both trajectories exhibit some unexpected left drift. This drift is insignificant when compared with the total downrange distance of the trajectory. The cause of the drift is unknown and may be numerical. From a physical point of view, the aerodynamics of both the failed and nominal vehicles is symmetrical as is the model used for the trajectory. Closer examination of the control allocation and aerodynamic data may yield answers. One obvious difference between the two trajectories is that the nominal trajectory drifts slowly to the left while the vehicle with

stuck flaps experiences both left and right drift along the trajectory. The angle of bank should be inspected to correlate the drift in crossrange.

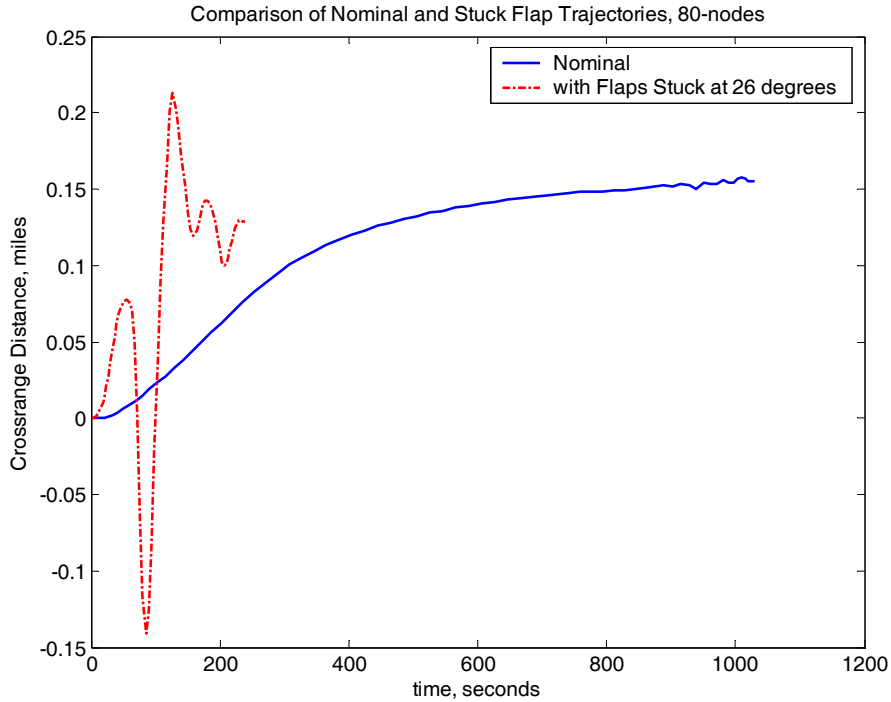


Figure 20 Cross Range Profiles for Maximum Downrange Trajectories

The altitude profiles have been discussed in some detail previously, but an interesting event occurs near the end of each trajectory. Both trajectories overshoot the endpoint altitude of 500 feet and appear to perform identical maneuvers to meet the 500 foot altitude requirement at the endpoint condition. This event was surprising not only because of the nearly identical maneuver, but also because the trajectory actually indicated a climb in the last moments of the trajectory. The encroachment below 500 foot altitude was allowed by the problem formulation; the only limit placed upon the z state variable was that it had to be nonnegative.

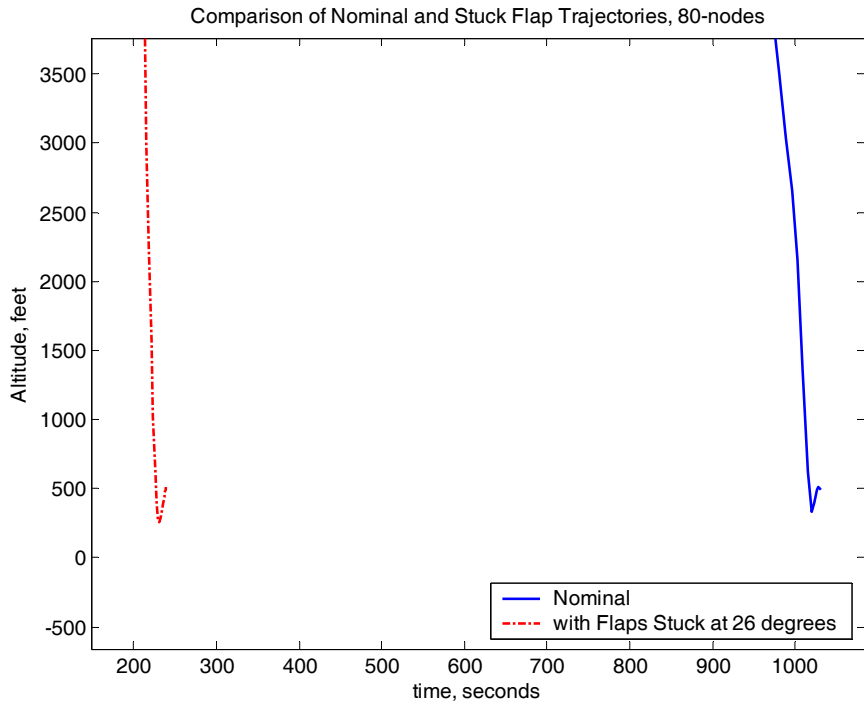


Figure 21 Terminal Maneuver for Max Downrange Trajectories

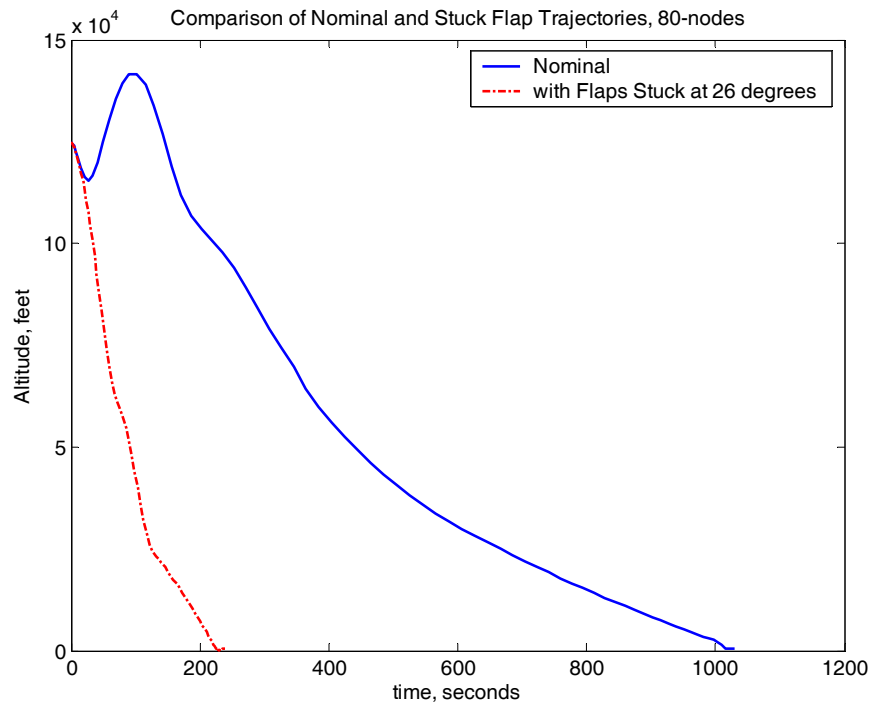


Figure 22 Altitude Profiles for Max Downrange Trajectories

c. Velocity Profiles

Figure 23 depicts the velocity profiles for the max downrange trajectories.

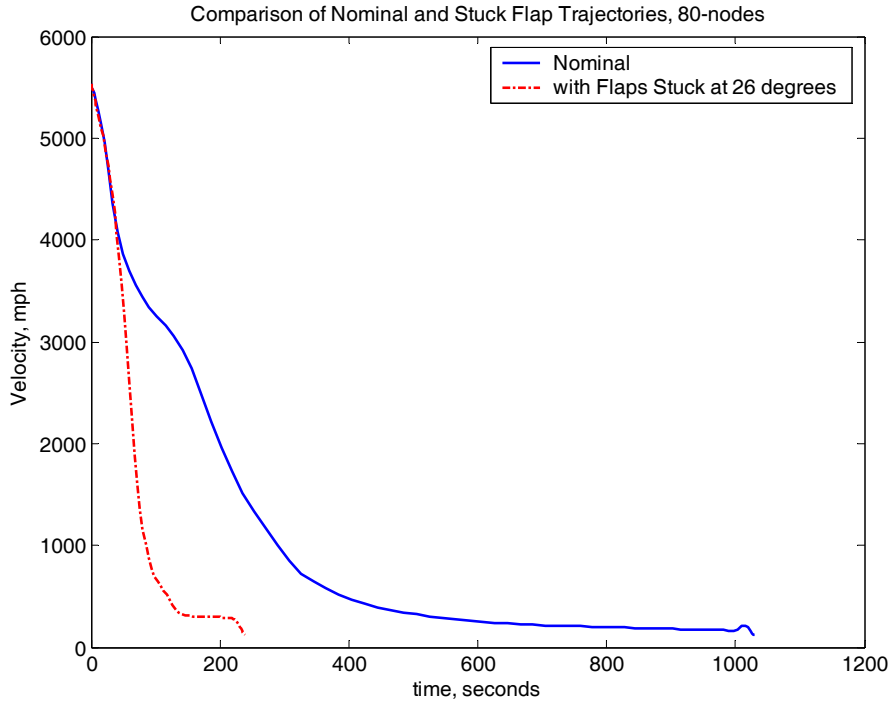


Figure 23 Velocity Profiles for Max Downrange Trajectories

d. Flight Path and Azimuth Angle

The flight path angles (FPA) shown in Figure 24 for these two trajectories differ as a consequence of the controls available to the individual vehicles. The failed vehicle exhibits a very steep descent but ends the trajectory with a terminal maneuver similar to the nominal trajectory. The similarity of the terminal maneuvers is a direct result of the endpoint conditions shared by the two trajectories.

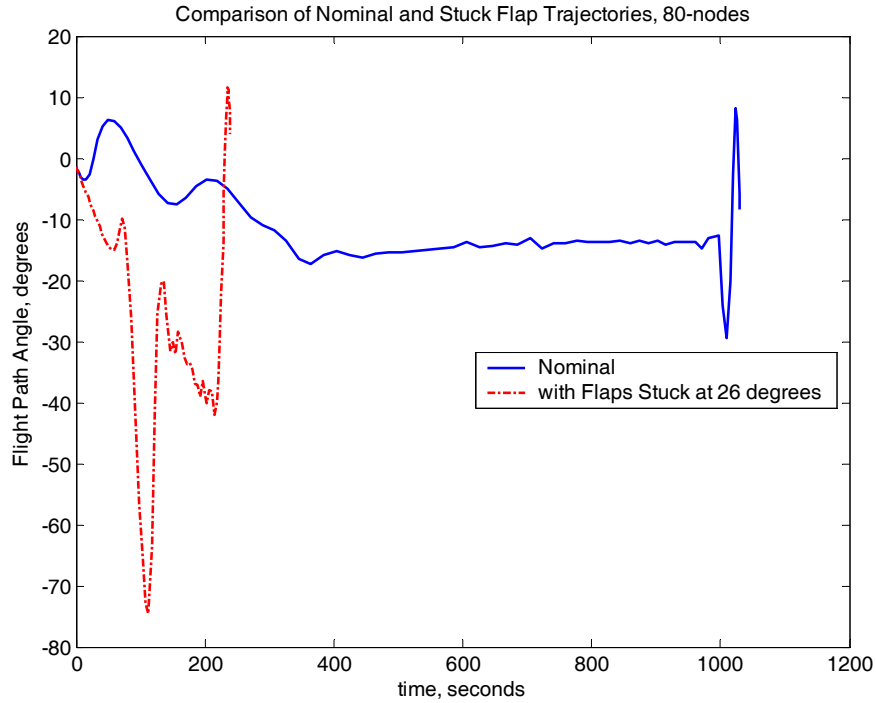


Figure 24 Flight Path Angle Profiles for Max Downrange Trajectories

There is no limit placed upon the azimuth angles for these trajectories and both vehicles wander somewhat in azimuth. The average azimuth of both trajectories in Figure 25 is positive and accounts for the left bias of the crossrange. Notice the nominal trajectory has the most stable azimuth between 100 and 700 seconds. The stable azimuth is small and positive and accounts for the steady left drift found in the nominal trajectory. The vehicle experiencing the stuck flap is far less stable and the azimuth varies by as much as 11 degrees.

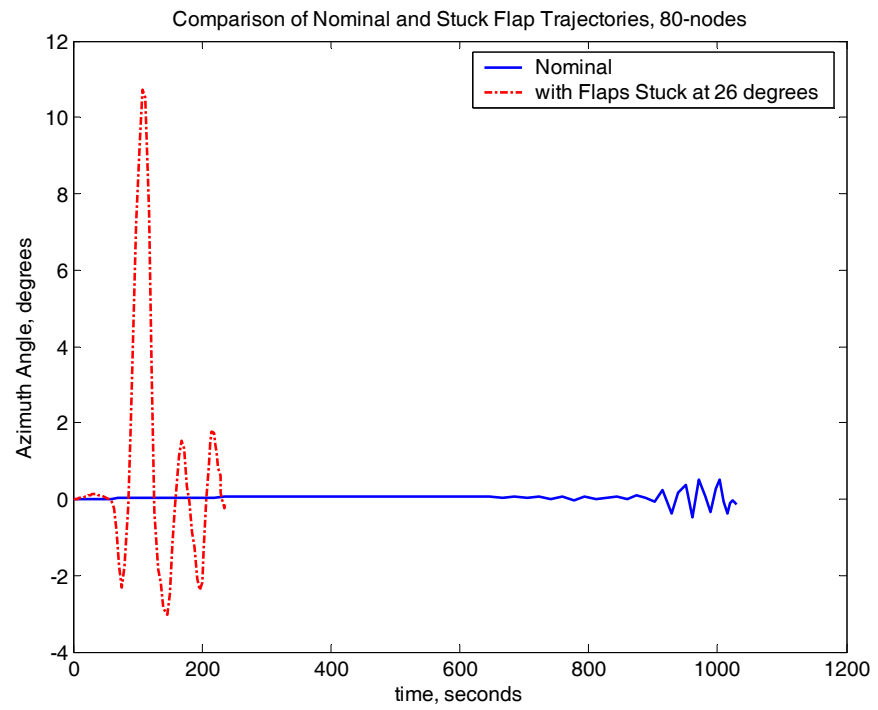


Figure 25 Azimuth Angle Profile for Max Downrange Trajectories

e. Vertical Speed Profile

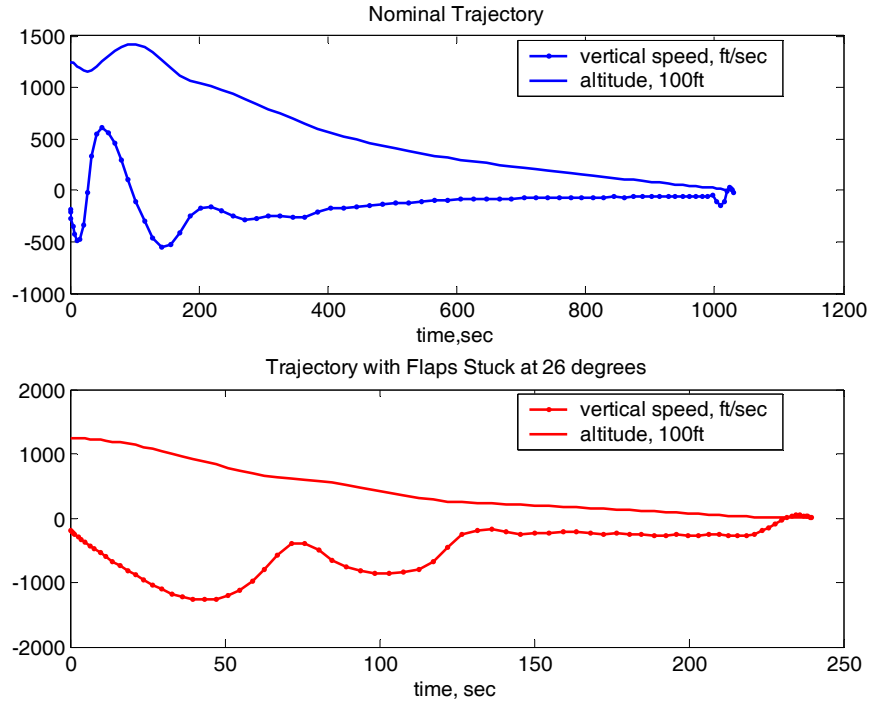


Figure 26 Vertical Speed Profiles for Nominal and Failed Trajectories (Max Downrange)

f. Body Frame Normal Force

The normal force experienced by the vehicle for both trajectories are depicted as functions of time and distance. As expected, the vehicle with the control surface failure has a more varied normal force profile with larger force excursions. Both vehicles have increases in normal force at the terminal maneuver as shown in Figure 27. Additionally, the nominal vehicle is “pulling g’s” during the zoom climb maneuver early in the trajectory.

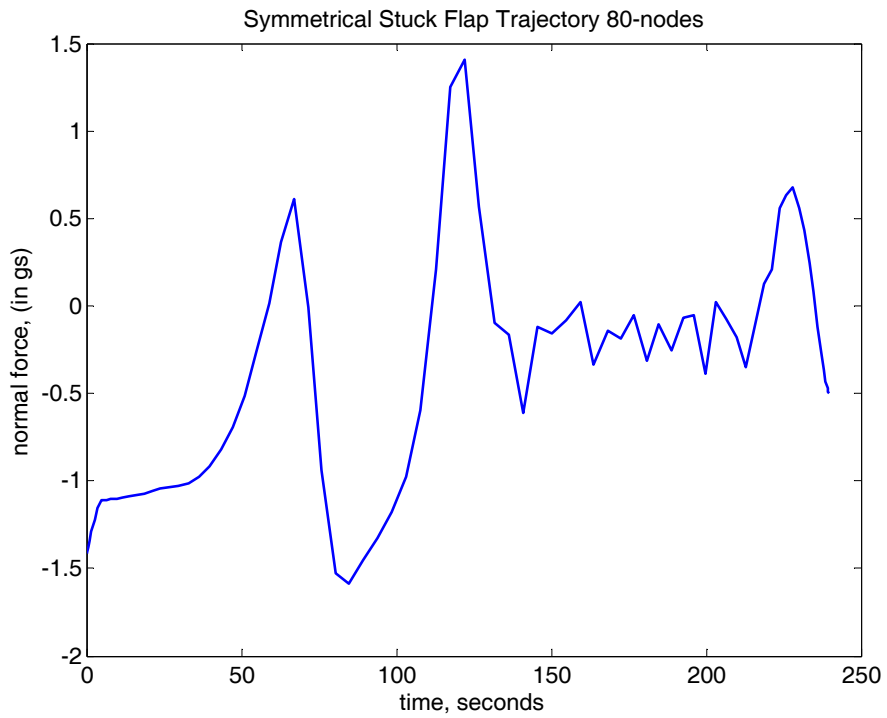


Figure 27 Normal Force ($n_z - 1$) vs. Time for Vehicle with Stuck Flaps

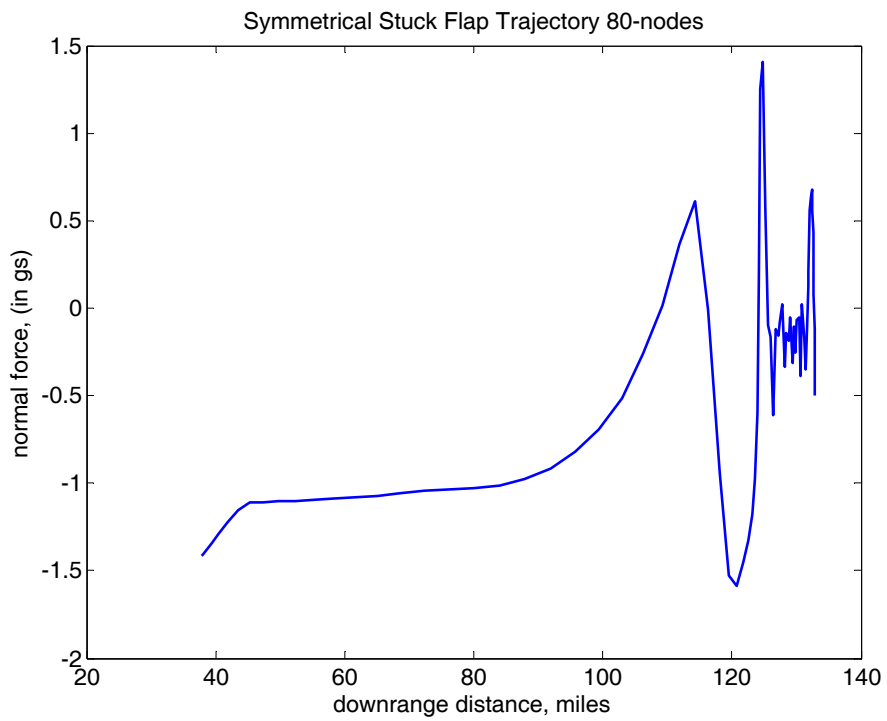


Figure 28 Normal Force ($n_z - 1$) vs. Downrange Distance for Vehicle with Stuck

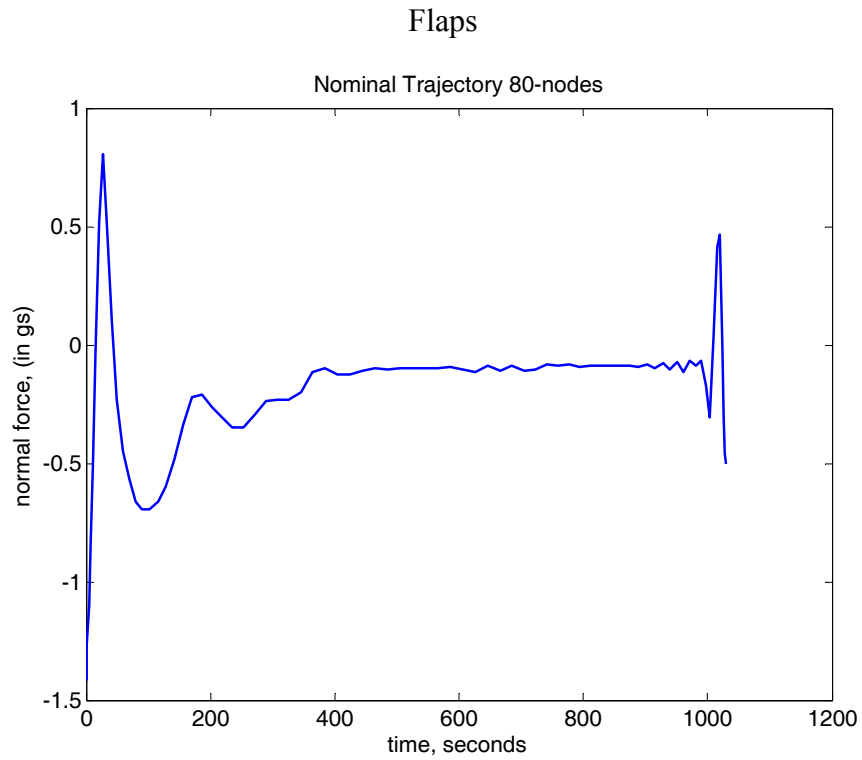


Figure 29 Normal Force ($n_z - 1$) vs. Time for Nominal Vehicle

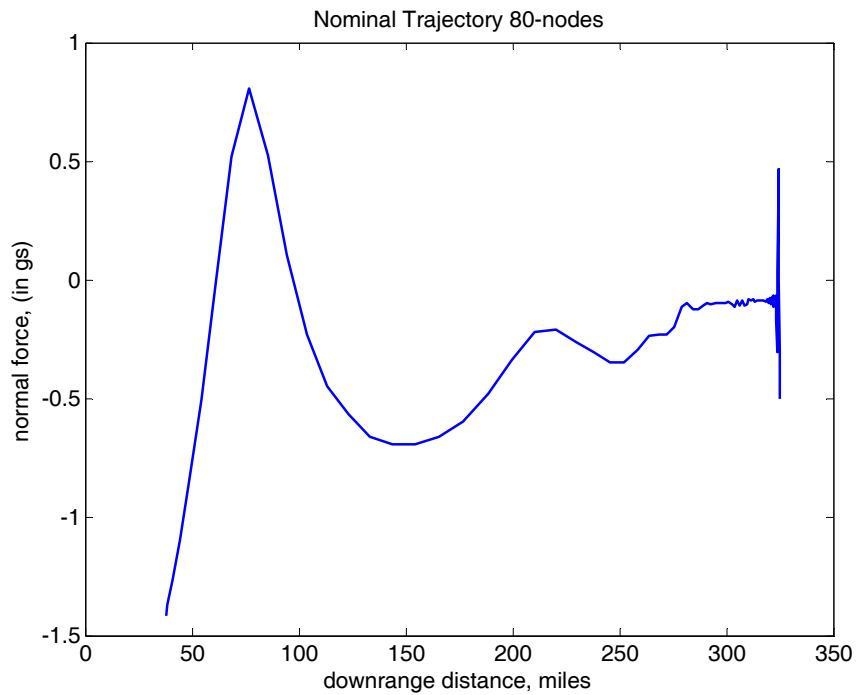


Figure 30 Delta Normal Force($n_z - 1$) vs. Downrange Distance for Nominal Vehicle

g. Controls

While the problem formulation uses pseudo controls to induce inertia into the dynamical model, the physical controls of the vehicle are its angles of attack and bank. The angle of attack profiles clearly demonstrate the effects of the reconfigured aerodynamics and resulting angle of attack limits. The failed vehicle is limited to a much smaller range of angles of attack until the subsonic flight regime at which point it can use the same full range of angles of attack as the nominal trajectory. Both trajectories share the same terminal maneuver. The terminal maneuver is simply a climb that compensates for undershooting the 500 foot final altitude condition. This maneuver can be compared to the terminal maneuver shown in the altitude profile.

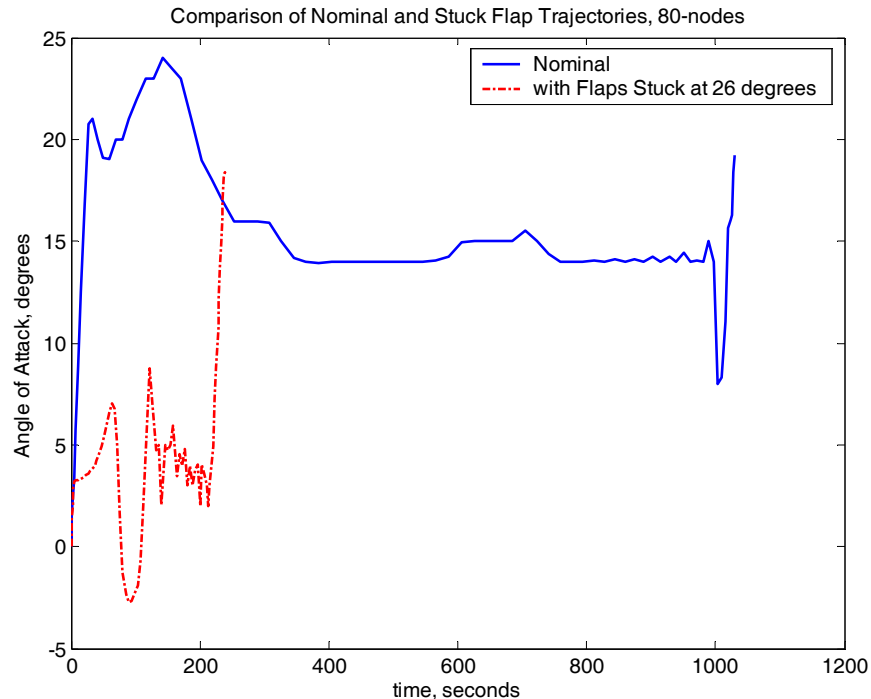


Figure 31 Angle of Attack Profiles for Max Downrange Trajectories

The bank angle profiles are as expected and compare well to the crossrange profiles previously discussed. The nominal vehicle is relatively steady all the way to the endpoint conditions where it gets a little chatter while the vehicle with the stuck flaps has bank angle excursions as large as 27 degrees.

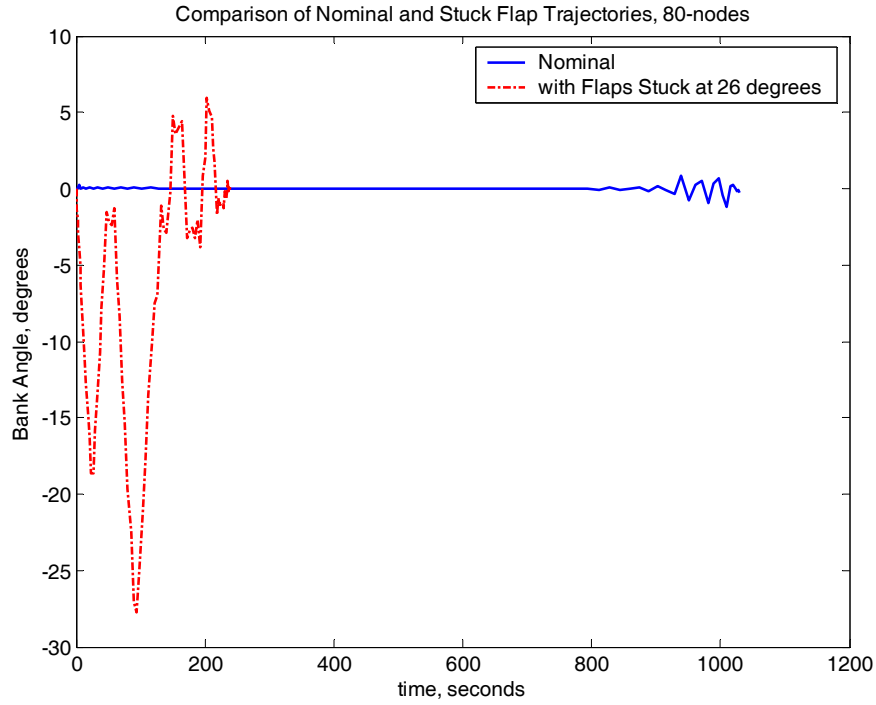


Figure 32 Bank Angle Profiles for Max Downrange Trajectories

h. Pseudo Controls

The pseudo controls depicted are not the true controls, but rather the control rates. The profiles show that while the majority of the maneuvers request the controls at the maximum rate available (the pseudo controls are *rate limited*), not every maneuver requires full control surface rates. The points where the pseudo controls are limited provide excellent insight into the optimality of the solution by examination of the necessary conditions.

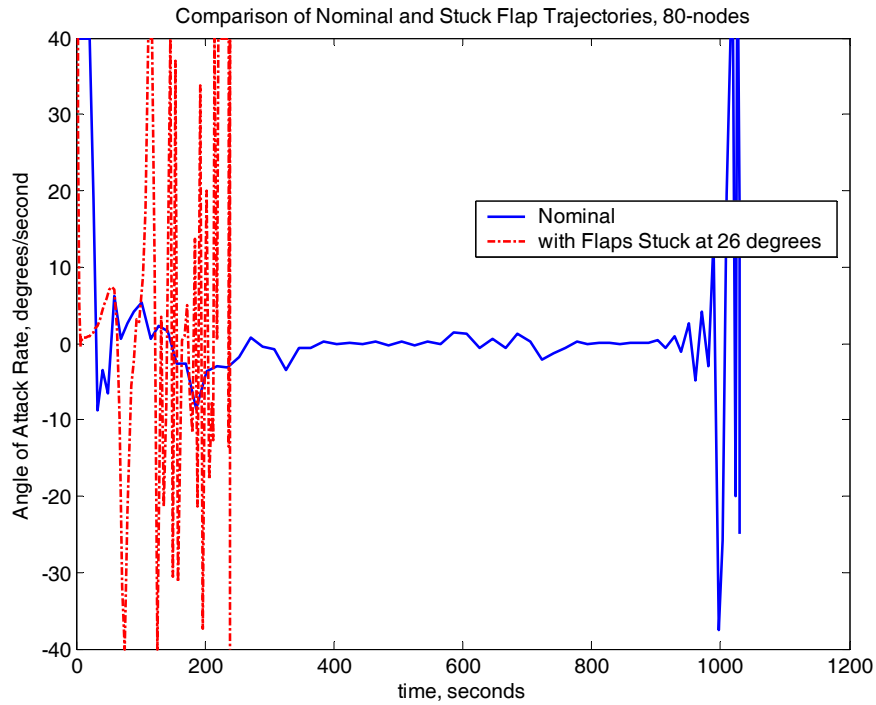


Figure 33 Angle of Attack Rate Profiles for Maximum Downrange Trajectories

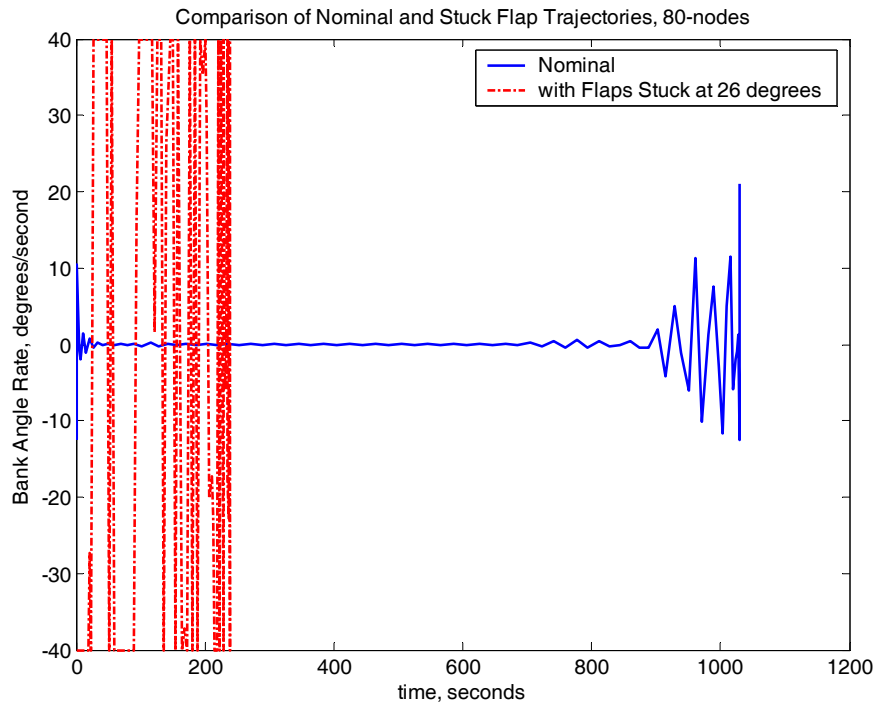


Figure 34 Bank Angle Rate Profiles for Maximum Downrange Trajectories

i. Trim Deficiency

The restricted region in Mach-alpha space, due to the moment trim deficiency for the vehicle with stuck flaps, imposes severe trajectory performance penalties as previously shown. Figure 35 is meant to show the differences between the two trajectories in Mach-alpha space as well as to provide visual verification that the trajectory for the vehicle experiencing flap failure does not violate the imposed trim deficiency constraint of 0.003 and instead closely follows the contour in regions where the constraint is active.

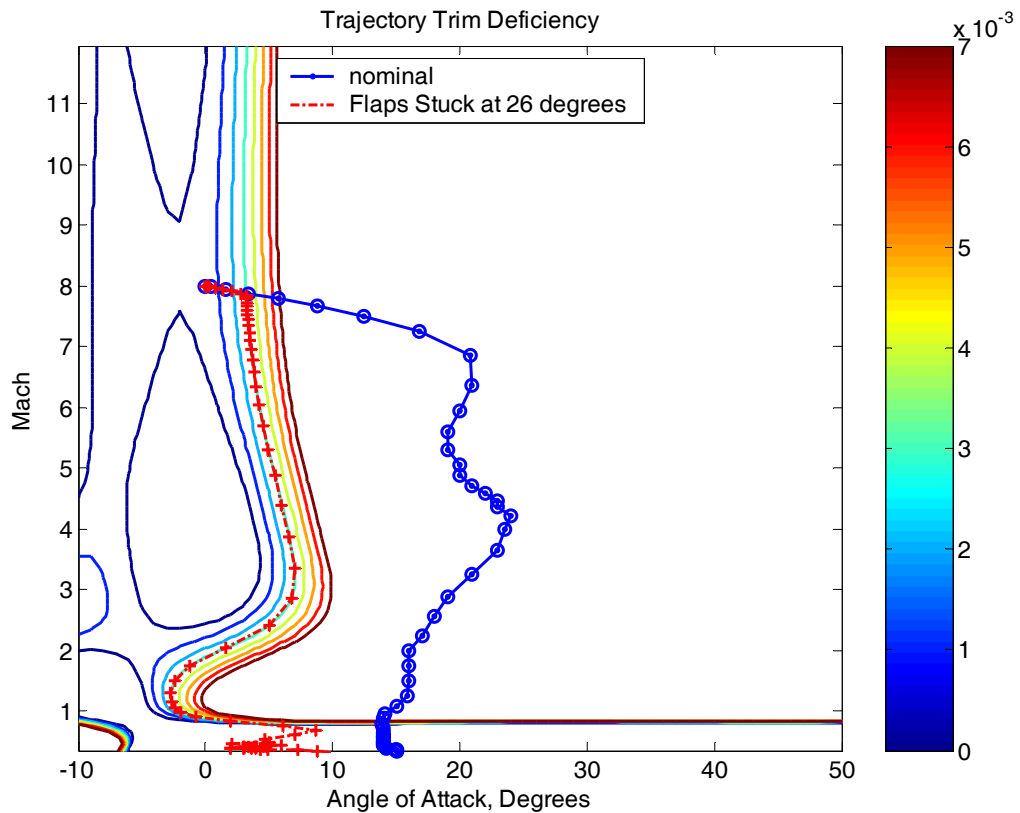


Figure 35 Trim Deficiency Map for Max Downrange Trajectories

j. Optimality Analysis

The optimality of the two trajectories can be shown by investigating the Hamiltonian and necessary conditions. The Hamiltonian for these trajectories should be zero. Several problems inherent with the trajectory problem as posed can prevent DIDO

from identifying a locally optimal solution and instead characterize the solution as “near optimal” where the cost *may be* within 99.999% of optimal. The two major problems which lead to “near optimal” solutions are

1. The use of nonsmooth data. In this case, the aero data tables are not smooth and can cause some difficulty in the Jacobian matrices used in the DIDO code.

2. Insufficient number of nodes used in the solution. This is a tradeoff between execution time and accuracy. If a 40-node solution yields propagation errors of acceptable magnitude along with a near-optimal solution, it may be undesirable to increase the execution time to find a locally optimal solution, if it exists.

Both nominal and stuck flap trajectories used an 80-node solution which resulted in a near-optimal solution determination. The Hamiltonians are not exactly zero but are close. The stuck flap trajectory Hamiltonian is not as smooth as expected but investigation of the necessary conditions shows appropriate switching of the dual for constrained controls.

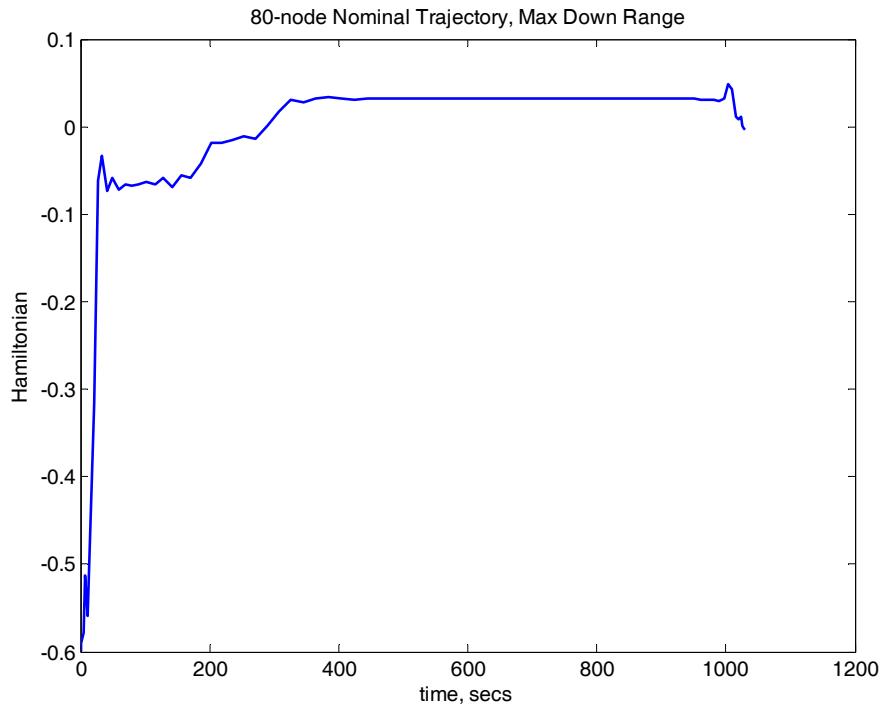


Figure 36 Hamiltonian for Max Downrange Nominal Trajectory

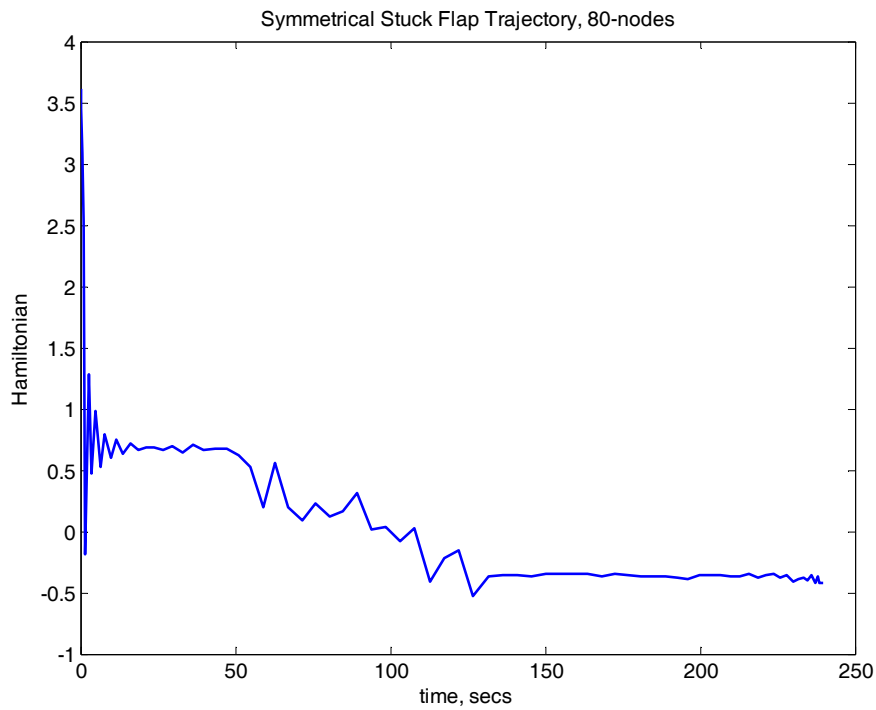


Figure 37 Hamiltonian for Vehicle with (26 deg) Stuck Flaps

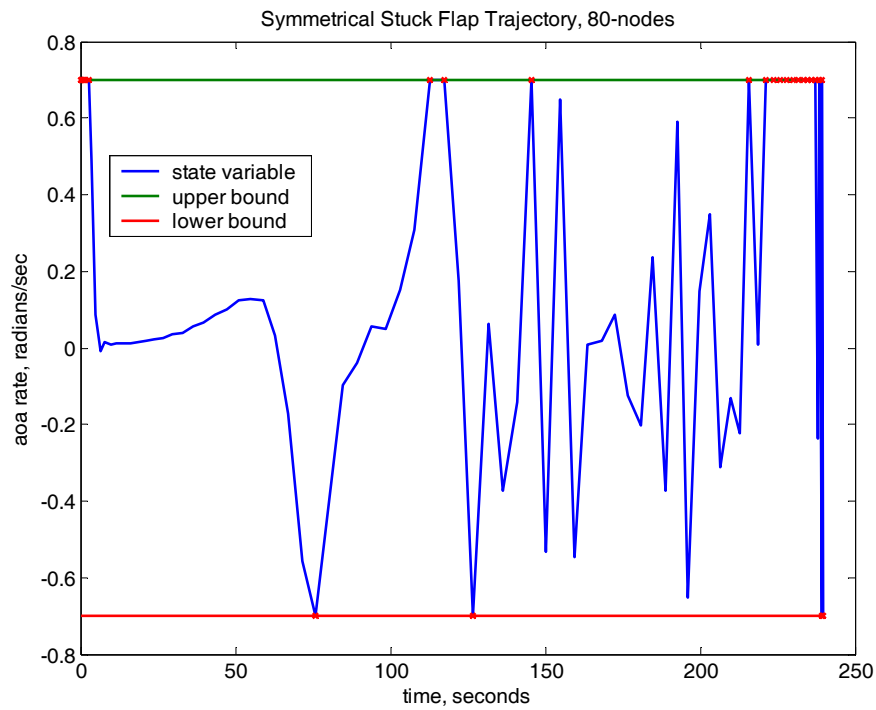


Figure 38 Constrained Pseudo Controls for (26 deg) Stuck Flap Trajectory

The pseudo controls for the vehicles experiencing the stuck flaps are generally constrained throughout the trajectory as shown in Figure 38 and Figure 39. The rapid switching between extreme pseudo control rates is a close approximation of bang-bang control. The necessary conditions for the pseudo controls are satisfied when the duals for both angle of attack and bank angle rates are positive for upper-bounded control rates and negative for lower-bounded control rates as shown in Figure 40 and Figure 41.

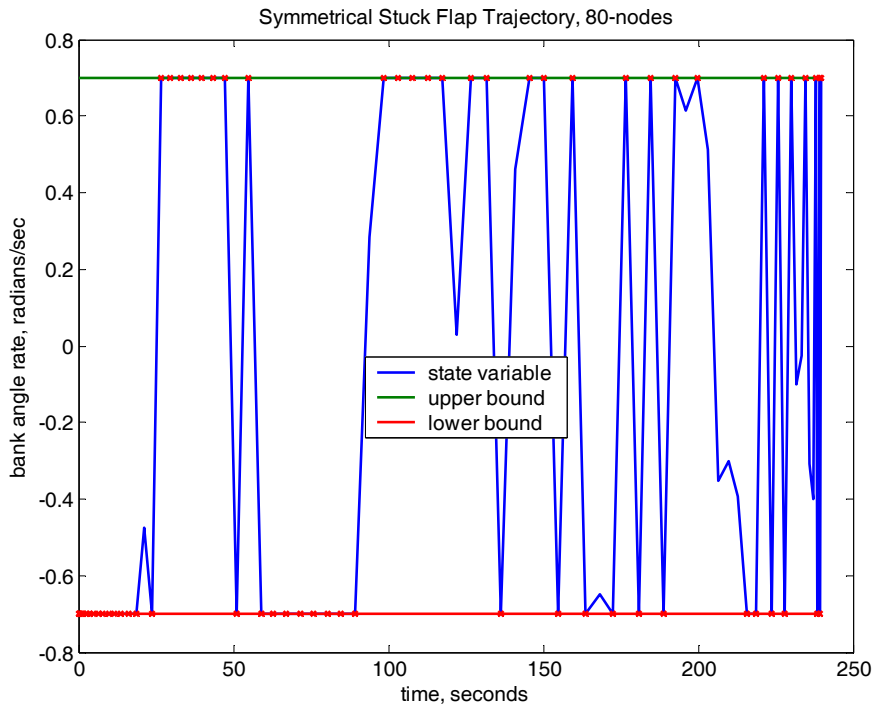


Figure 39 Upper and Lower Bounded Bank Angle Rate for (26 degree) Stuck Flap Trajectory

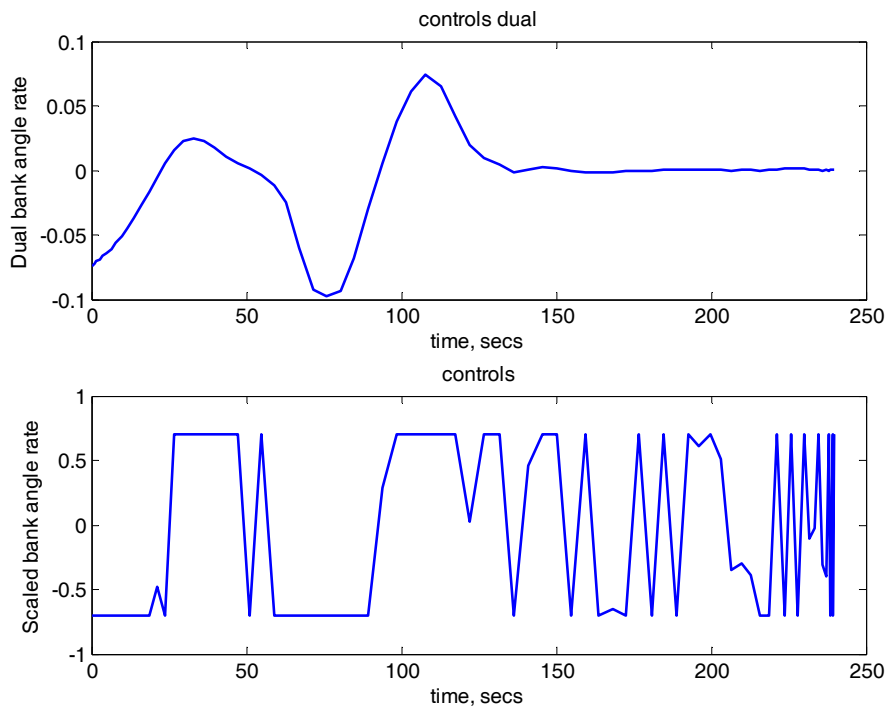


Figure 40 Bank Angle Rate and Associated Dual for (26 deg) Stuck Flap Trajectory

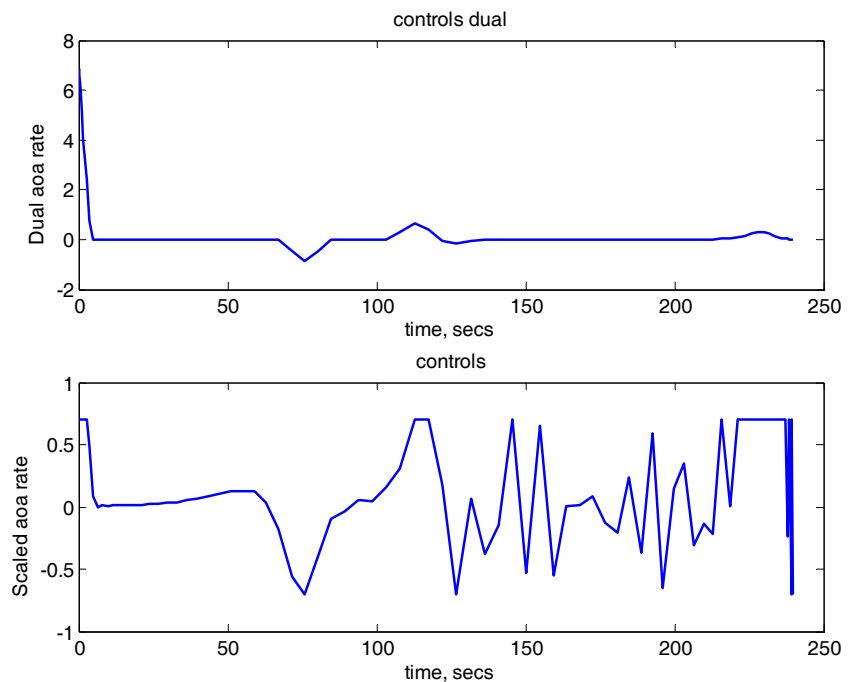


Figure 41 Angle of Attack Rate and Associated Dual for (26 degree) Stuck Flap Trajectory

k. Feasibility

The feasibility of the trajectory is demonstrated by propagating the DIDO controls using an R-K algorithm and comparing the DIDO and propagated state vectors at the endpoint. There is an obvious tradeoff –a trajectory that seeks to place the vehicle in a landable attitude at the landing threshold of a runway needs sufficient accuracy at the endpoint conditions that does not place the vehicle in danger. The accuracy of an 80-node solution is generally sufficient. The errors in the corresponding components of the state vector are shown below.

$$\text{error} = [436\text{ft} \ -267\text{ft} \ 79 \text{ ft} \ 11.5 \text{ deg} \ -10 \text{ deg} \ -21 \text{ deg} \ 0.11 \text{ deg/sec} \ -0.63 \text{ deg/sec}]'$$

A graphical depiction of the DIDO and propagated controls is shown in Figure 42

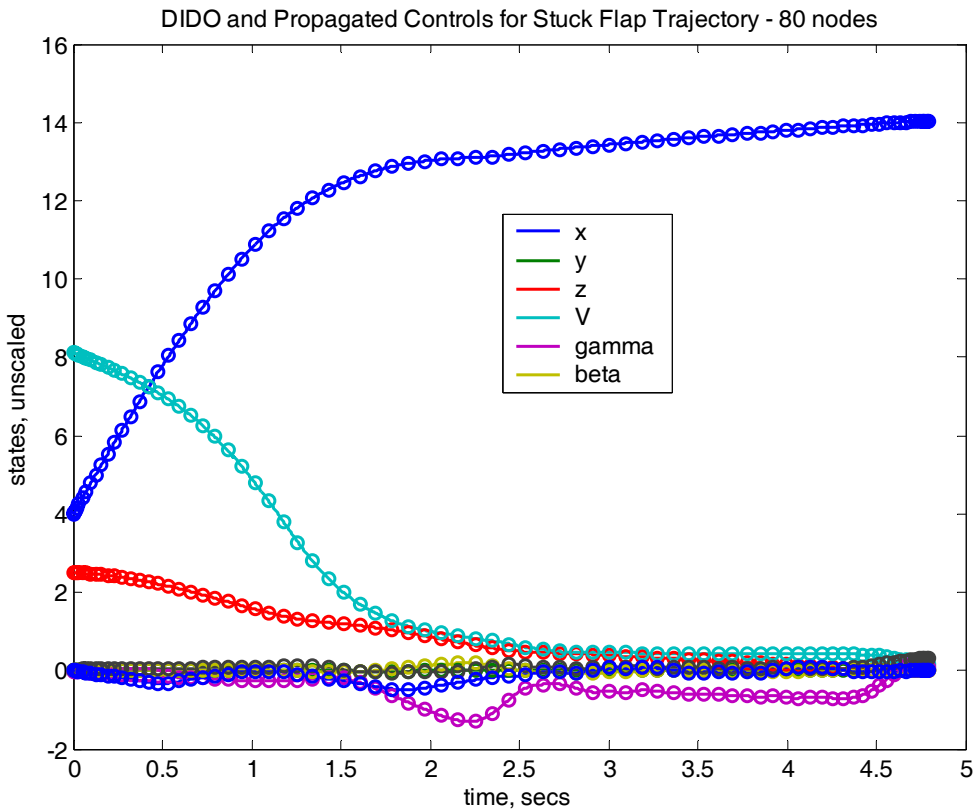


Figure 42 DIDO and Propagated Controls (DIDO controls are denoted by discrete points)

4. Minimum Downrange

a. Mach-Altitude Profile

The Mach-altitude profile for the minimum downrange trajectory produced some unexpected results. The nominal and stuck flap trajectories closely approximate each other until approximately 60,000 feet where the nominal vehicle conducts a zoom climb that approaches stall and then rapidly descends at a high subsonic speed. The point of the climb corresponds to altitude of minimum speed of sound in Figure 7

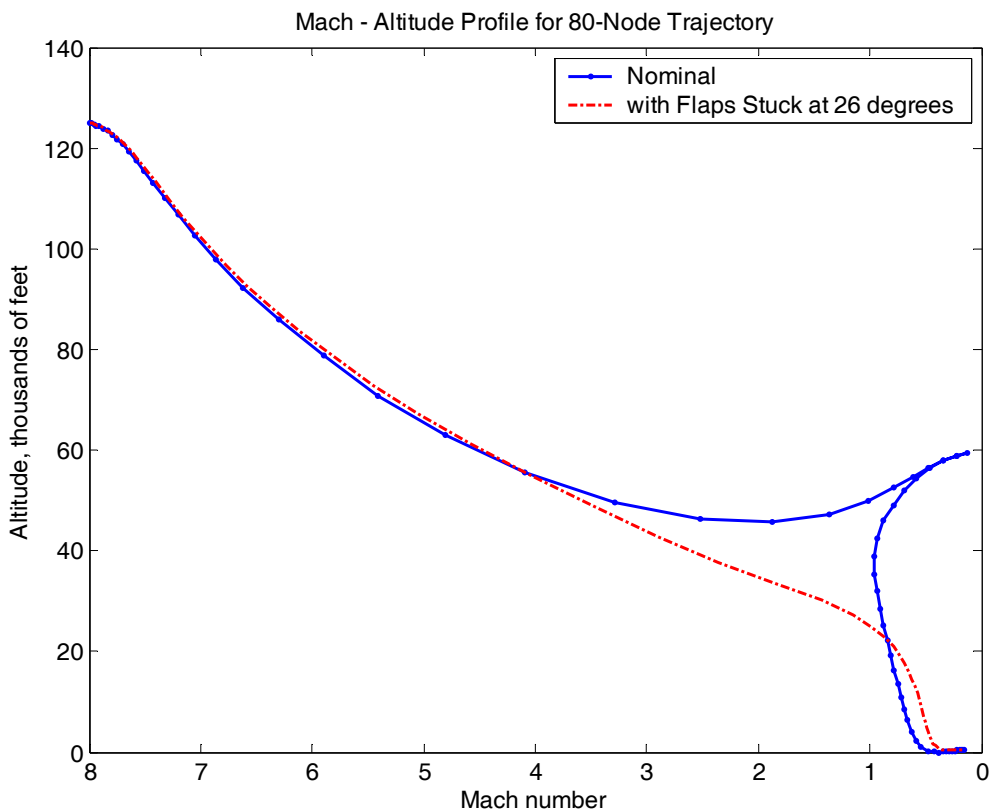


Figure 43 Mach-altitude Profiles for Minimum Downrange Trajectory

b. Trajectory in Cartesian Coordinates

The profiles in Cartesian coordinates for the minimum downrange trajectory are shown in Figure 44 . The stuck flap trajectory shows better minimum downrange performance than the nominal trajectory. This is surprising because the

nominal vehicle has the full available range of control effector positions available while the failed vehicle only has a subset of the available control effector positions. In other words, the performance of the nominal vehicle should never be less than that of the vehicle experiencing a control surface failure. One explanation for the performance difference lies with the control allocation found in the inner loop of the algorithm. Recall that the control effector position vector for the requested angle of attack is optimized to minimize pitching moment using the aero dynamic data and vehicle flight condition (determined by Mach and angle of attack) as arguments. The resulting control effector position vectors are different with each aerodynamic configuration for the same requested angle of attack with accompanying differences in the lift and drag forces experienced by the vehicles. The consequence is nearly 10 miles in additional downrange distance and 100 additional seconds of flight time.

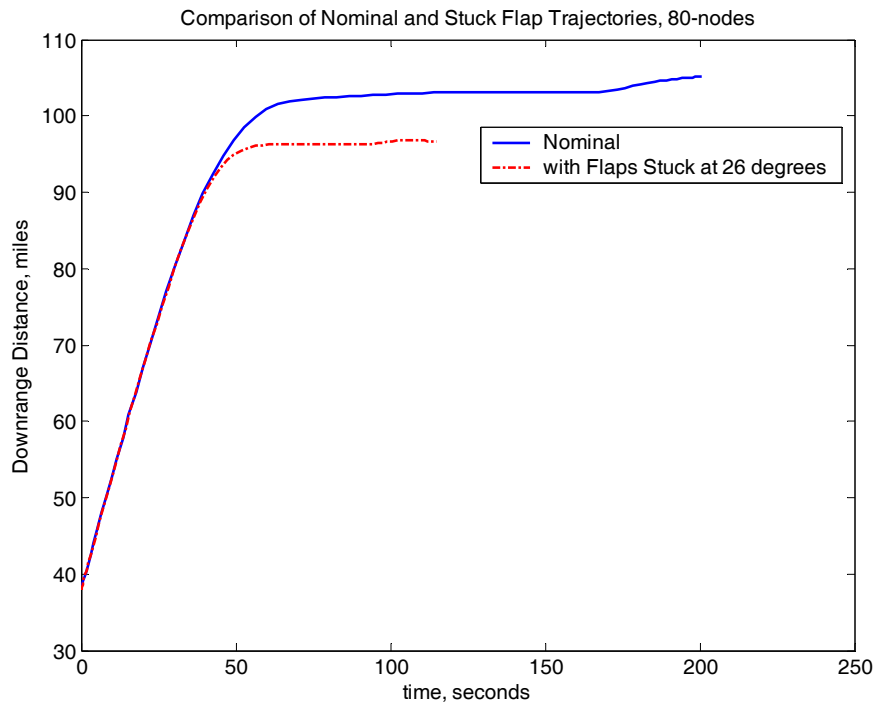


Figure 44 Downrange Distance Profiles for Minimum Downrange Trajectories

The crossrange profile of the vehicle with stuck flaps veers nearly a mile off centerline before attempting to return to centerline while the nominal trajectory remains on centerline throughout the trajectory.

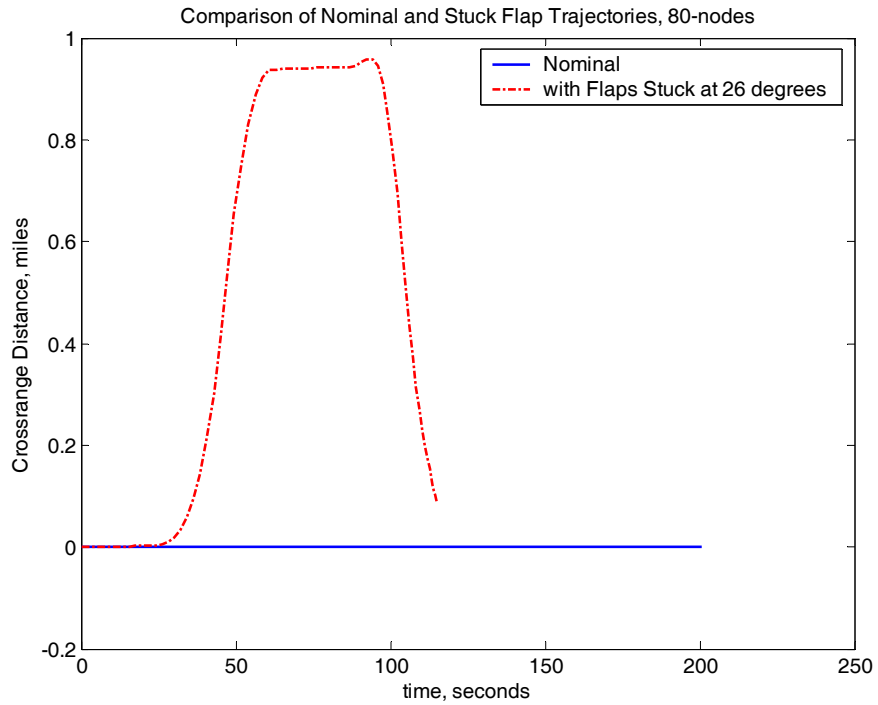


Figure 45 Crossrange Profiles for Minimum Downrange Trajectories

The altitude profile for the nominal trajectory shows the previously pointed out climb at 50,000 feet. Both trajectories exhibit similar terminal maneuvers as those meeting the maximum downrange criterion. The vehicles pass through 500 feet and initiate climbs to meet the endpoint conditions.

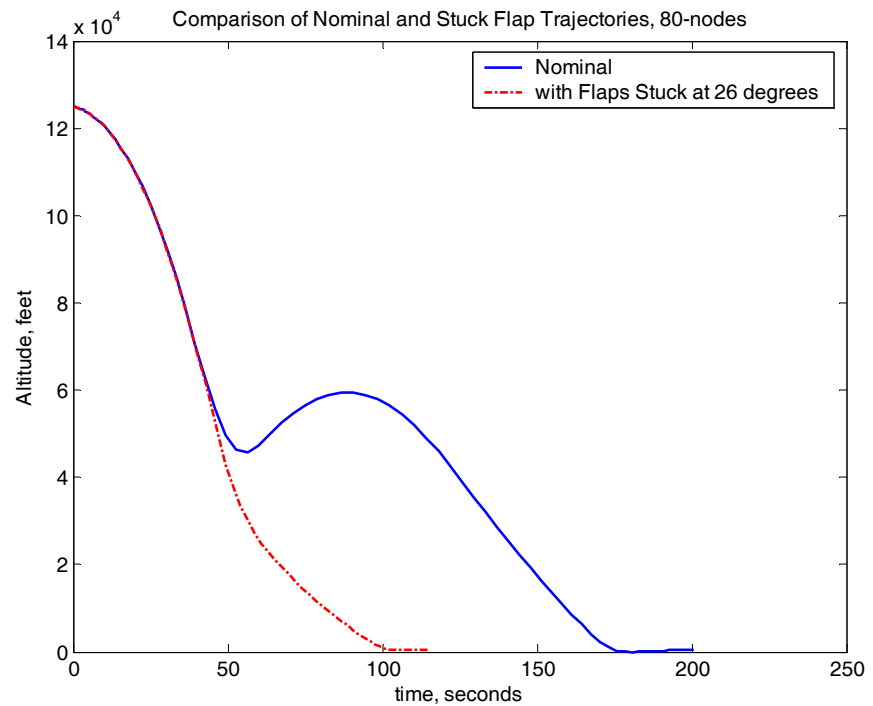


Figure 46 Altitude Profile for Minimum Downrange Trajectories

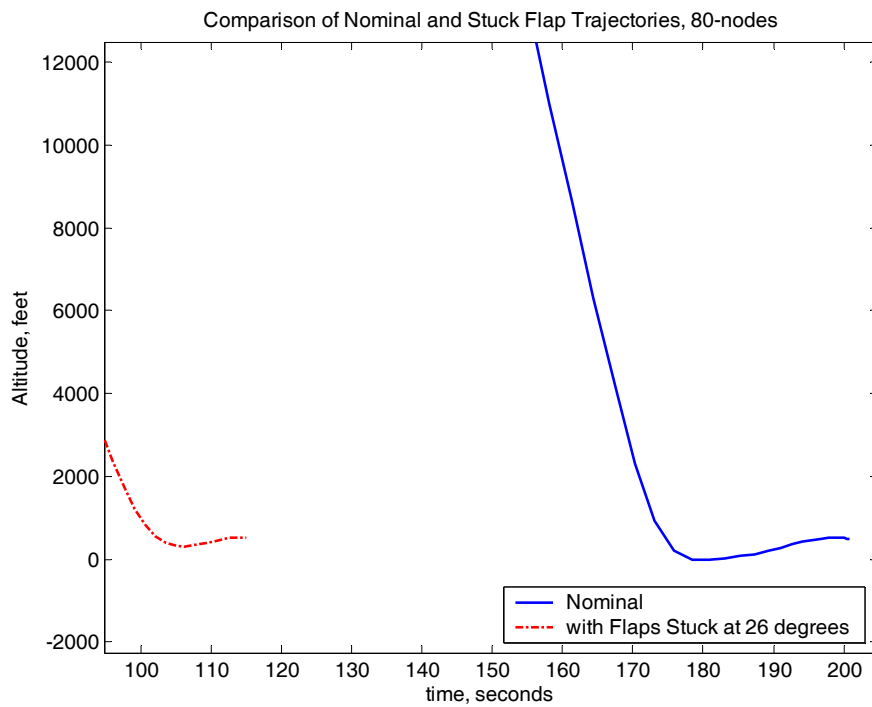


Figure 47 Terminal Altitude Maneuver for Minimum Downrange Trajectories

c. Velocity Profile

The vertical speed profiles are nearly identical until the transonic region at which point they diverge. This divergence is a consequence of the nominal trajectory's zoom climb that occurs at 50,000 feet. The final 30 seconds' velocity profile for both trajectories is very similar.

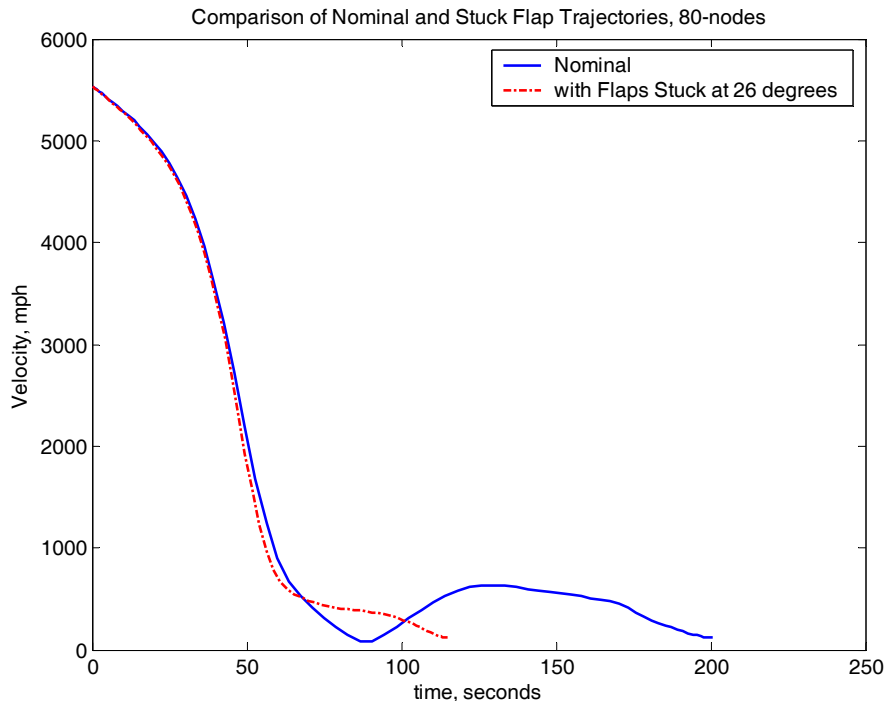


Figure 48 Velocity Profiles for Minimum Downrange Trajectories

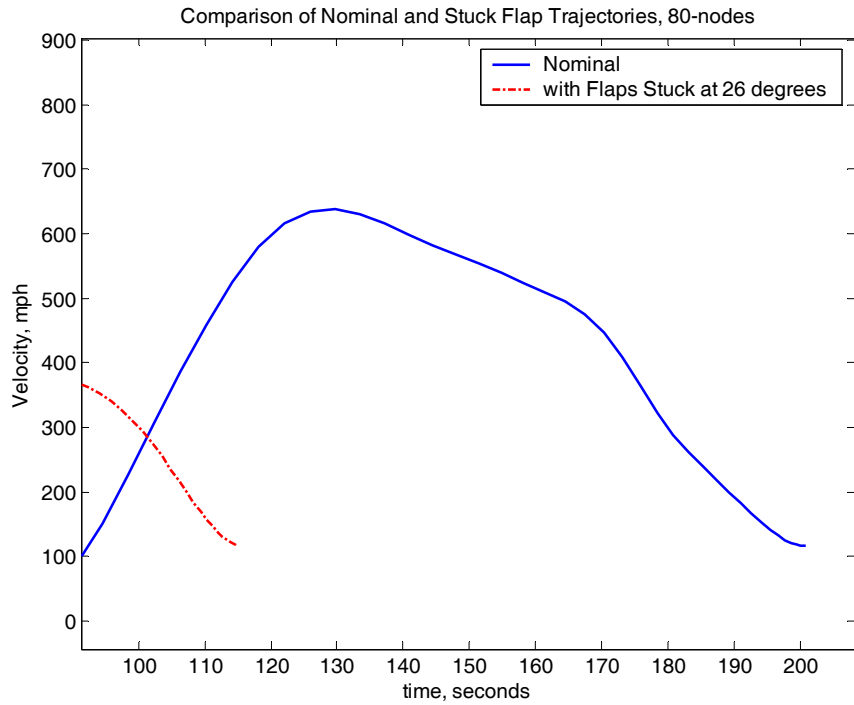


Figure 49 Terminal Velocity Profile for Minimum Downrange Trajectories

d. Flight Path and Azimuth Angle

The terminal flight path angle profile for both trajectories is very similar. The failed vehicle's final azimuth performance is far better than the nominal vehicle with some attempt at ground track reversal in evidence.

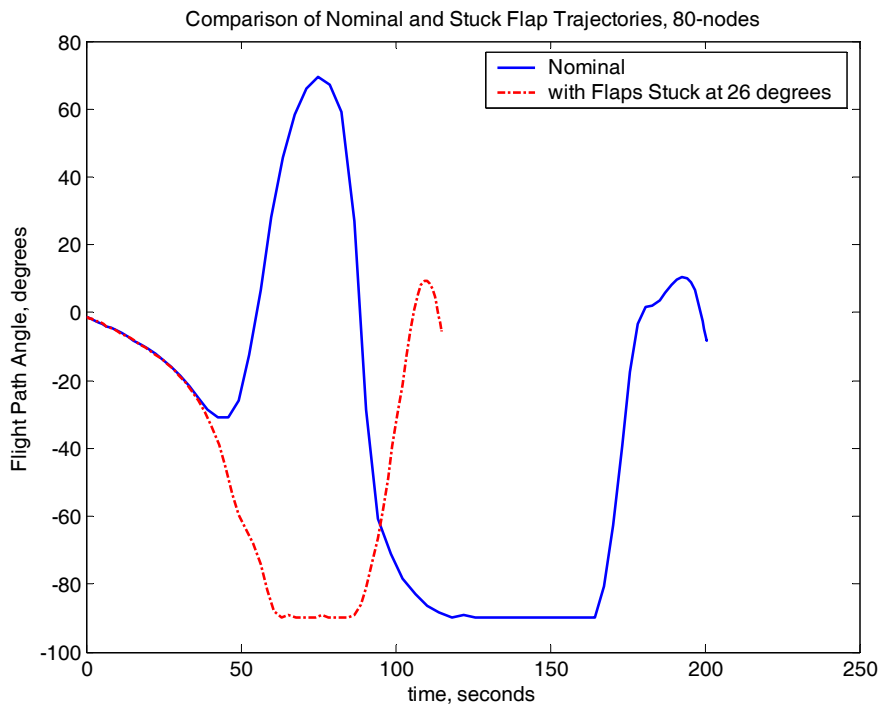


Figure 50 Flight Path Angle Profile for Min Downrange Trajectories

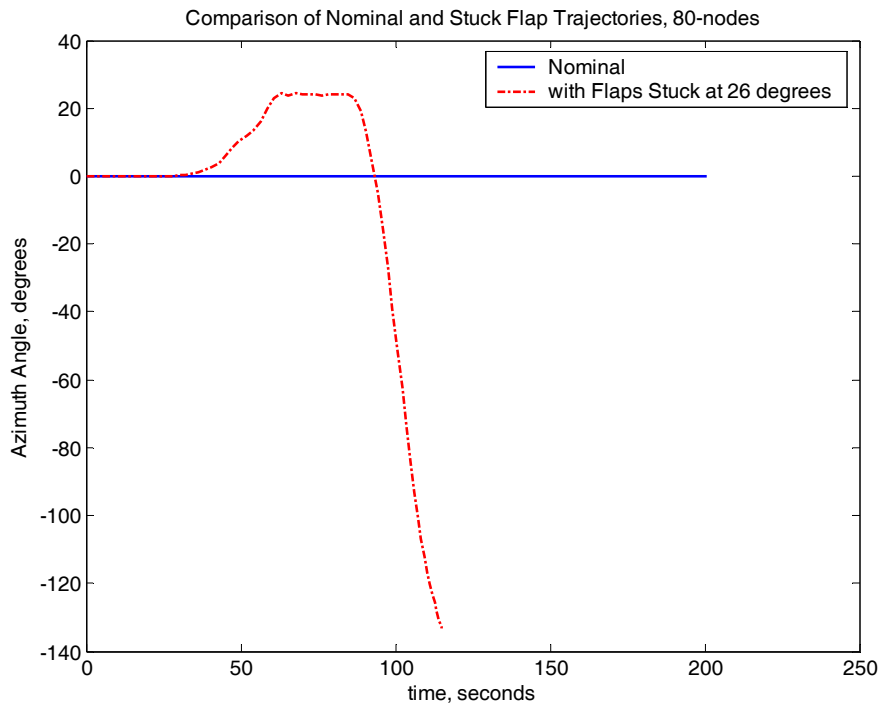


Figure 51 Azimuth Angle Profile for Min Downrange Trajectories

e. *Vertical Speed Profile*

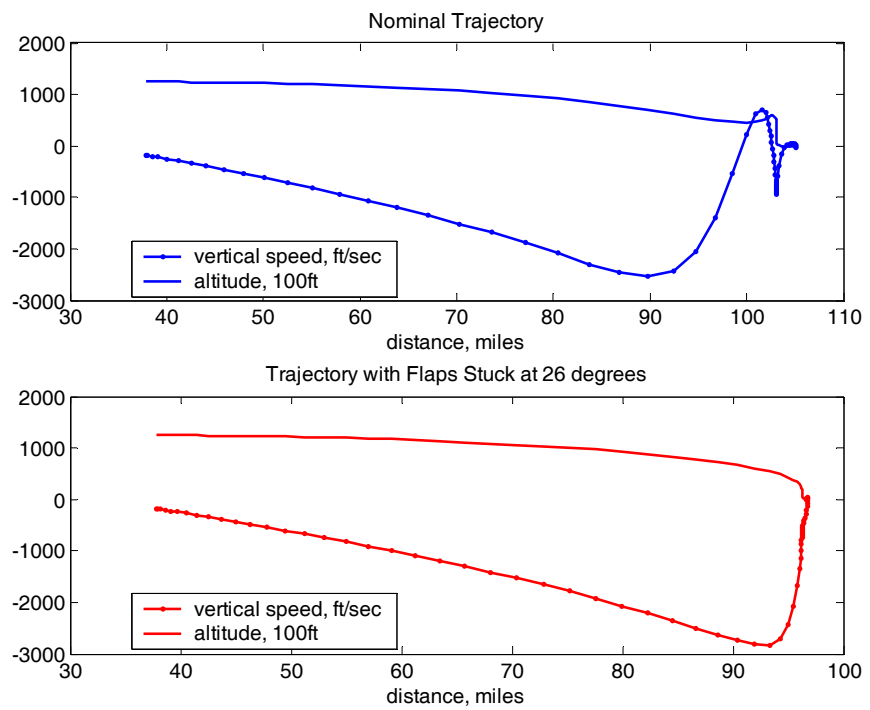


Figure 52 Vertical Speed Profiles (vs. Downrange Distance) for Minimum Downrange Trajectories

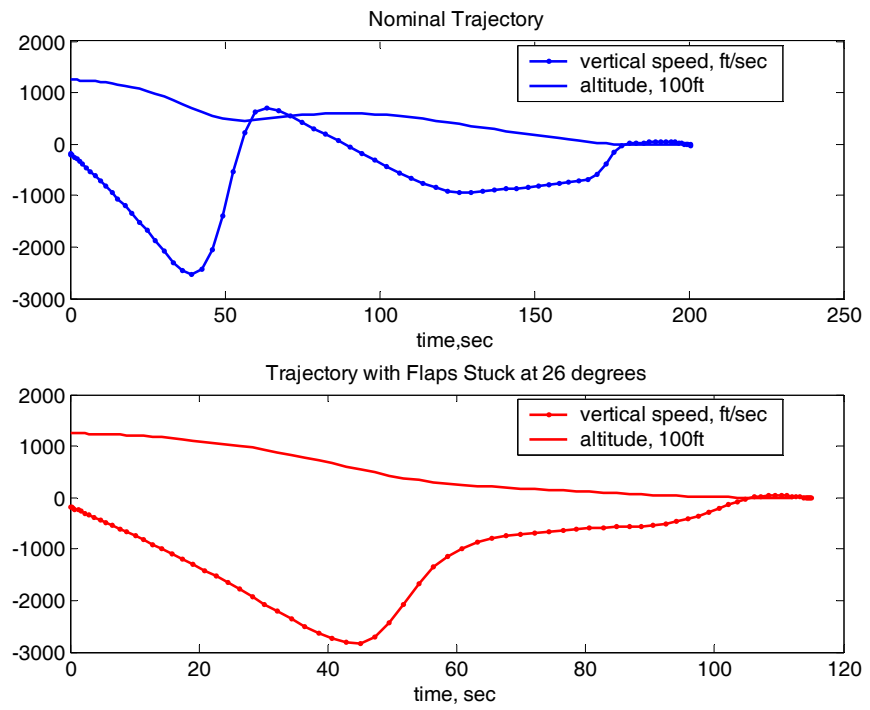


Figure 53 Vertical Speed Profiles (vs. time) for Nominal and Failed Trajectories,
Minimum Downrange

f. Body Frame Normal Force

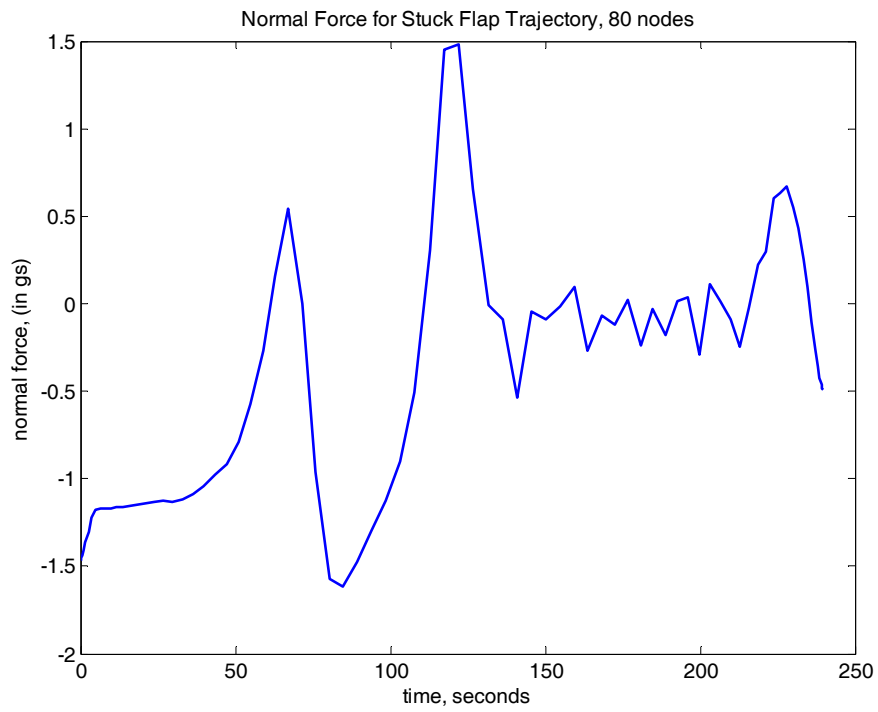


Figure 54 Body Frame Normal Force ($n_z - 1$), Stuck Flap Minimum Downrange Trajectory

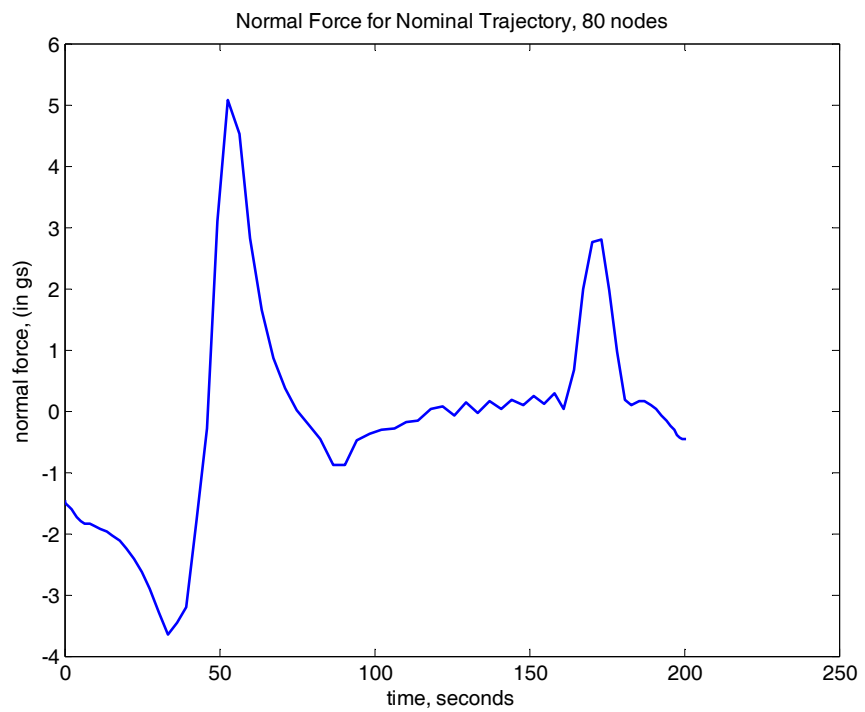


Figure 55 Body Frame Normal Force ($n_z - 1$), Nominal Minimum Downrange Trajectory

g. Controls

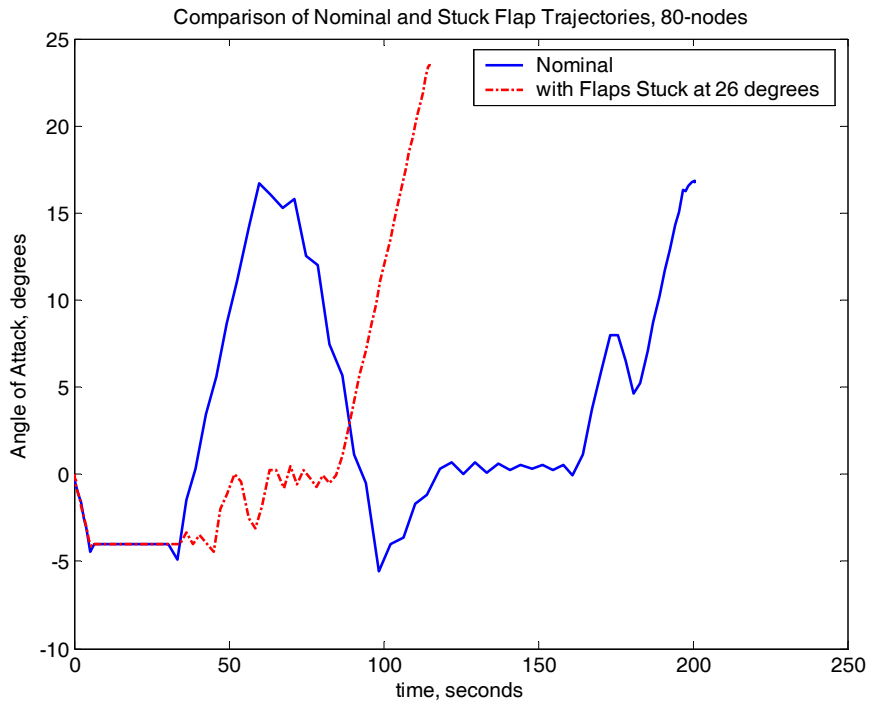


Figure 56 Angle of Attack Profile, Minimum Downrange Trajectories

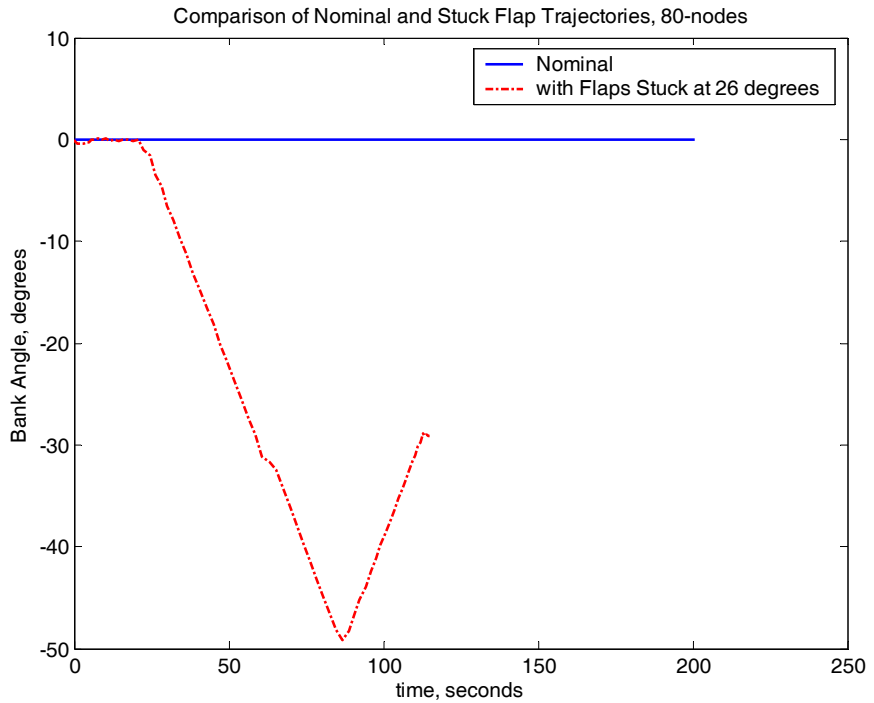


Figure 57 Bank Angle Profile, Minimum Downrange Trajectories

h. Pseudo Controls

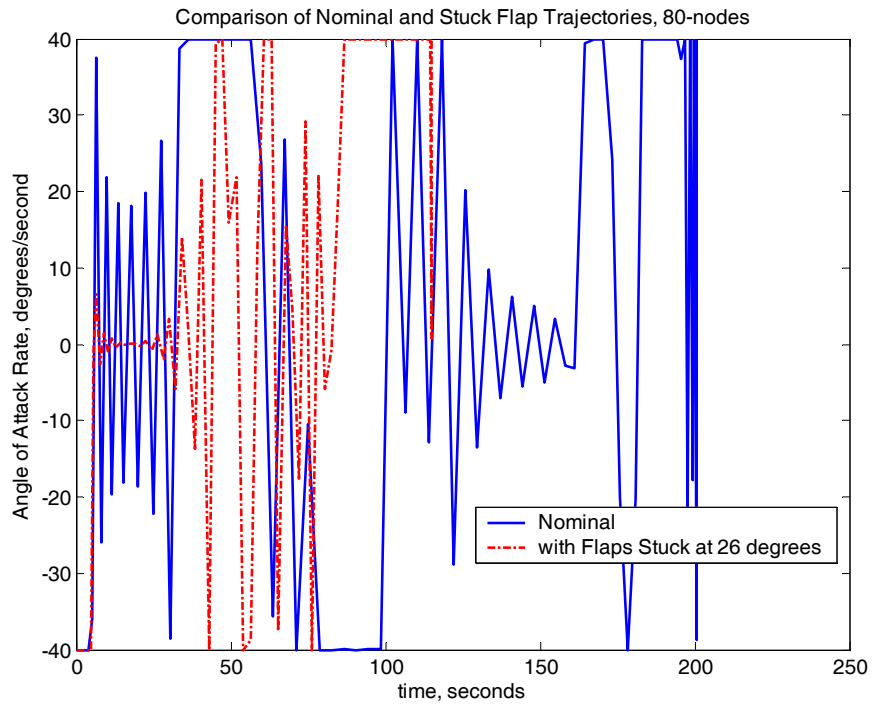


Figure 58 Angle of Attack Rate Profile, Minimum Downrange Trajectories

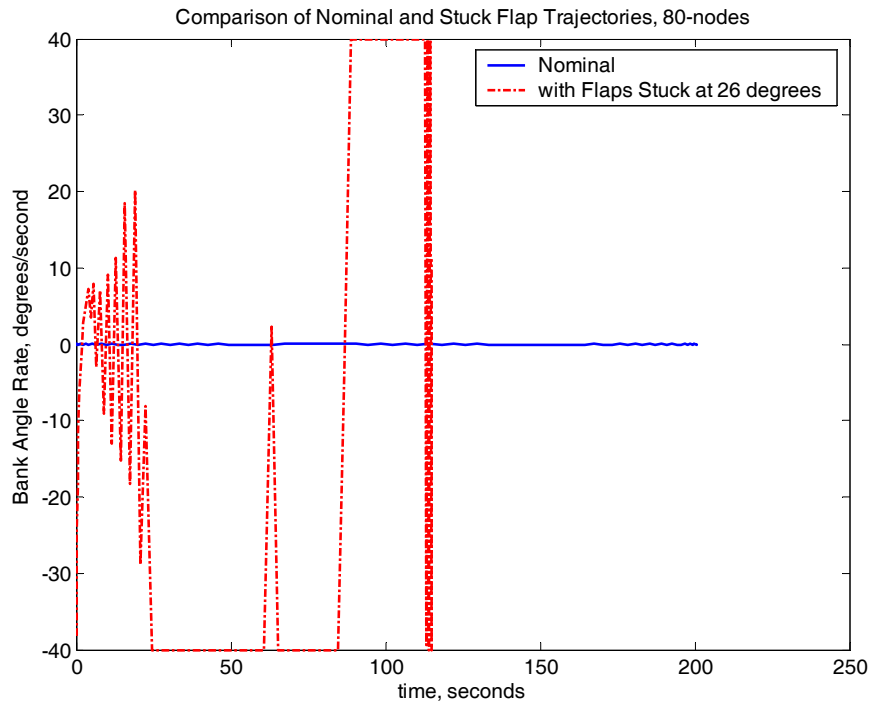


Figure 59 Bank Angle Profile, Minimum Downrange Trajectories

i. Trim Deficiency

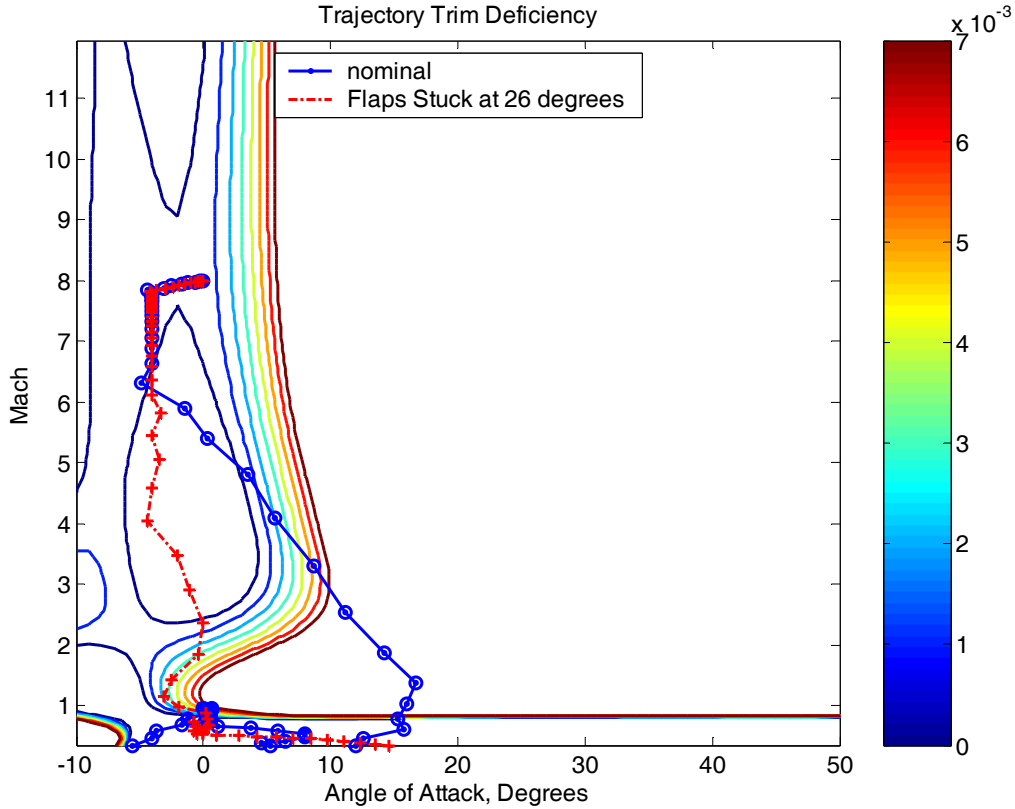


Figure 60 Trajectory Trim Deficiencies, Minimum Downrange Trajectories

The trim deficiency path constraint for the failed vehicle is not active until passing Mach 2 at which point the vehicle follows the path constraint until subsonic. The initial Mach-alpha profiles for both vehicles are nearly identical until Mach 6 at which point they diverge. The vehicles' Mach-altitude profiles begin to slightly diverge until Mach 4 at which point the nominal vehicle conducts a climb. While it appears to be some encroachment upon the trim deficiency path constraint for the failed trajectory between Mach 2 and Mach 1, all trim deficiency points corresponding to the trajectory's nodal points are within limits. The possible encroachment illustrates the need to have sufficient nodes not only for endpoint accuracy but also to adequately characterize the trajectory as related to trim deficiency. The solution can avoid encroachment by placing knots at the critical points where there is a large change in trim deficiency for small changes in either Mach number or angle of attack.

j. Optimality Analysis

The trajectories generated by DIDO were “near-optimal”. An examination of the Hamiltonians for both trajectories shows larger Hamiltonians than the expected zero, however, the *average* Hamiltonian for both trajectories is nearly zero. Both vehicles’ flight path angles reach the limiting value of ninety degrees. The duals for both FPAs meet the necessary conditions.

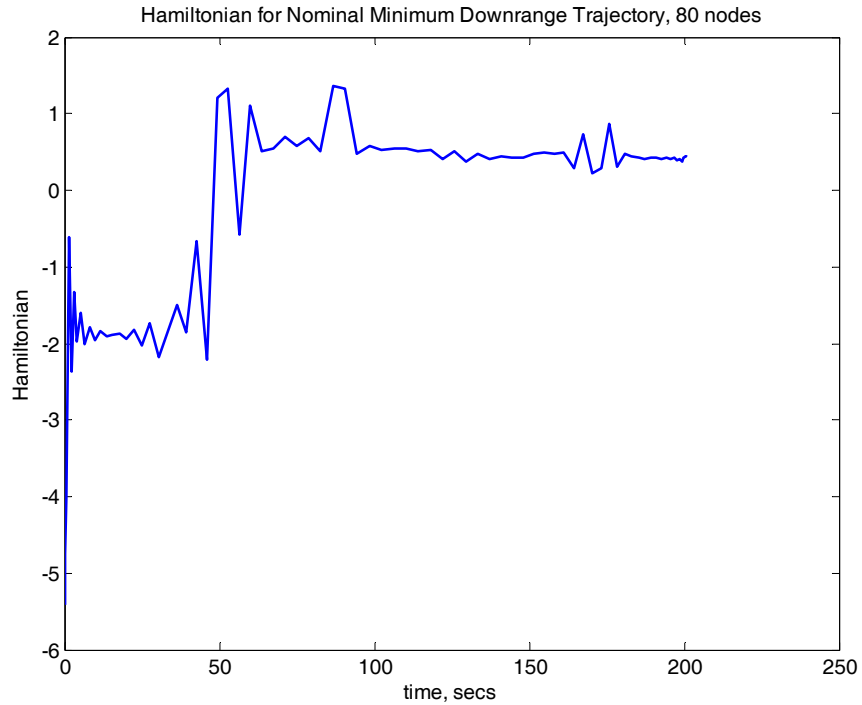


Figure 61 Hamiltonian for Nominal Minimum Downrange Trajectory

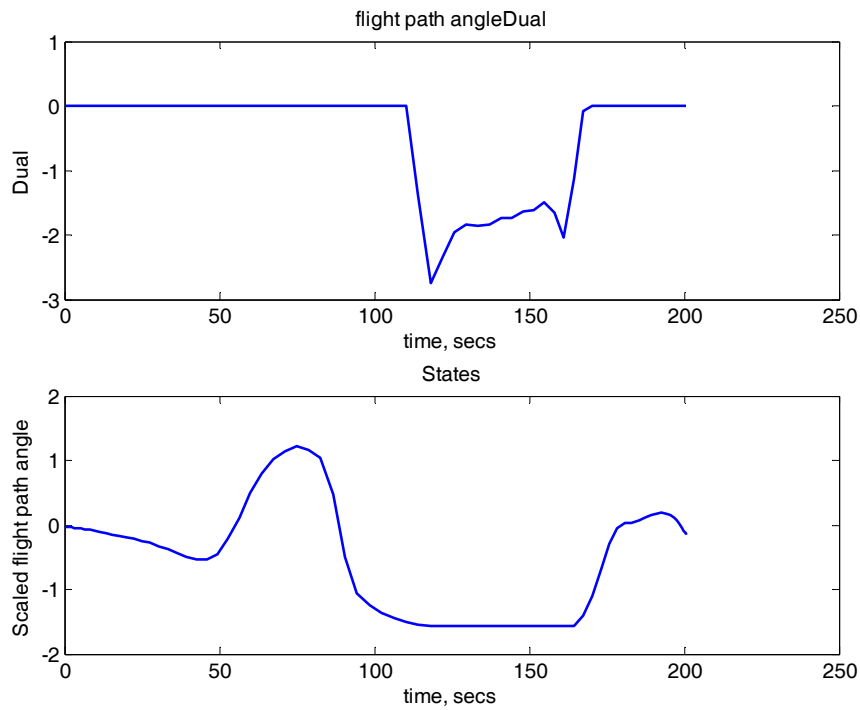


Figure 62 Constrained Flight Path Angle and Associated Dual, Nominal Minimum Downrange Trajectory

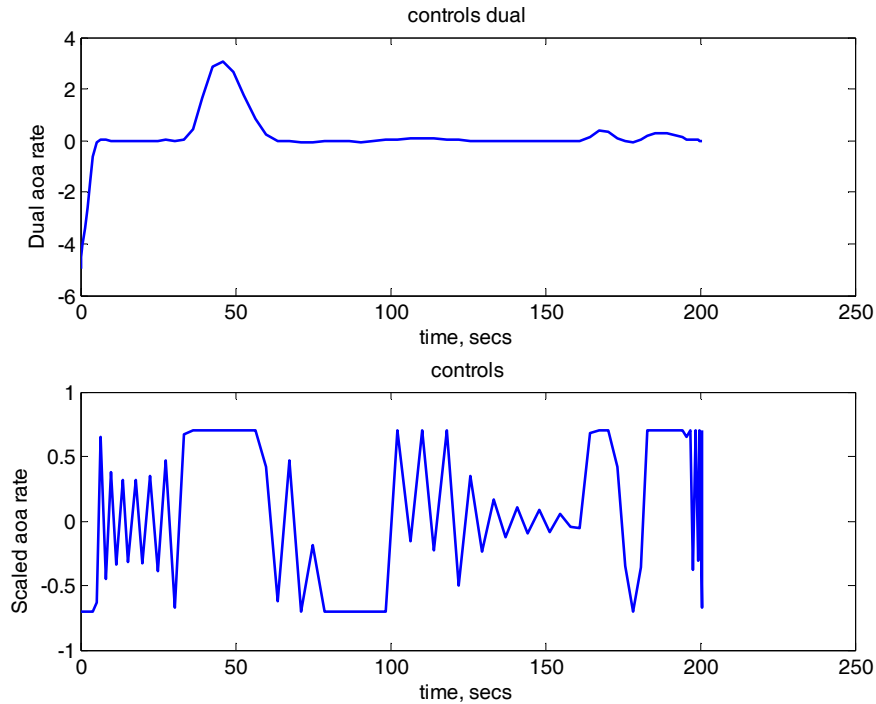


Figure 63 Constrained Angle of Attack Rate and Associated Dual, Nominal Minimum Downrange Trajectory

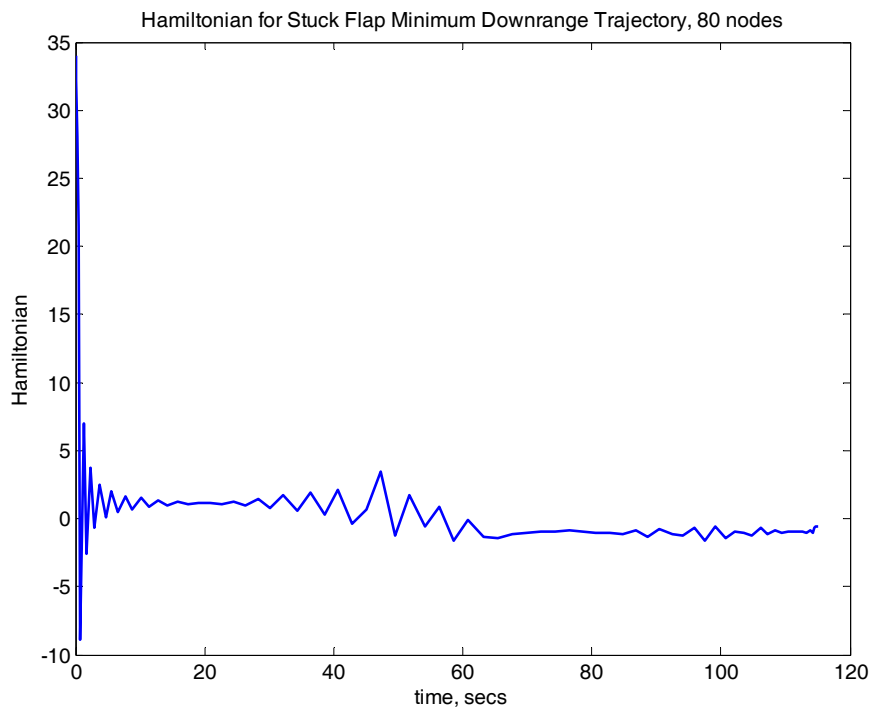


Figure 64 Hamiltonian for Stuck Flap, Minimum Downrange Trajectory

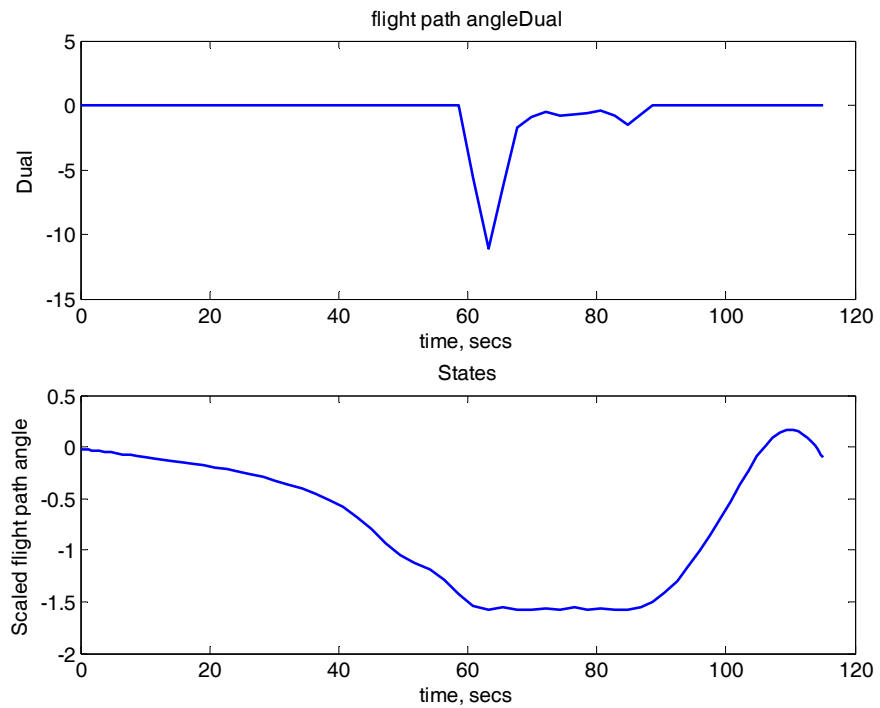


Figure 65 Constrained Flight Path Angle and Associated Dual, Stuck Flap Minimum Downrange Trajectory

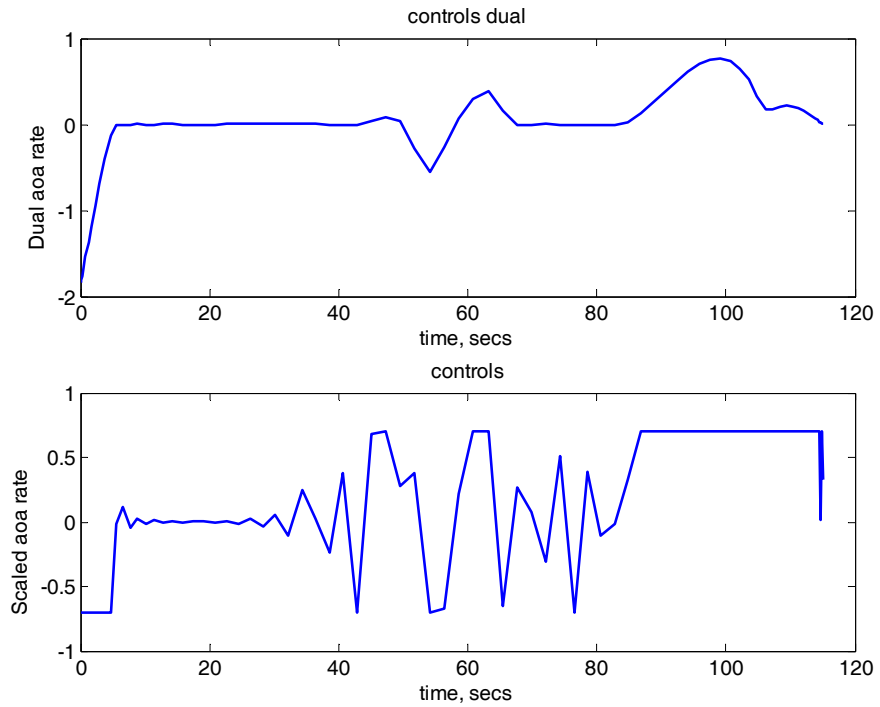


Figure 66 Constrained Angle of Attack Rate and Associated Dual, Stuck Flap Minimum Downrange Trajectory

k. Feasibility

Both nominal and stuck flap trajectories propagate with acceptable error with 80-node solutions. Propagation errors are identical to those for the failed, maximum downrange trajectory.

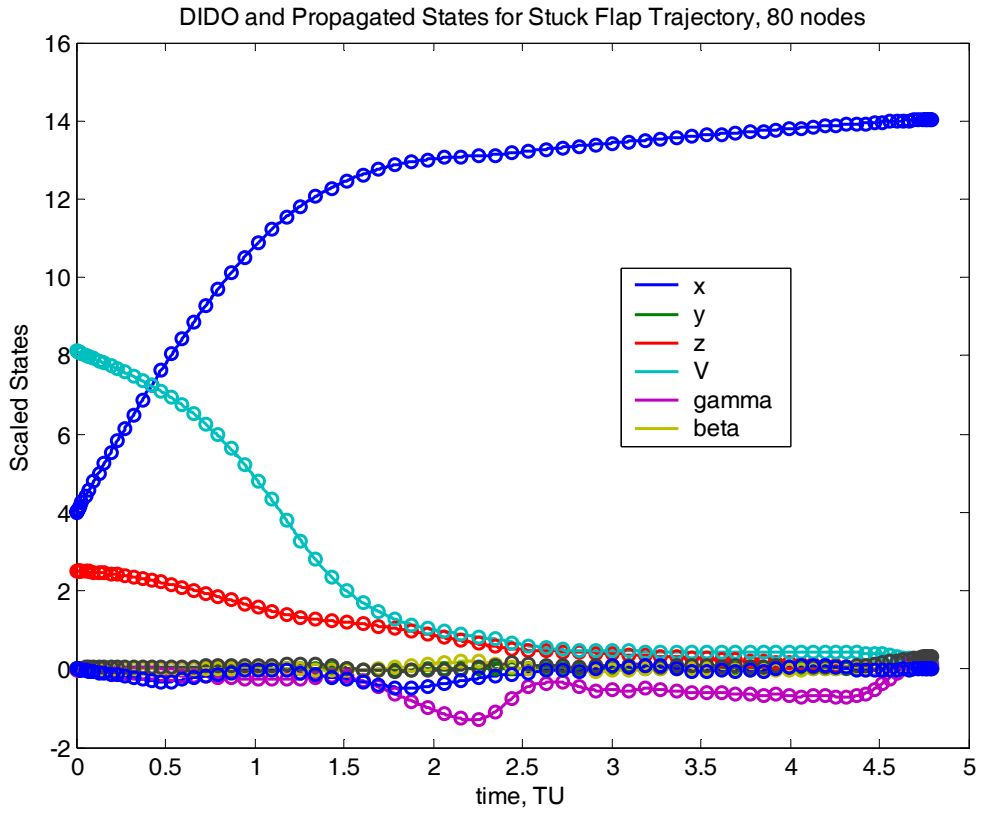


Figure 67 DIDO and Propagated Controls for Stuck Flap, Minimum Downrange Trajectory (DIDO controls are denoted by discrete points)

5. Minimum /Maximum Crossrange

The minimum and maximum crossrange profiles show symmetry and as such only the maximum crossrange will be shown as representative trajectories.

a. *Mach-Altitude Profile*

The Mach-altitude profile is similar to those shown for the maximum downrange case. The vehicle trades airspeed for altitude as it seeks to maximize the cross range.

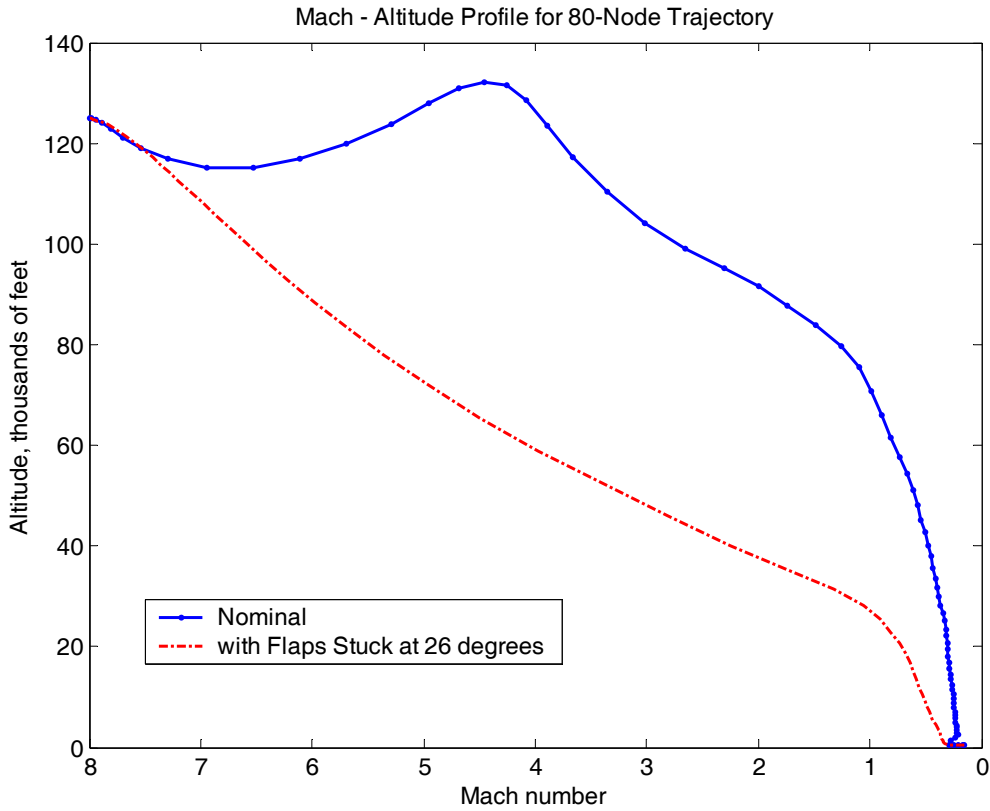


Figure 68 Downrange Distance Profiles for Maximum Crossrange Trajectories

b. Trajectory in Cartesian Coordinates

An interesting result of Figure 69 is that the nominal vehicle reaches the maximum downrange in the first fifth of its flight time. This corresponds to an azimuth of 90 degrees at the 300 second point. This failed vehicle initiates its turn at the same time as the nominal vehicle but is able to reach 90 degrees azimuth (with some trouble) much earlier because of the energy bleed caused by the additional drag of the stuck flaps.

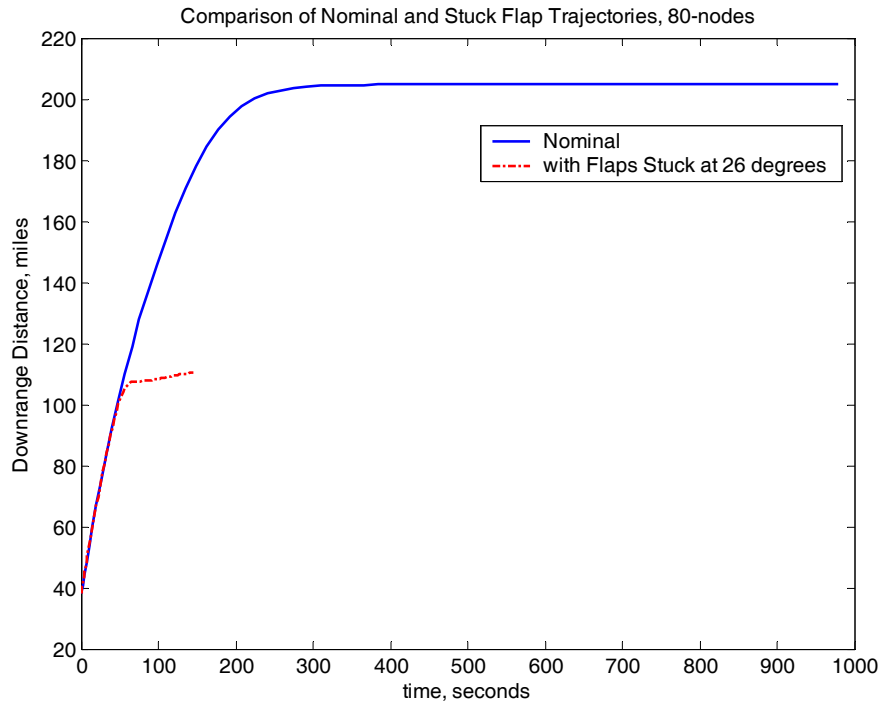


Figure 69 Downrange Distance Profile for Maximum Crossrange Trajectories

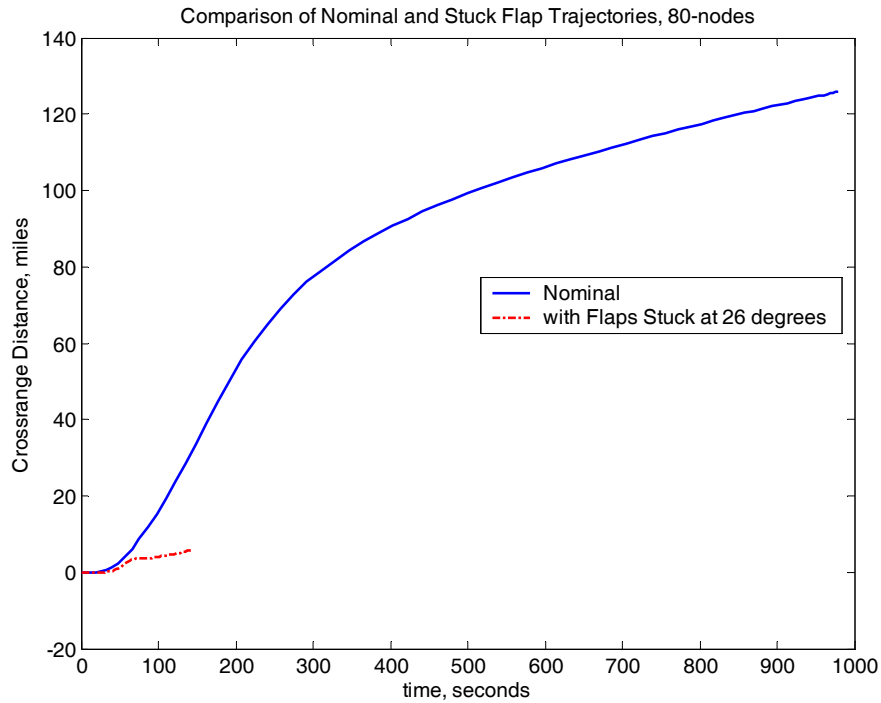


Figure 70 Crossrange Distance Profile for Maximum Crossrange Trajectories

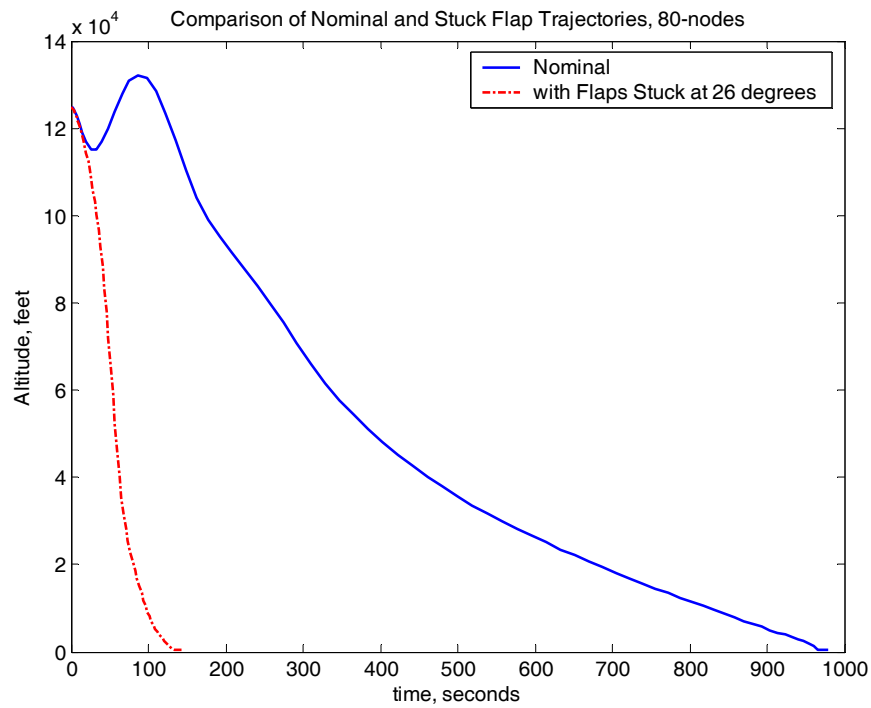


Figure 71 Altitude Profile for Maximum Crossrange Trajectories

c. Velocity Profile

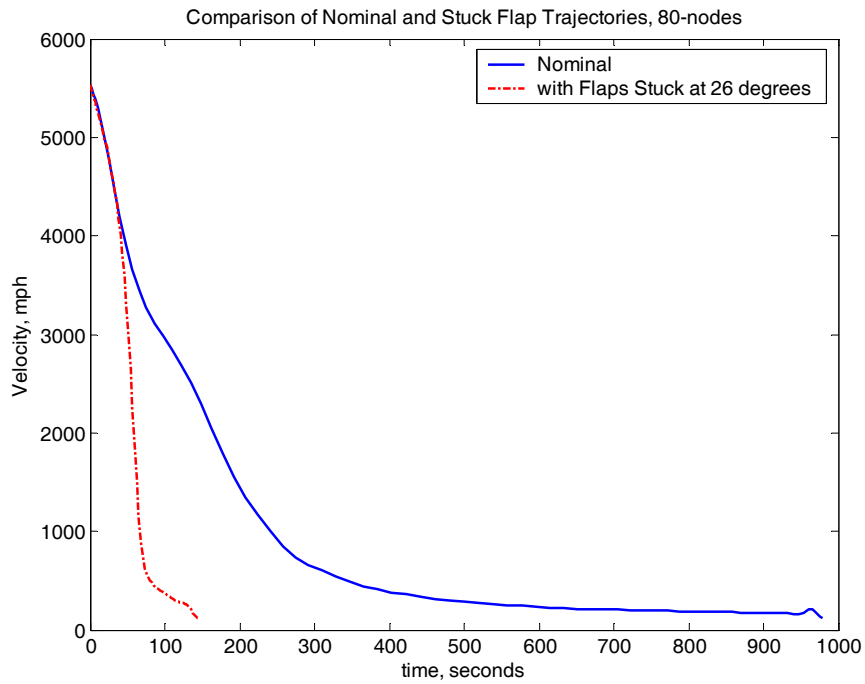


Figure 72 Velocity Profile for Maximum Crossrange Trajectories

d. Flight Path and Azimuth Angles

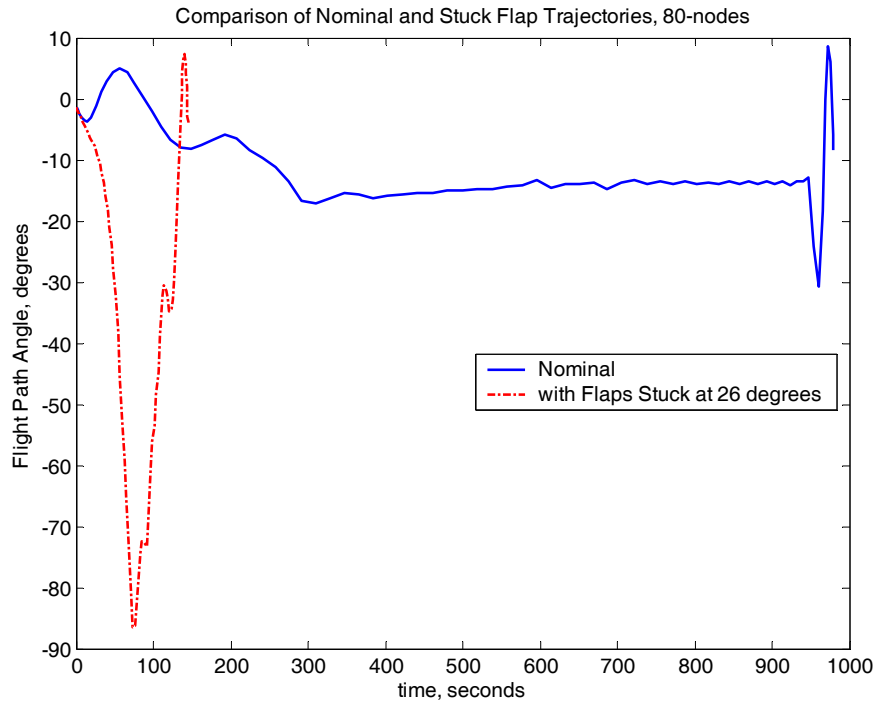


Figure 73 Flight Path Angle Profile for Maximum Crossrange Trajectories

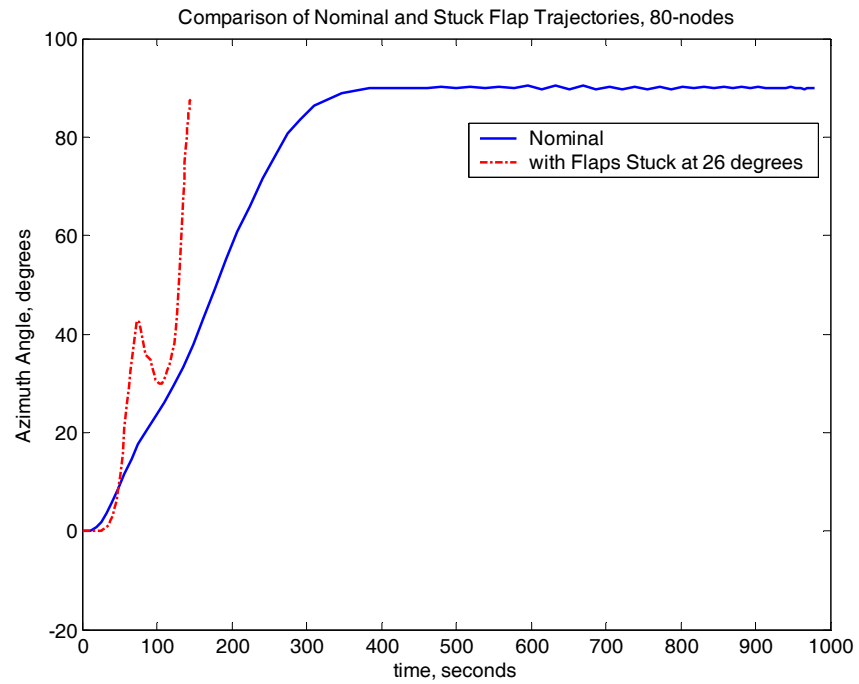


Figure 74 Azimuth Angle Profile for Maximum Crossrange Trajectories

e. *Vertical Speed Profiles*

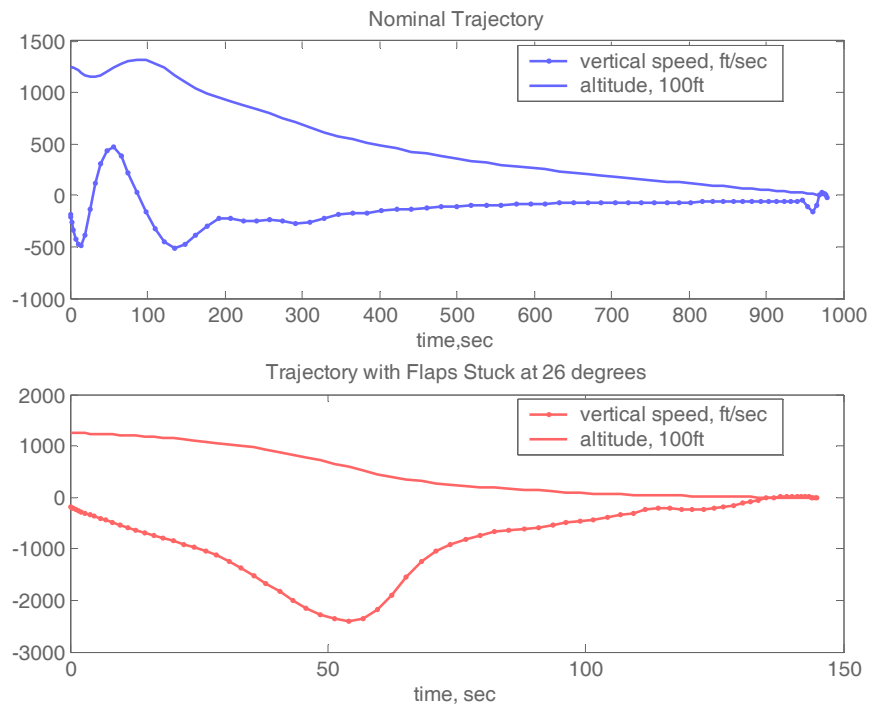


Figure 75 Vertical Speed Profiles for Maximum Crossrange Trajectories

f. Normal Force Profiles

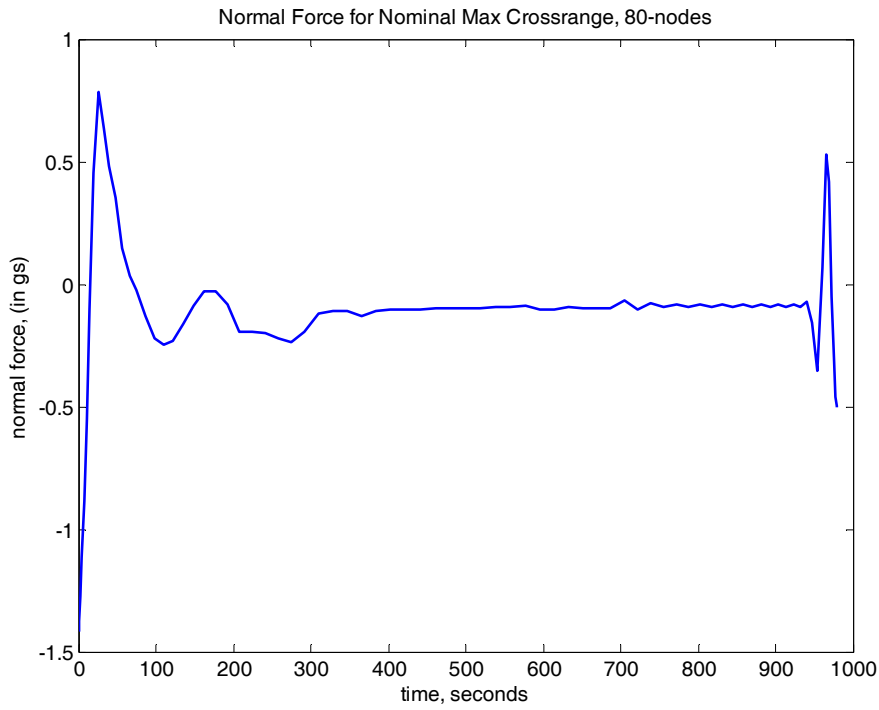


Figure 76 Normal Force ($n_z - 1$) for Nominal Maximum Crossrange Trajectory

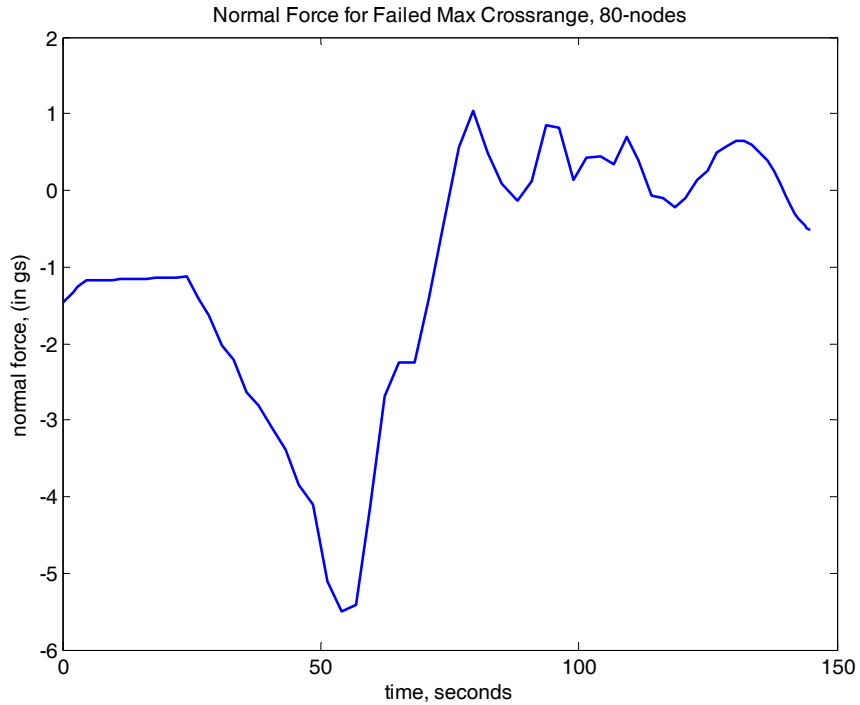


Figure 77 Normal Force($n_z - 1$) for Stuck Flap, Maximum Crossrange Trajectory

g. Controls

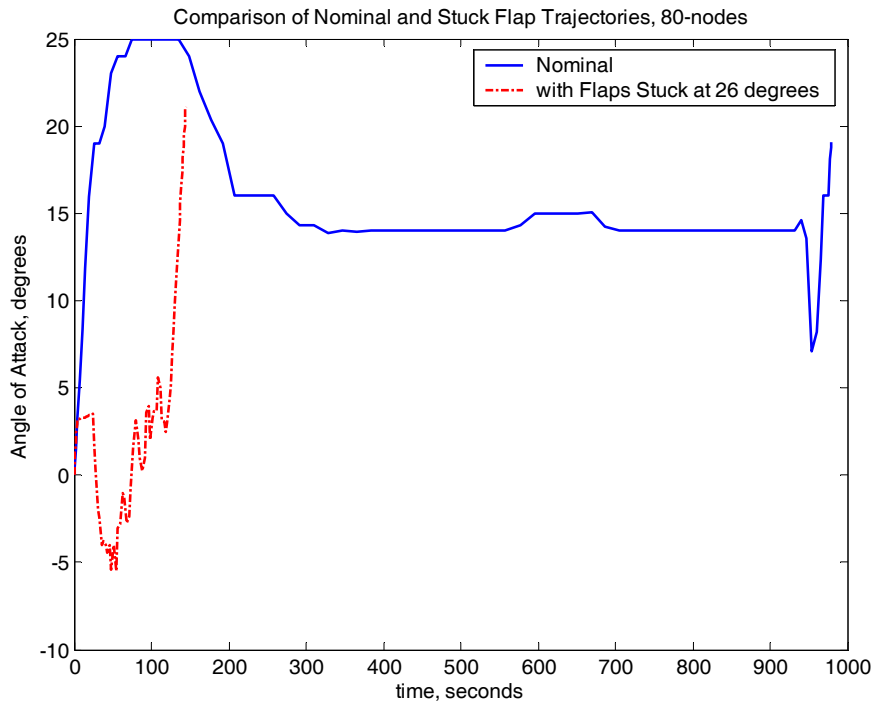


Figure 78 Angle of Attack Profile for Maximum Crossrange Trajectories

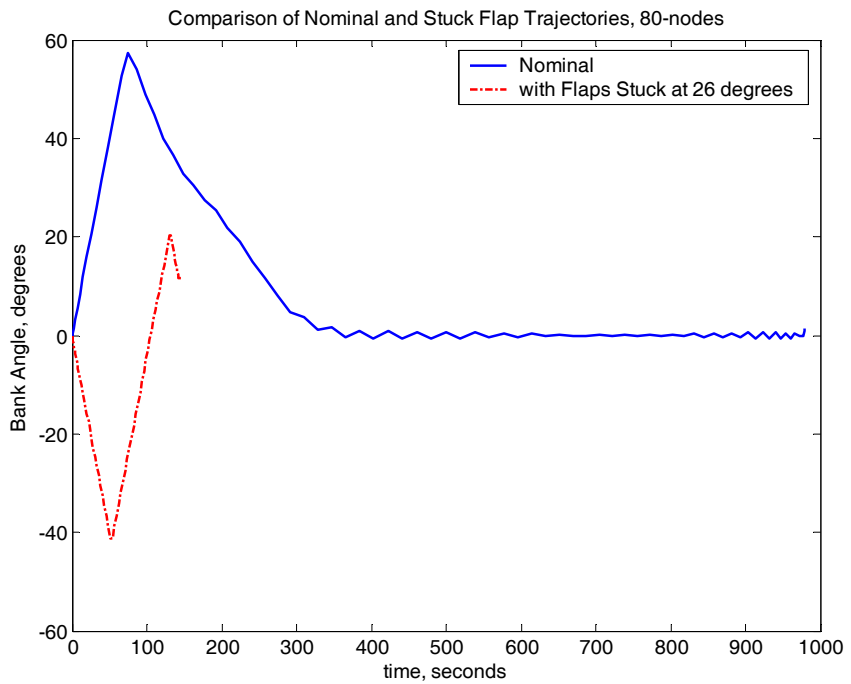


Figure 79 Bank Angle Profile for Maximum Crossrange Trajectories

h. Pseudo Controls

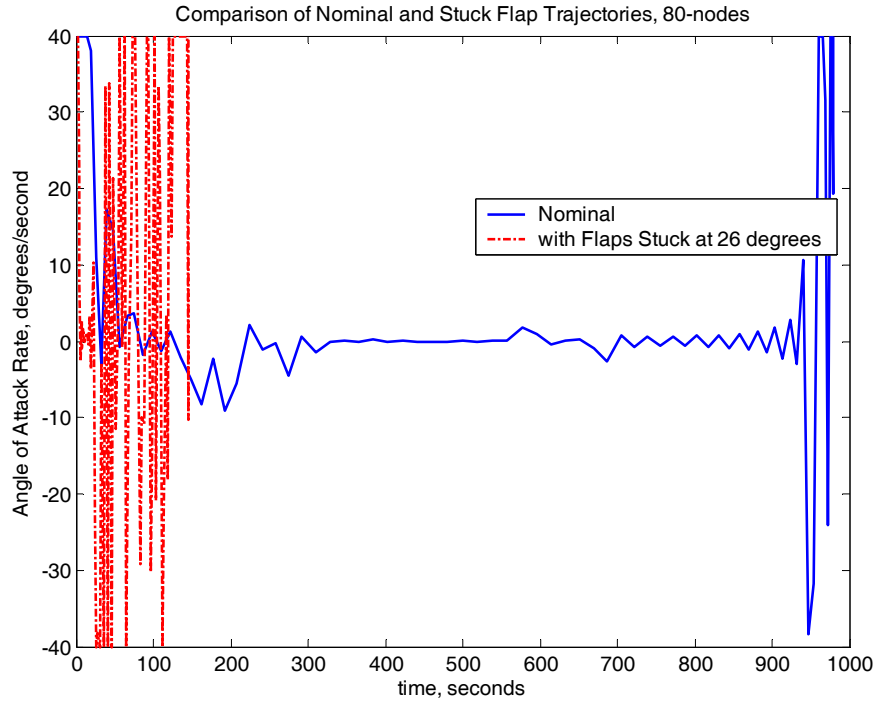


Figure 80 Angle of Attack Rate Profile for Maximum Crossrange Trajectories

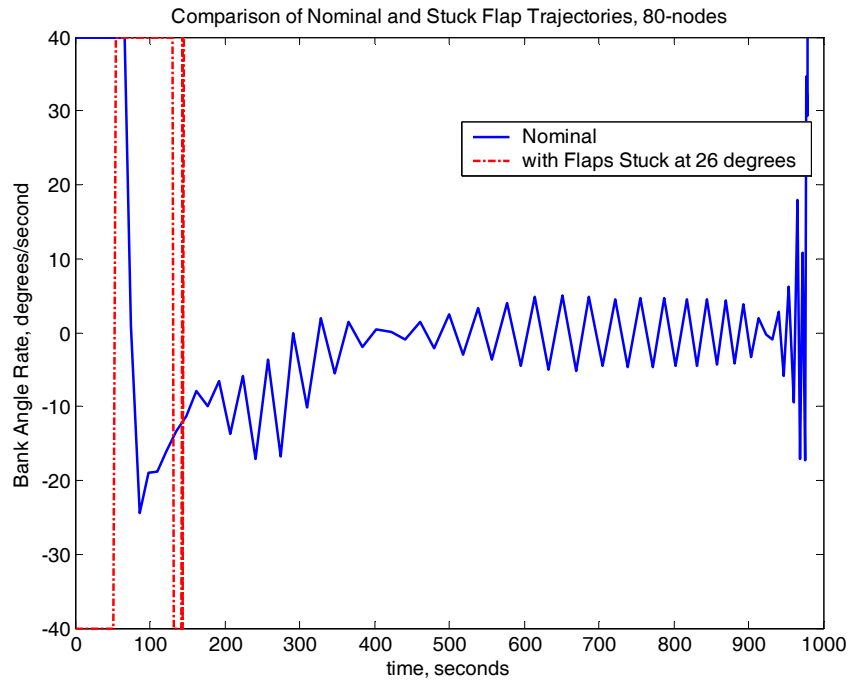


Figure 81 Bank Angle Rate Profiles for Maximum Crossrange Trajectories

i. Trim Deficiency

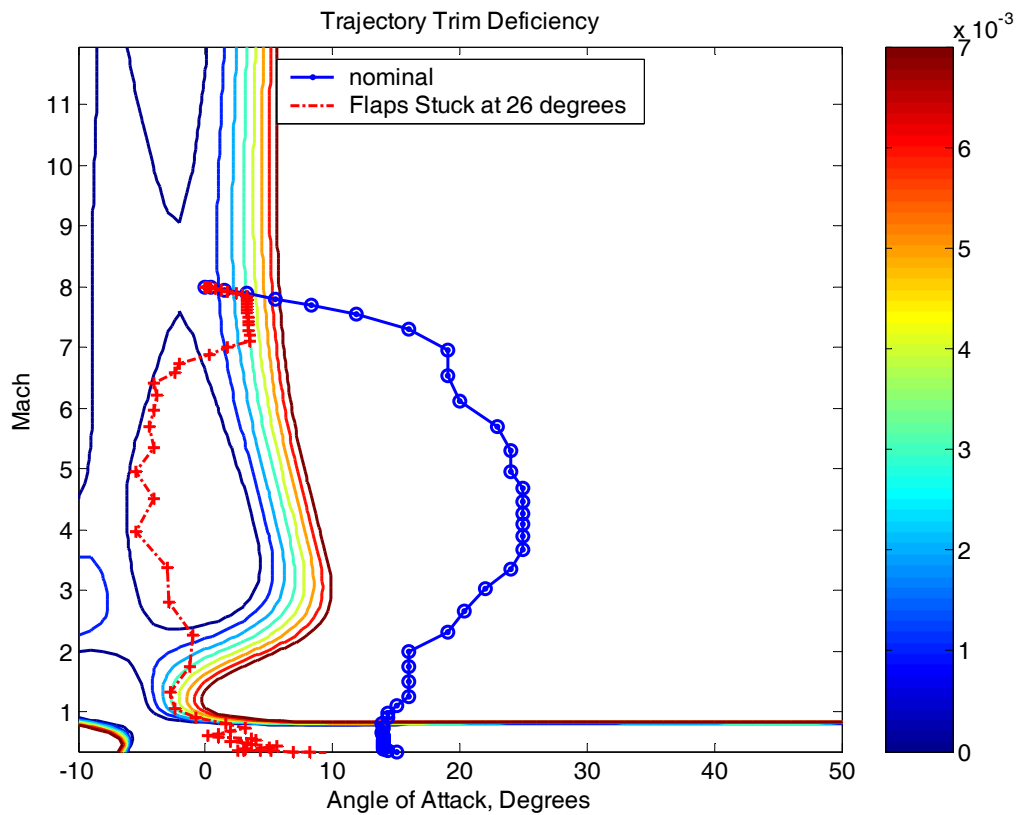


Figure 82 Trim Deficiencies for Maximum Crossrange Trajectories

j. Optimality Analysis

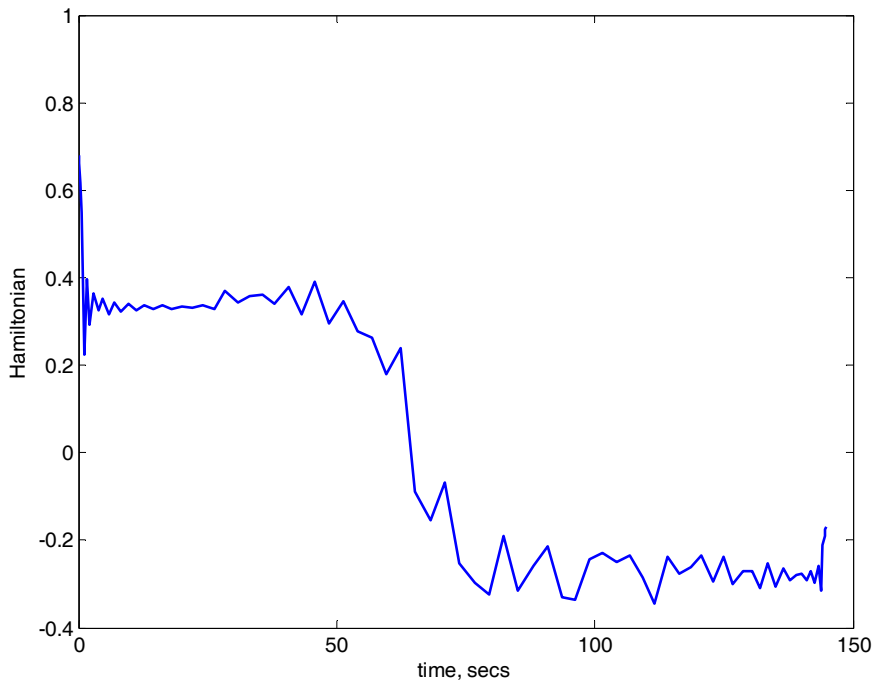


Figure 83 Hamiltonian for Stuck Flap, Maximum Crossrange Trajectory

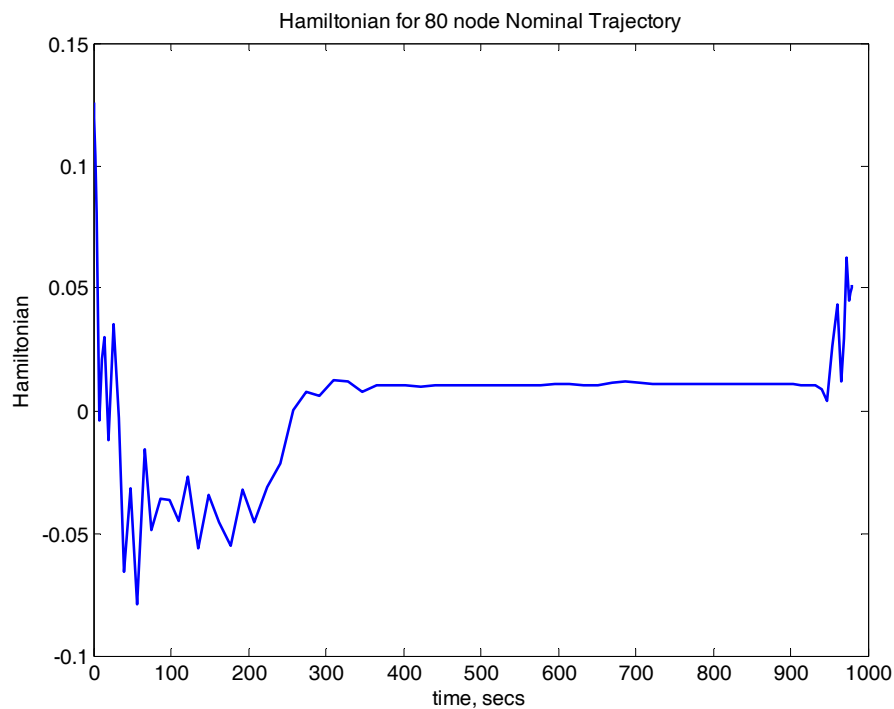


Figure 84 Hamiltonian for Nominal Maximum Crossrange Trajectory

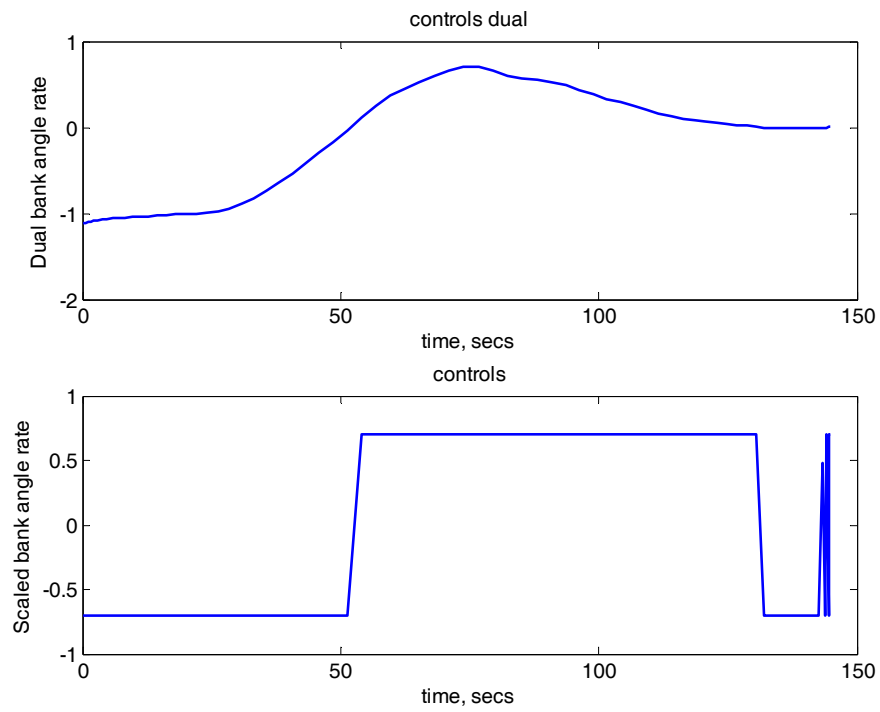


Figure 85 Bank Angle Rate and Dual for Stuck Flap Max Crossrange Trajectory

k. Feasibility

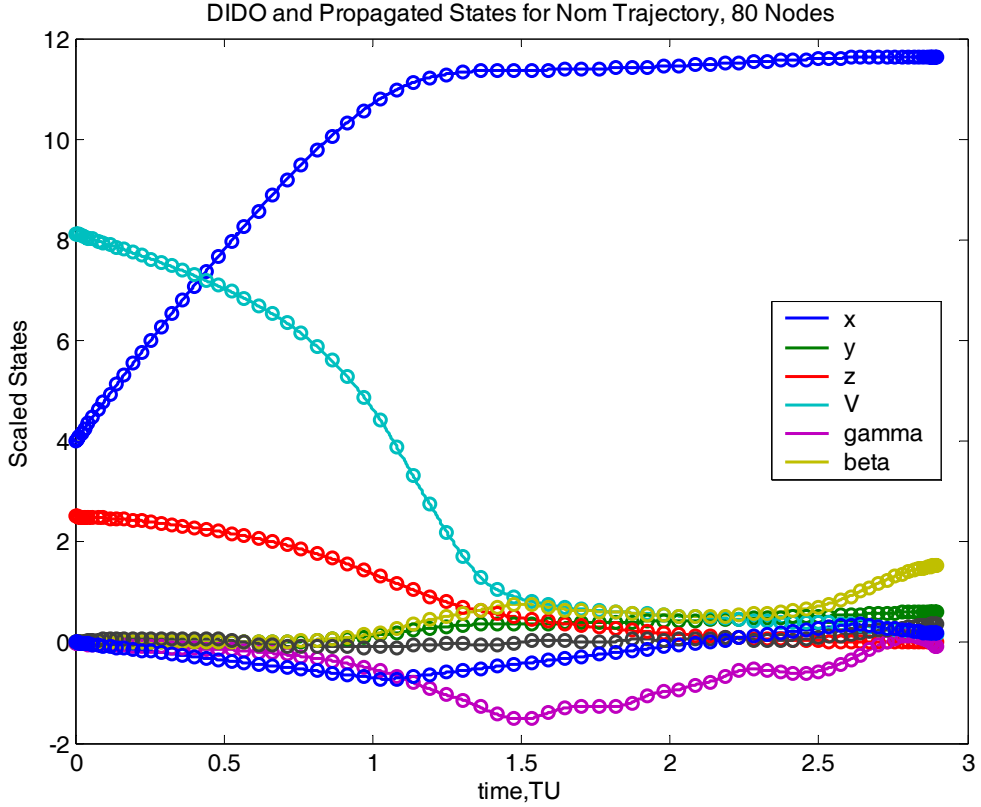


Figure 86 DIDO and Propagated Controls for Stuck Flap Max Crossrange Trajectory (DIDO controls are denoted by discrete points)

The error between the DIDO states and propagated states for the vehicle with stuck flaps is shown below.

$$\text{error} = \begin{bmatrix} 37 \text{ ft} & -85 \text{ ft} & -7 \text{ ft} & -0.11 \text{ ft/sec} & -7 \text{ deg} & 9 \text{ deg} & -0.01 \text{ deg/sec} & -0.01 \text{ deg/sec} \end{bmatrix}^T$$

C. TRAJECTORY TO A SPECIFIED FIELD

1. Endpoint Conditions and Cost Function

The endpoint set for a trajectory to a specified field within the footprint contains the field Cartesian coordinates as well as the azimuth of the landing runway. Both nominal and failed vehicles were able to land at specified fields within their respective footprints however the choice of runway azimuths was limited to an approximate range

of +/- 100 degrees. For example, landing at a runway within the failed footprint with a runway heading of -90 degrees was accomplished relatively rapidly with a resultant “locally optimal solution found”. The same field with a runway heading of -100 degrees gave a “near optimal” solution while a field with a runway heading of -120 degrees gave infeasible or suboptimal results for the same 80-node run. It should be noted that while the infeasibility was for an 80-node trajectory, larger node trajectories have been shown to provide near optimal or locally optimal solutions when bootstrapped from lower-node infeasible trajectories. There is the additional computation time penalty that comes along with computing trajectories with larger nodes.

The cost function for these trajectories to specified field was a Lagrangian cost function that minimized the angles of attack and bank. The rationale behind a cost function such as this is that depending on the control system failure, excessive movement of control surface hydraulic actuators may deplete the hydraulic working fluid of that particular loop resulting in cascading failures.

The full problem formulation is shown below:

$$\min_u J(\underline{x}(t), \underline{u}(t), t_0, t_f) = \int_{t_0}^{t_f} (\alpha(t) + \phi(t)) dt$$

subject to $\dot{\underline{x}} = \underline{f}(\underline{x}, \underline{u}, \tau)$

$$\underline{h}_l \leq \underline{h}(\underline{x}, \underline{u}, t) \leq \underline{h}_u$$

$$\underline{e}_l \leq \underline{e}(\underline{x}(\tau_0), \underline{x}(\tau_f), \tau_0, \tau_f) \leq \underline{e}_u$$

$$\underline{x}_l \leq \underline{x}(\tau) \leq \underline{x}_u$$

$$\underline{u}_l \leq \underline{u}(\tau) \leq \underline{u}_u$$

Where

$$\underline{e}(x_f, \dot{x}_f, t_f) = [x_f \ y_f \ z_f \ \dot{z}_f \ V_f \ \beta_f \ \phi_f]^T$$

$$\underline{e}(x_f, \dot{x}_f, t_f) = [110 \text{ miles} \ -1 \text{ mile} \ 500 \text{ feet} \ -500 \pm 1000 \text{ ft/min} \ \text{Mach } 0.15 \pm 2\% \ -100^\circ \ 0 \pm 10^\circ]^T$$

All other initial conditions and path, state and control vectors and limits are identical to the previous formulations.

2. Profiles for a Failure-Mode Trajectory to a Specified Field

a. *Mach-Altitude Profile*

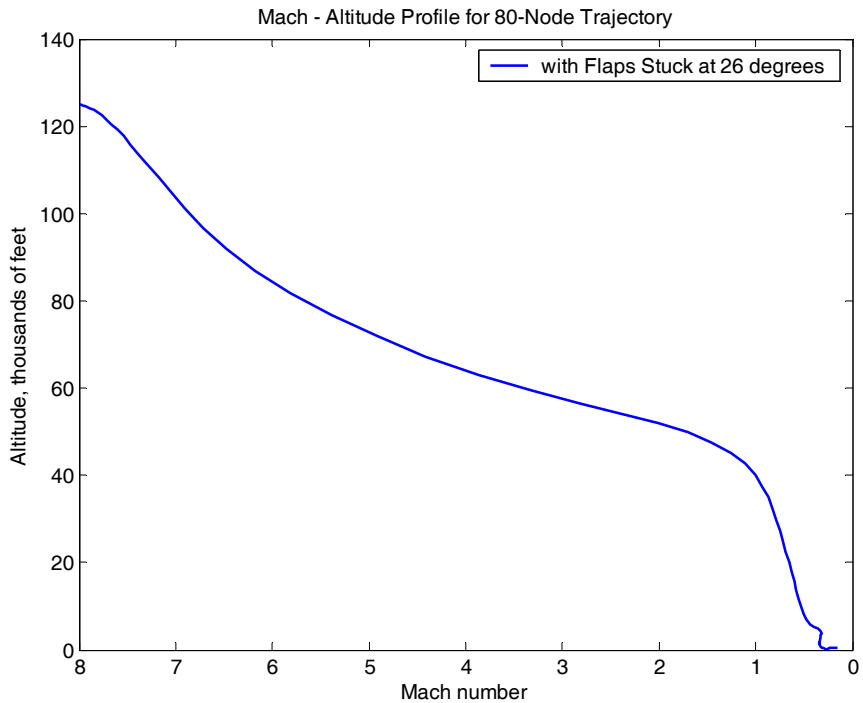


Figure 87 Mach-altitude Profile for Stuck Flap Trajectory to Specified Field

b. Trajectory in Cartesian Coordinates

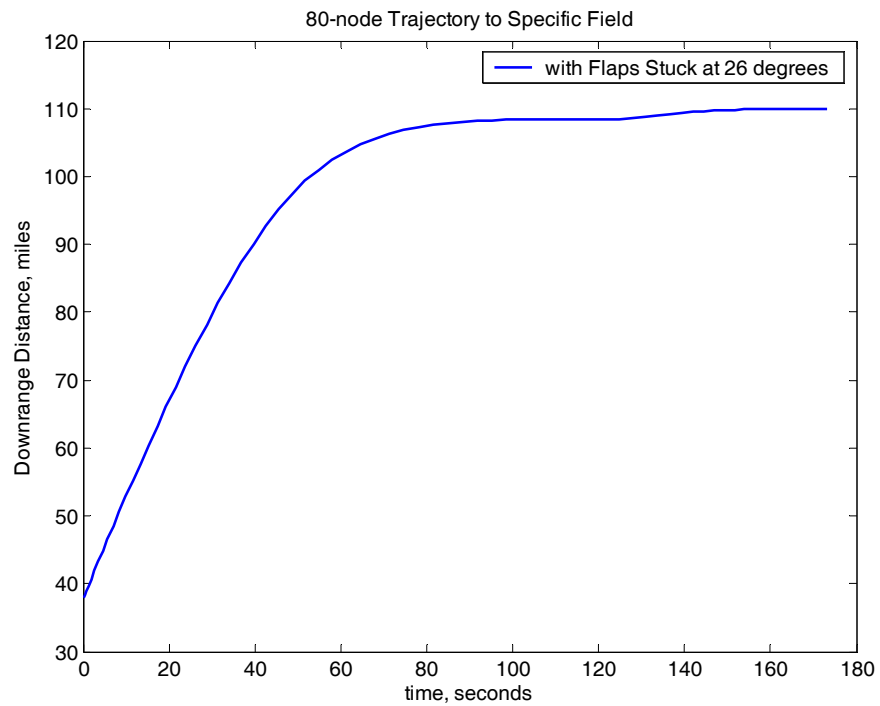


Figure 88 Downrange Profile for Stuck Flap Trajectory to Specified Field (Flaps Stuck at 26 degrees)

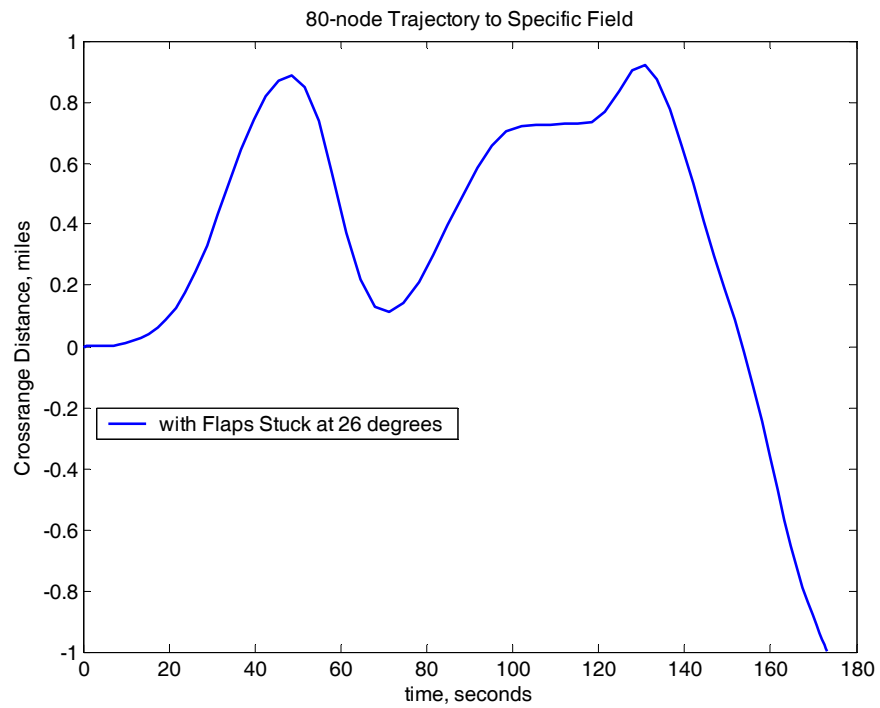


Figure 89 Crossrange Profile for Stuck Flap Trajectory to Specified Field (Flaps Stuck at 26 degrees)

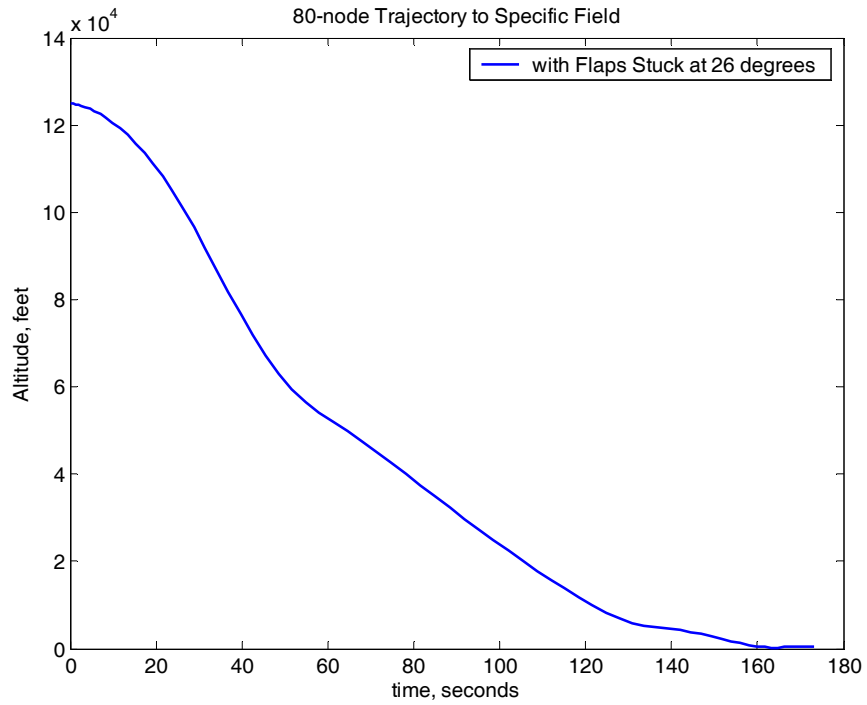


Figure 90 Altitude Profile for Stuck Flap Trajectory to Specified Field

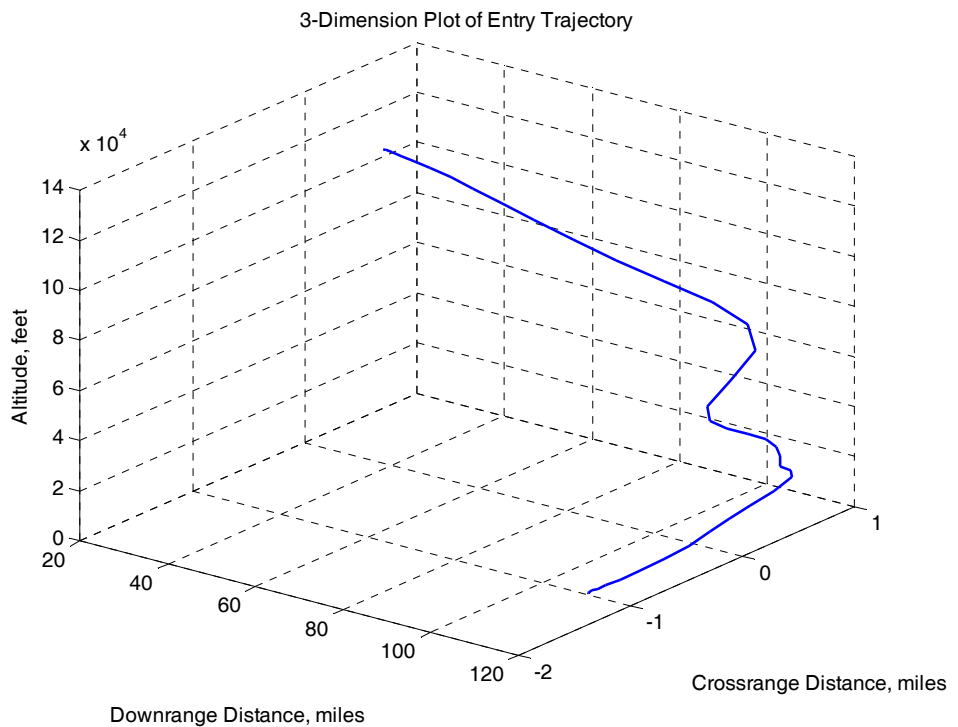


Figure 91 Three Dimensional Trajectory Depiction (not to scale) for Failed Vehicle
(Flaps Stuck at 26 degrees)

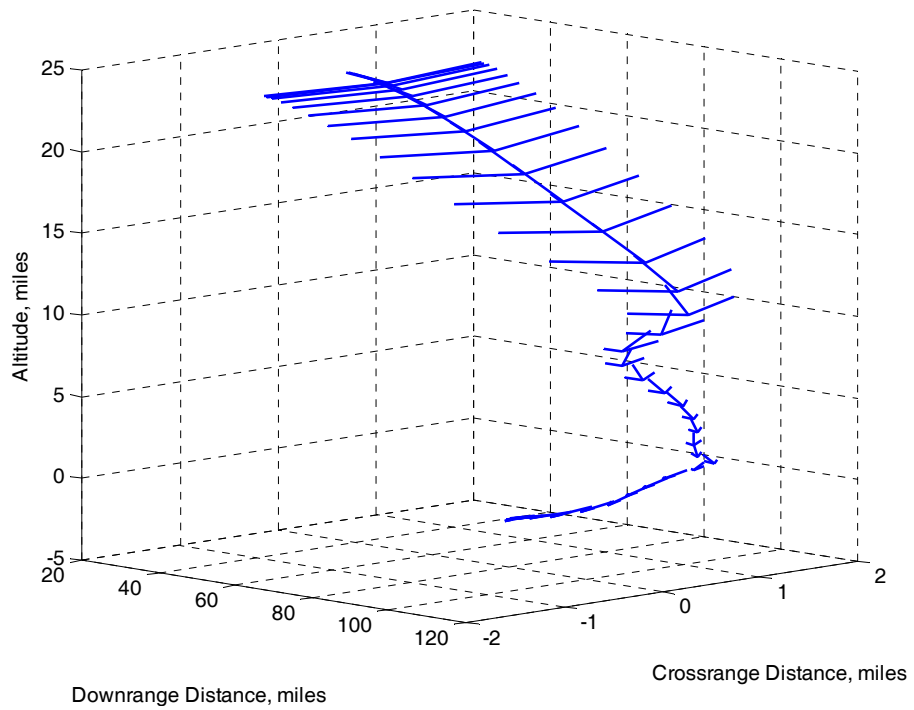


Figure 92 Quiver Plot (not to scale) for Failed Vehicle Trajectory to Specified Field
(Flaps Stuck at 26 degrees)

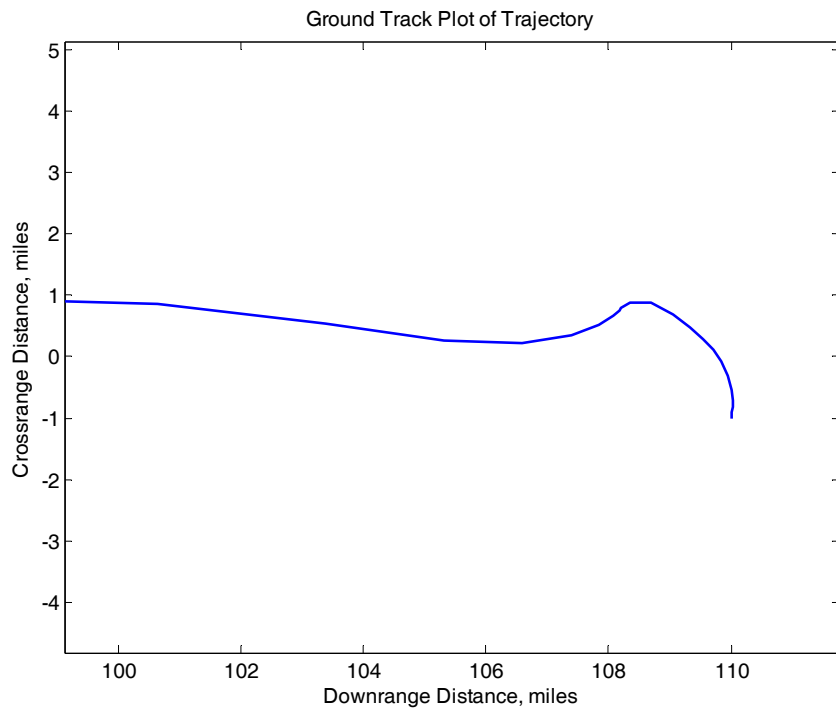


Figure 93 Ground Track Plot (not to scale) of Failed Vehicle Trajectory to Specified Field (Flaps Stuck at 26 degrees)

c. Velocity Profile

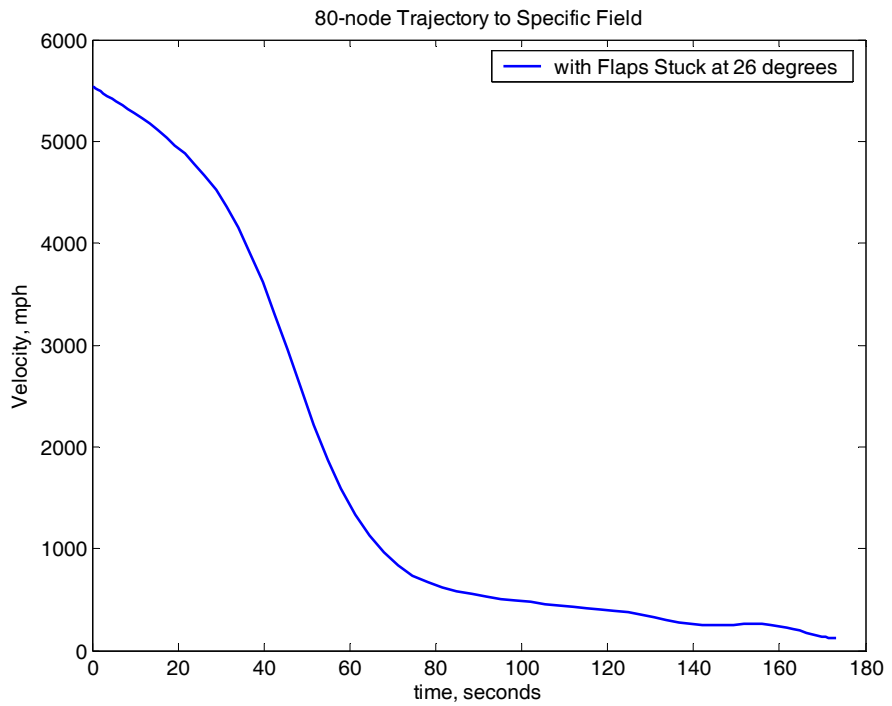


Figure 94 Velocity Profile for Failed Vehicle Trajectory to Specified Field

d. Flight Path and Azimuth Angle

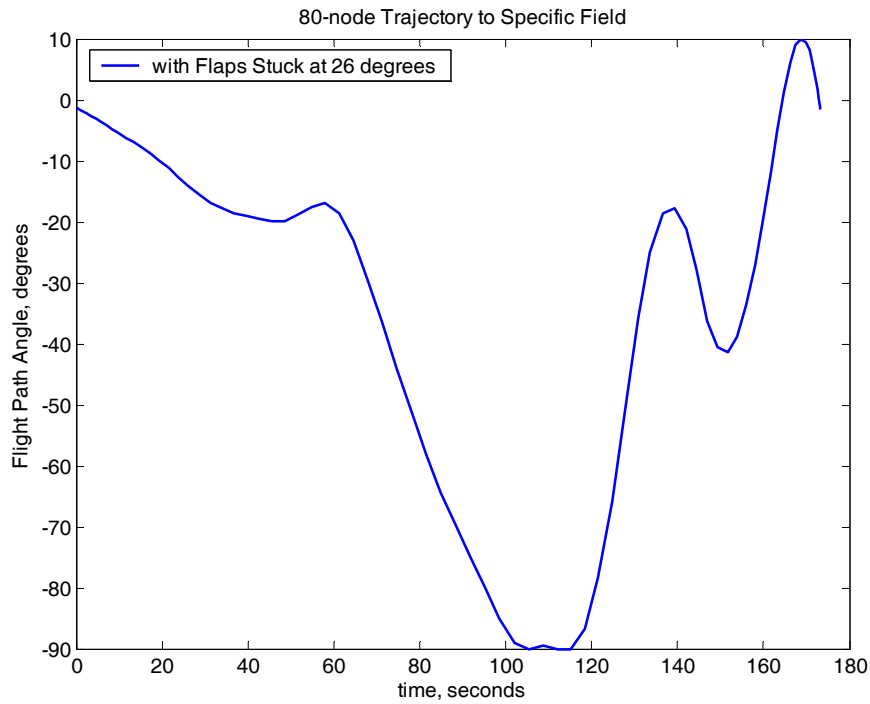


Figure 95 Flight Path Angle Profile for Failed Vehicle Trajectory to a Specified Field

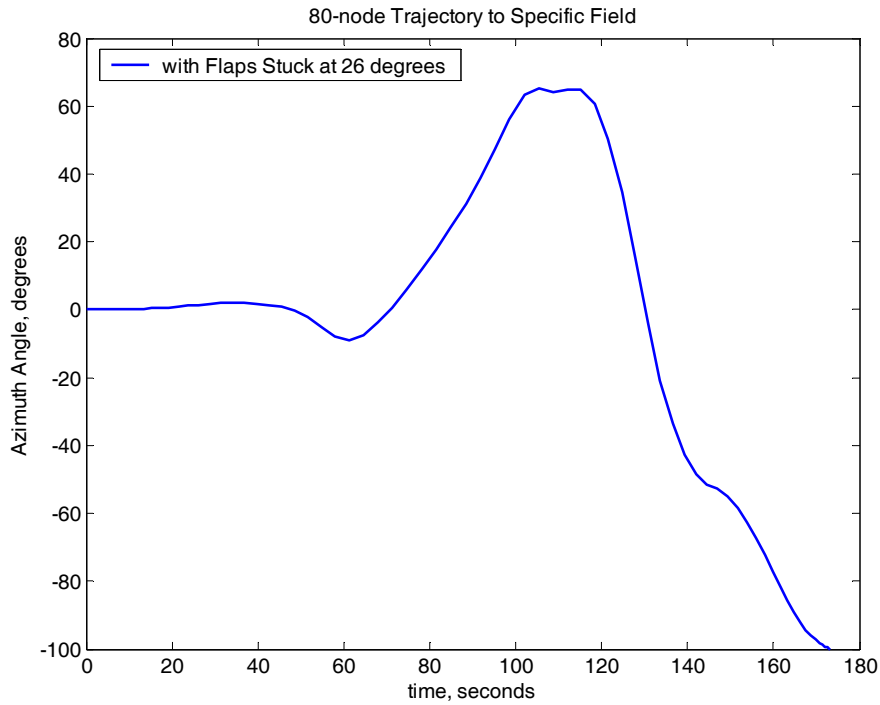


Figure 96 Azimuth Angle Profile for Failed Vehicle Trajectory to a Specified Field

e. **Body Frame Normal Force**

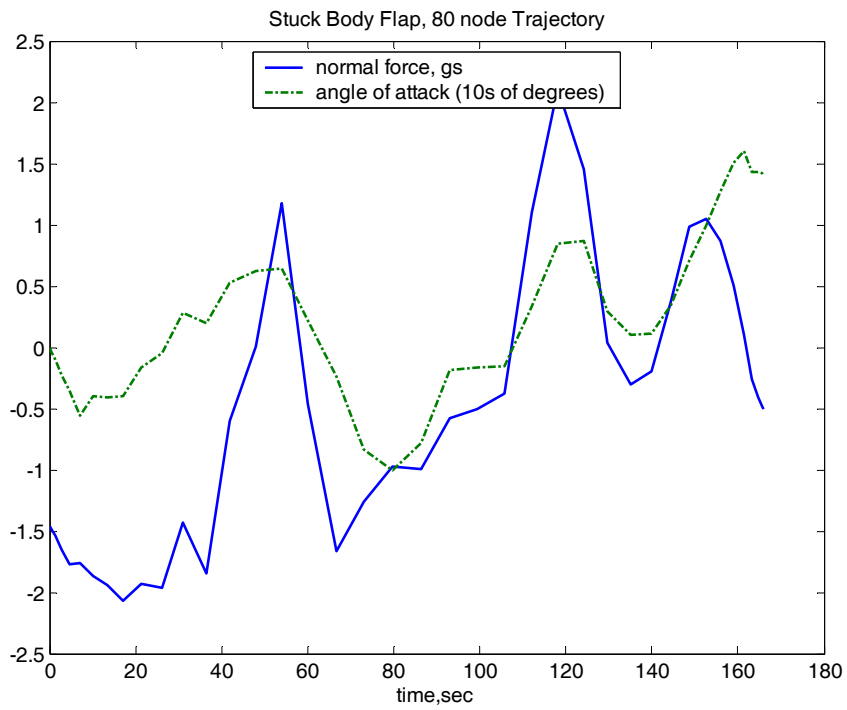


Figure 97 Normal Force($n_z - 1$) and Angle of Attack Profile for Failed Vehicle Trajectory to Specified Field



Figure 98 Normal Force($n_z - 1$) and Angle of Bank Profile for Failed Vehicle Trajectory to Specified Field

f. Vertical Speed Profile

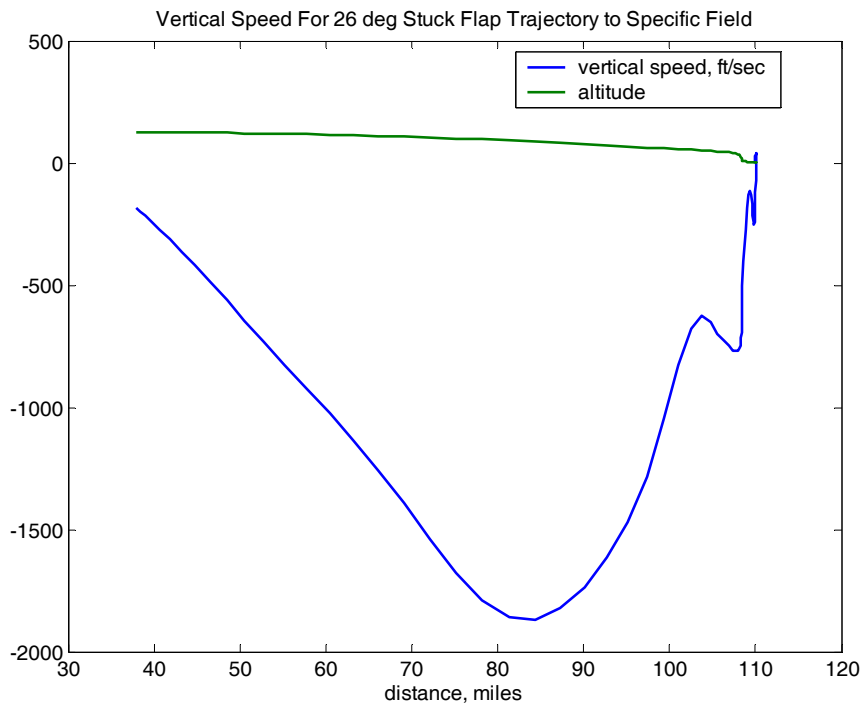


Figure 99 Vertical Speed Profile for Failed Vehicle Trajectory to Specified Field

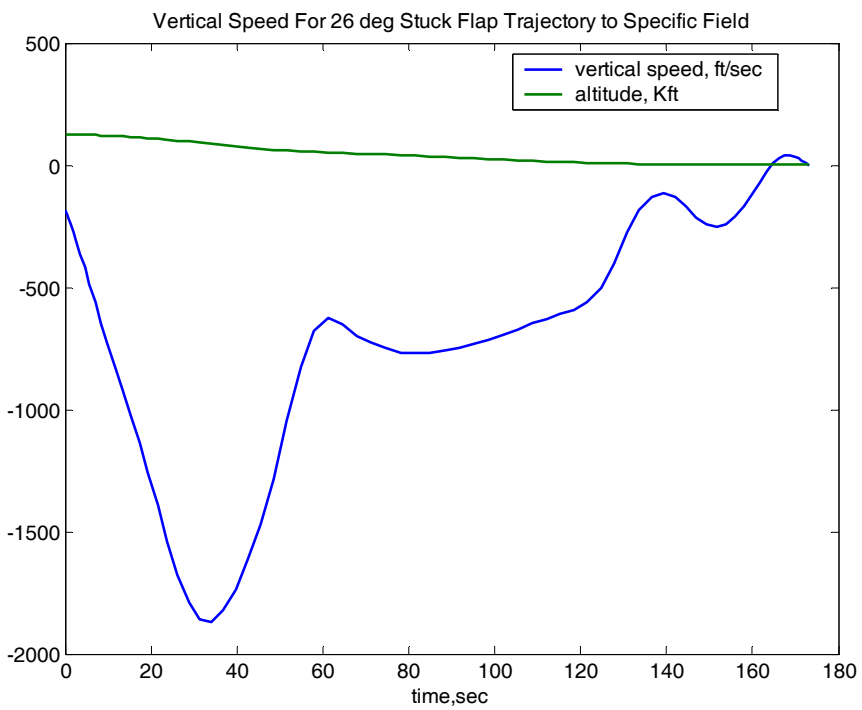


Figure 100 Vertical Speed Profile (vs. time) for Failed Vehicle Trajectory to Specified Field

g. Controls

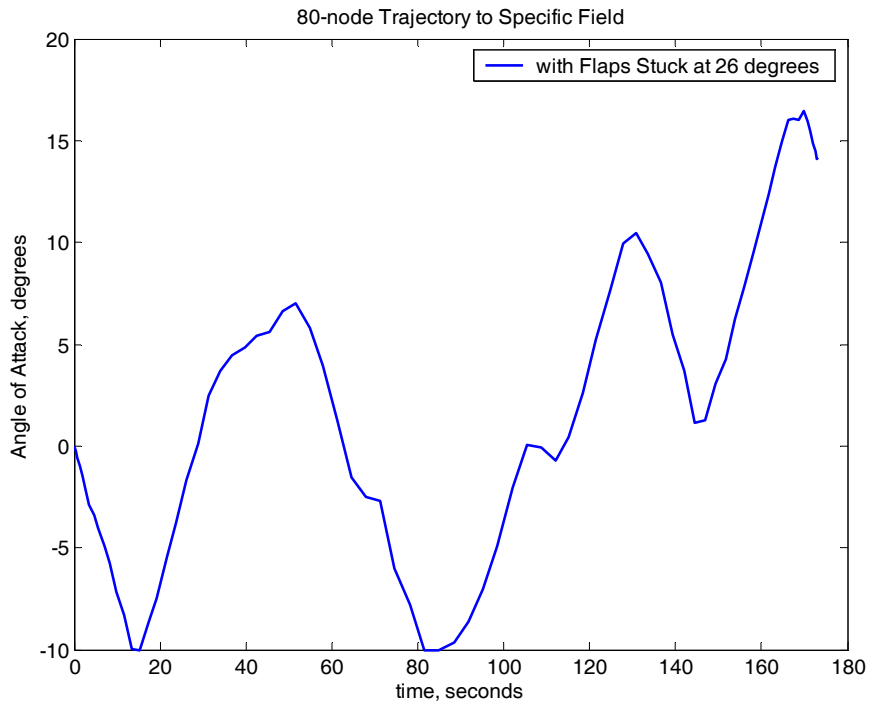


Figure 101 Angle of Attack Profile for Failed Vehicle Trajectory to Specified Field

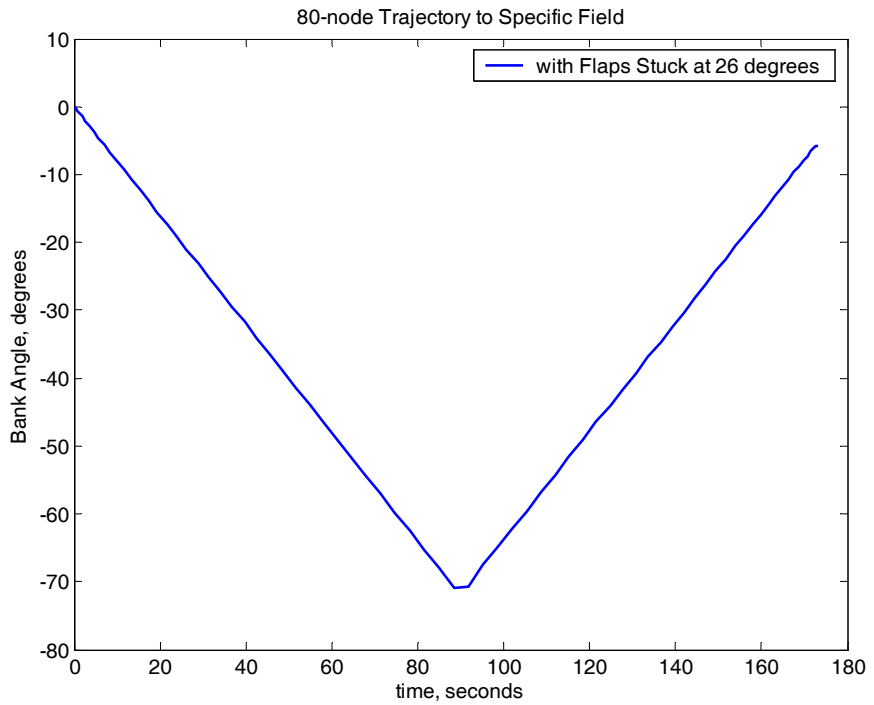


Figure 102 Angle of Bank Profile for Failed Vehicle Trajectory to Specified Field

h. Pseudo Controls

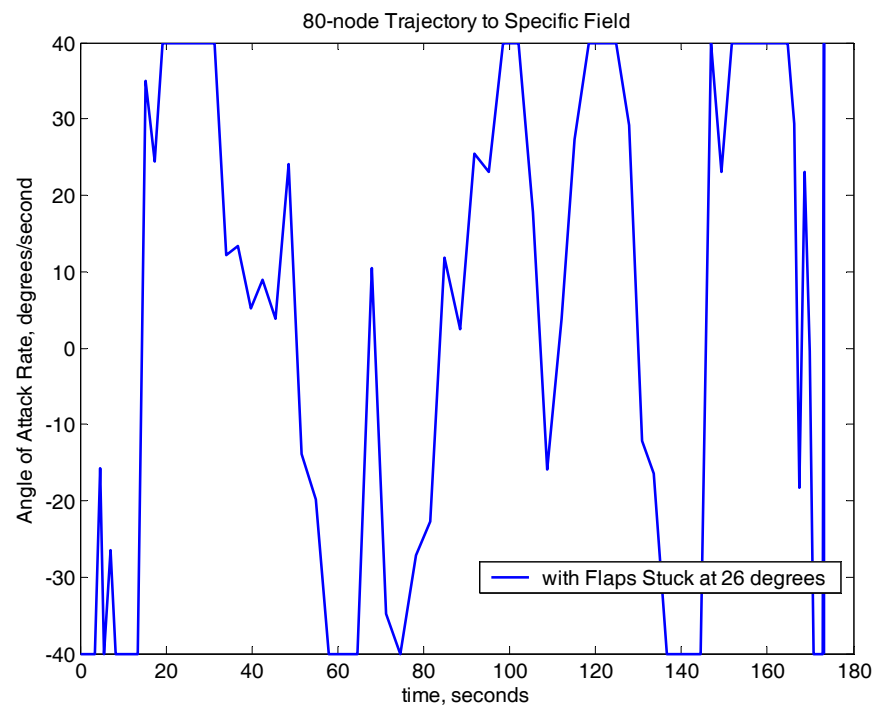


Figure 103 Angle of Attack Rate Profile for Failed Vehicle Trajectory to Specified Field

The bank angle rate profile is nearly bang-bang for this trajectory.

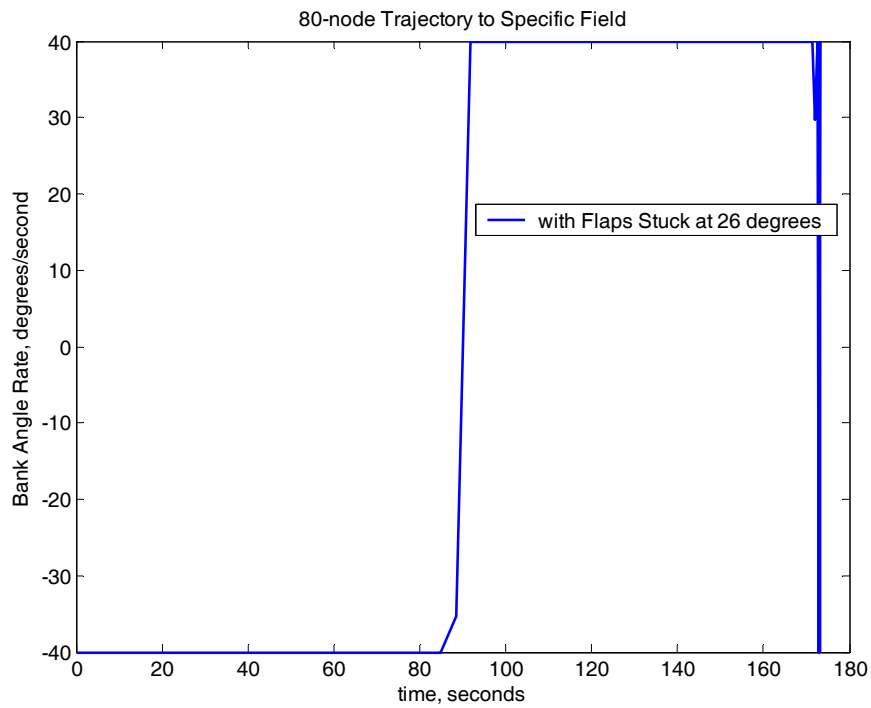


Figure 104 Bank Angle Rate for Failed Vehicle Trajectory to Specified Field

i. Trim Deficiency

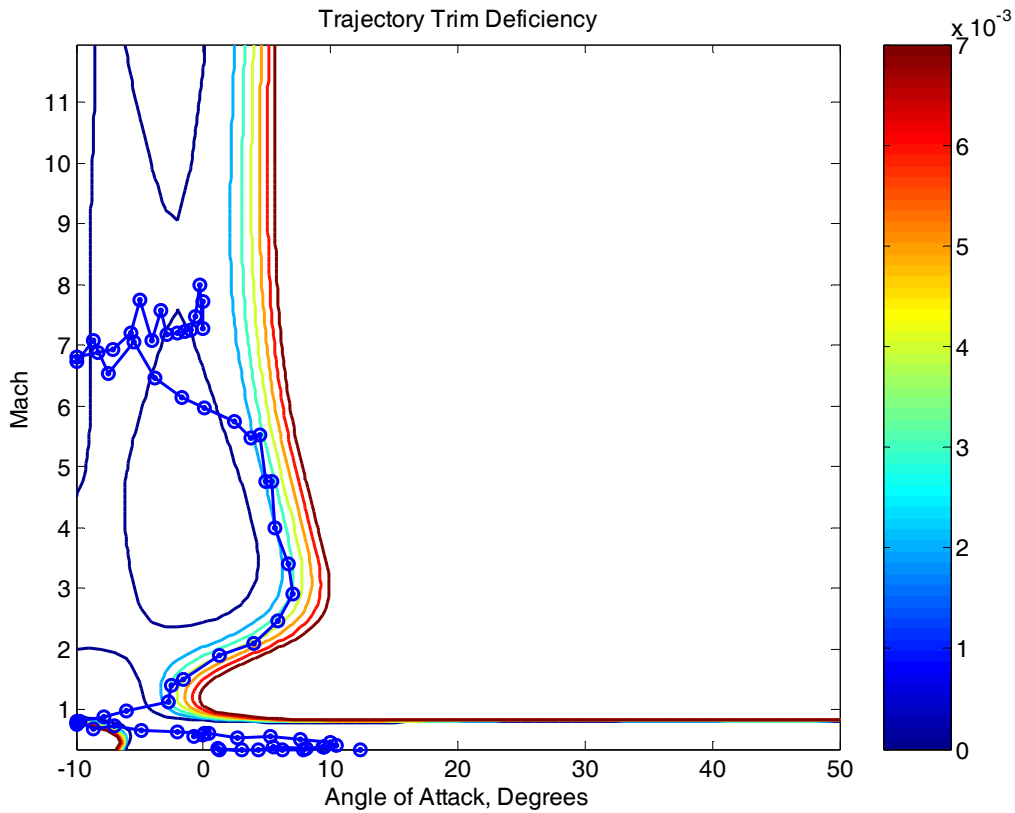


Figure 105 Trim Deficiency Profile for Failed Vehicle Trajectory to Specified Field

The trim deficiency profile illustrates several problems associated with fitting curves to the trim deficiency data. The contour plot of the fitted trim deficiency curve is relatively well behaved except for the low Mach and angle of attack combinations, which is exactly where the trajectory wants to go. For this case, the process of fitting the trim deficiency data has artificially reduced the Mach-alpha envelope available to the trajectory with a corresponding decrease in the performance of the vehicle. There must be sufficient nodes or properly placed knots as previously discussed to cover regions in the trajectory where there is rapidly changing trim deficiencies. While the solutions points do not violate the trim deficiency path constraint as shown below, the trajectory between the points may violate the constraint. This violation can be easily removed with proper problem setup.

```

Columns 1 through 15
 0.0005  0.0004  0.0004  0.0003  0.0002  0.0001  0.0000  0.0001  0.0001  0.0002  0.0004  0.0005  0.0006  0.0003 -0.0008
Columns 16 through 30
-0.0008  0.0002  0.0005  0.0004  0.0001 -0.0002  0.0001  0.0014  0.0025  0.0030  0.0030  0.0030  0.0024  0.0030  0.0030
Columns 31 through 45
 0.0021  0.0022  0.0030  0.0030  0.0030 -0.0020 -0.0033 -0.0013  0.0011  0.0030  0.0030  0.0011 -0.0025 -0.0081
Columns 46 through 60
-0.0145 -0.0182 -0.0201 -0.0278 -0.0412 -0.0591 -0.0806 -0.1083 -0.1281 -0.1283 -0.1106 -0.0766 -0.0514 -0.0352 -0.0412
Columns 61 through 75
-0.0585 -0.0721 -0.0858 -0.0912 -0.0861 -0.0600  0.0002  0.0001 -0.0000 -0.0001 -0.0002 -0.0001 -0.0002 -0.0001 -0.0001
Columns 76 through 80
-0.0000  0.0000  0.0001  0.0001  0.0001

```

Table 2. Numerical Trim Deficiency Constraint Results for 80 nodal Points

j. Optimality Analysis

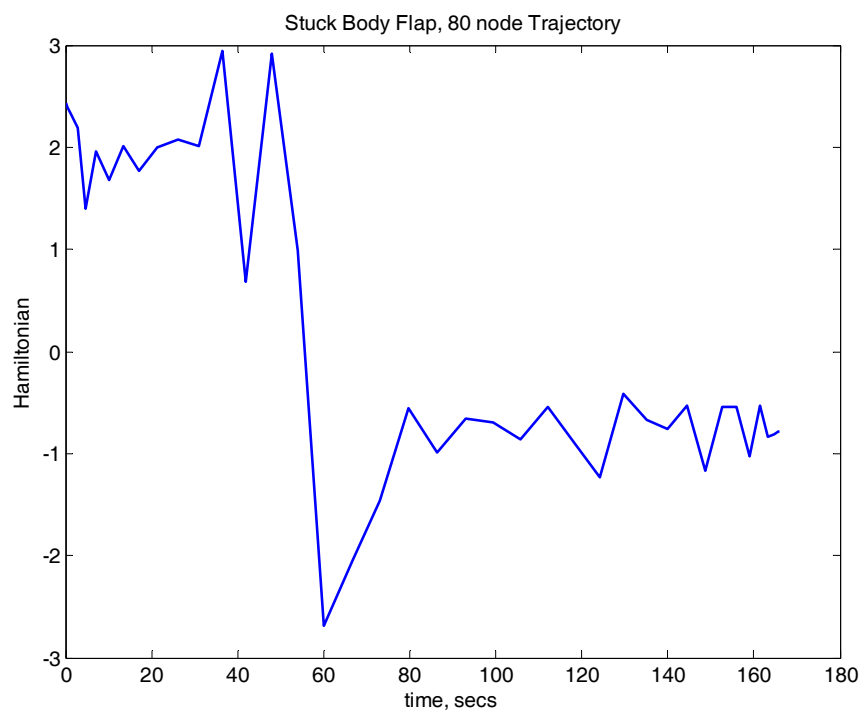


Figure 106 Hamiltonian for Failed Vehicle Trajectory to Specified Field (Flaps Stuck at 26 degrees)

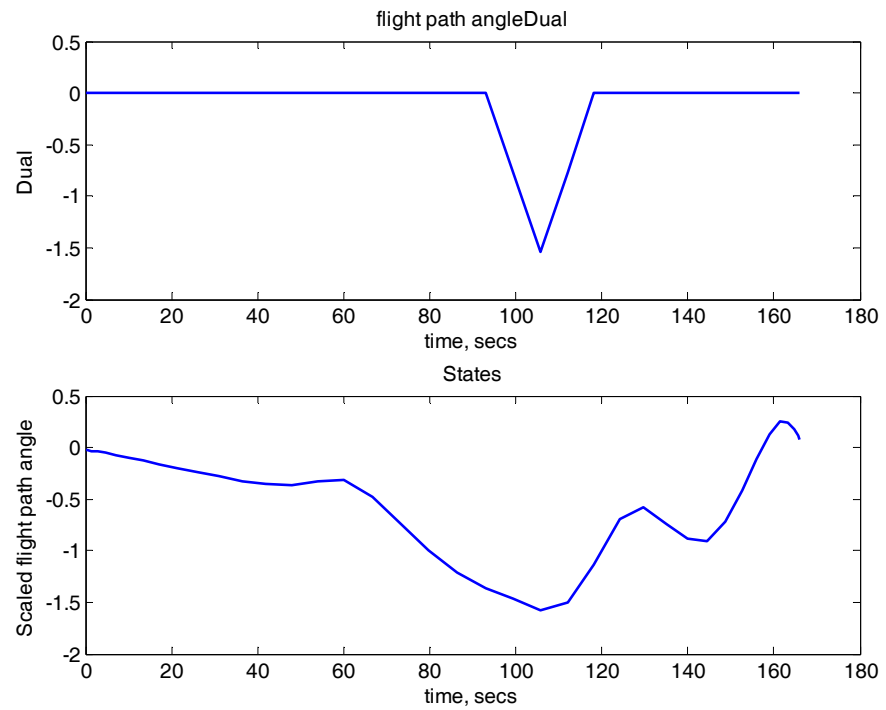


Figure 107 FPA and Associated Dual for Failed Vehicle Trajectory to Specified Field
(Flaps Stuck at 26 degrees)

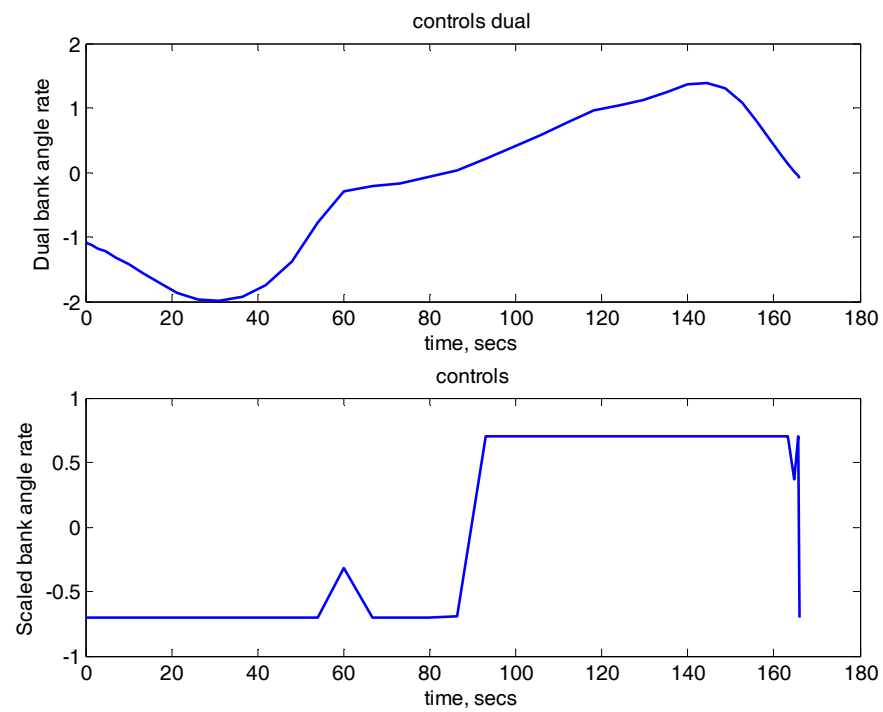


Figure 108 Bank Angle Rate and Associated Dual for Failed Vehicle Trajectory to Specified Field (Flaps Stuck at 26 degrees)

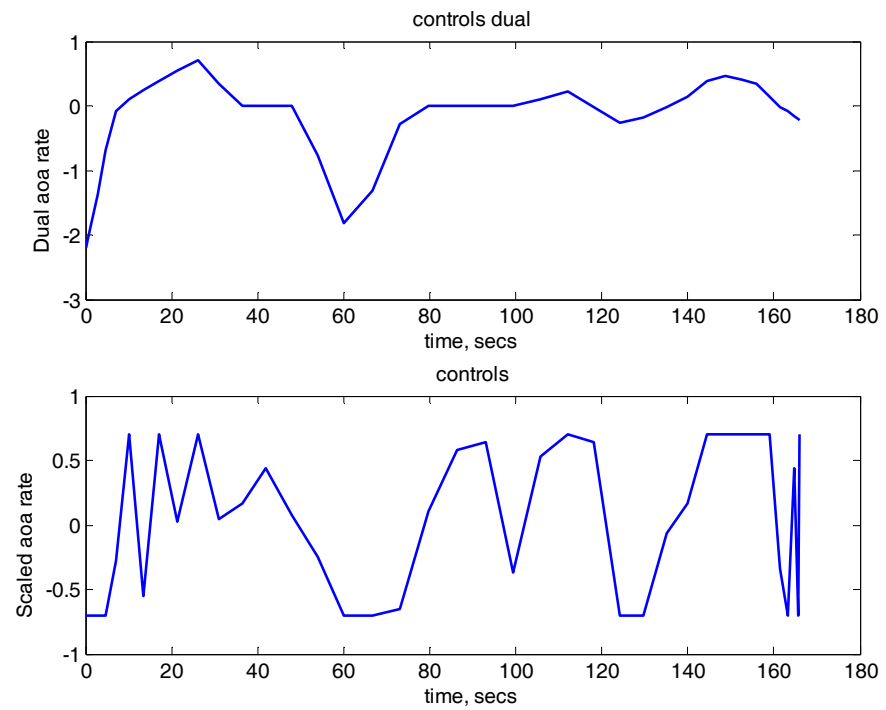


Figure 109 Angle of Attack Rate and Associated Dual for Failed Vehicle Trajectory to Specified Field (Flaps Stuck at 26 degrees)

k. Feasibility Analysis

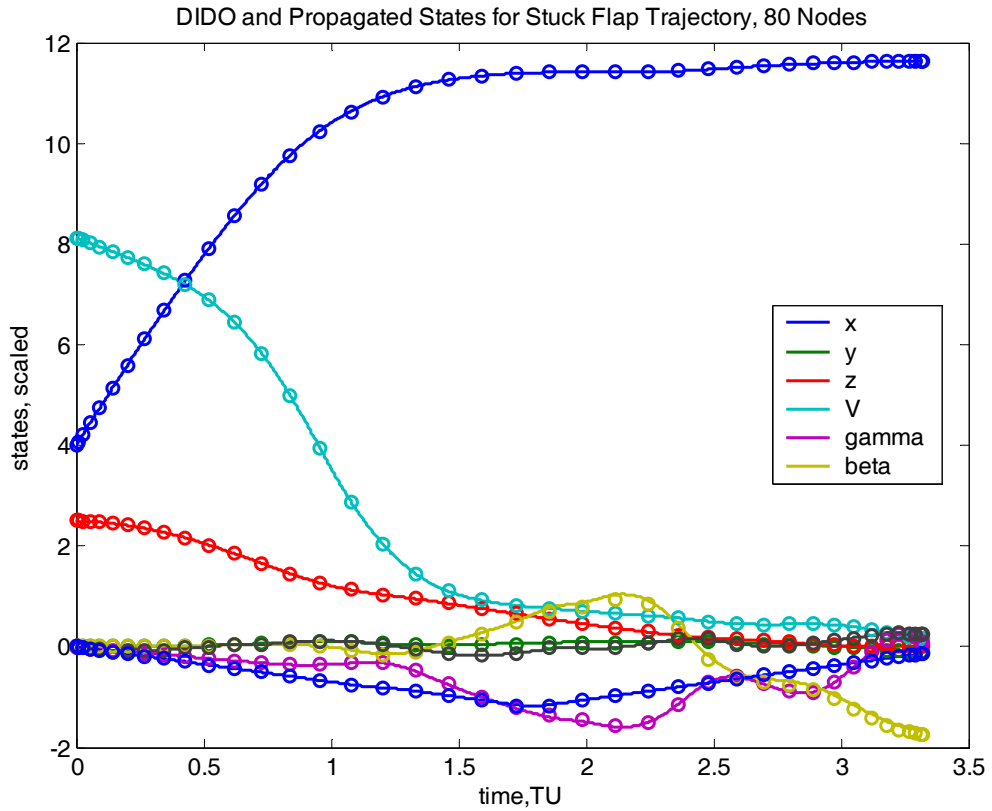


Figure 110 Scaled DIDO and Propagated States, Failed Vehicle Trajectory to Specified Field (DIDO controls are denoted by discrete points)

The error between the DIDO states and the R-K propagated states using the DIDO controls is shown in Figure XX. The altitude error is still high and either the trajectory should be generated using more nodes or the endpoint conditions relaxed

$$\text{Error} = [108\text{ft} \quad 1247\text{ft} \quad -460\text{ft} \quad -01.7\text{ft/sec} \quad -0.8\text{deg} \quad 4.5\text{deg} \quad 0\text{deg/sec} \quad -0.1\text{deg/sec}]$$

D. DIDO PERFORMANCE

While there are several performance criteria for the optimal trajectory solutions, several criteria dominate:

- i. Accuracy of the solution. In other words, how closely do the states at the endpoint set generated by using the propagated solution controls match the internally generated states used by the optimization algorithm.
- ii. Optimality. How optimal is the solution? Examination of the necessary conditions can help answer this question but can be inadequate when attempting to qualify a “near optimal” solution.
- iii. Time to find a solution. Can the solution be found in “real time” and if not, how close to real time can a solution be found?

For the pseudospectral method used in this thesis, all three criteria are a function of the number of nodes used in the solution. Given a feasible solution, the error between propagated and DIDO states can be reduced by increasing the number of nodes. At the same time, increasing the number of nodes in the solution comes at significant expense in computation time. If a locally optimal solution is declared, the end states will not generally change; however, if a “near optimal” solution is declared, then the end states become a function of the number of nodes in the solution. Recall that the generation of a “near optimal” solution is a consequence of many things including insufficient number of nodes and the use of nonsmooth data.

The following analysis provides some insight into the DIDO solution performance for a nominal trajectory with the same initial and endpoint conditions as shown in the results. The graphs represent data from a nominal maximum downrange trajectory. The relationship between propagated errors and number of nodes in the solution is shown in Figure 111 and Figure 112. Notice that the error for low node solutions is unacceptable while the error for solutions greater than 60 nodes results is acceptable.

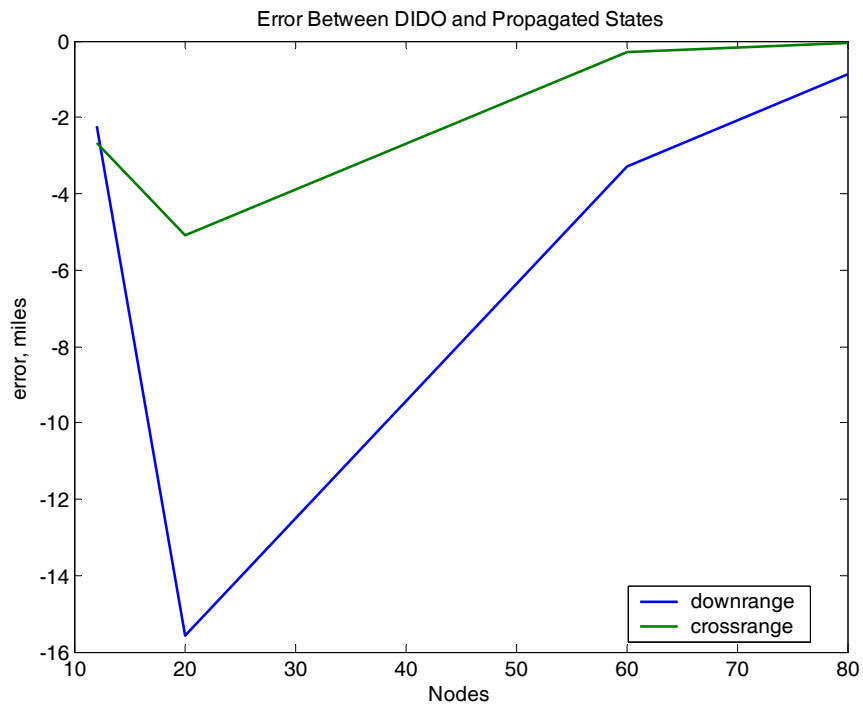


Figure 111 Downrange and Crossrange Error, Nominal Trajectory

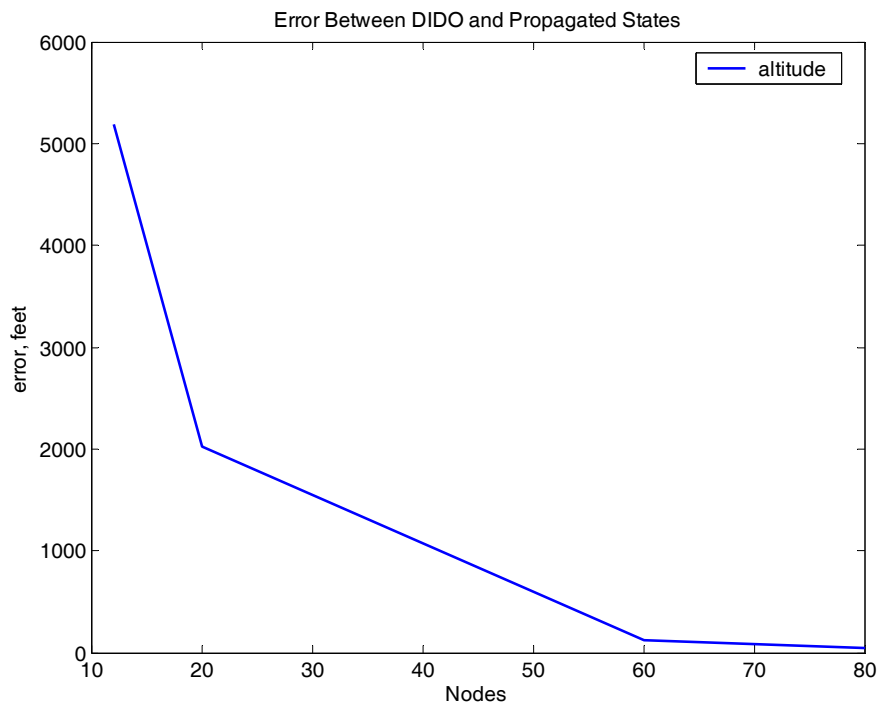


Figure 112 Altitude Error vs. Nodes

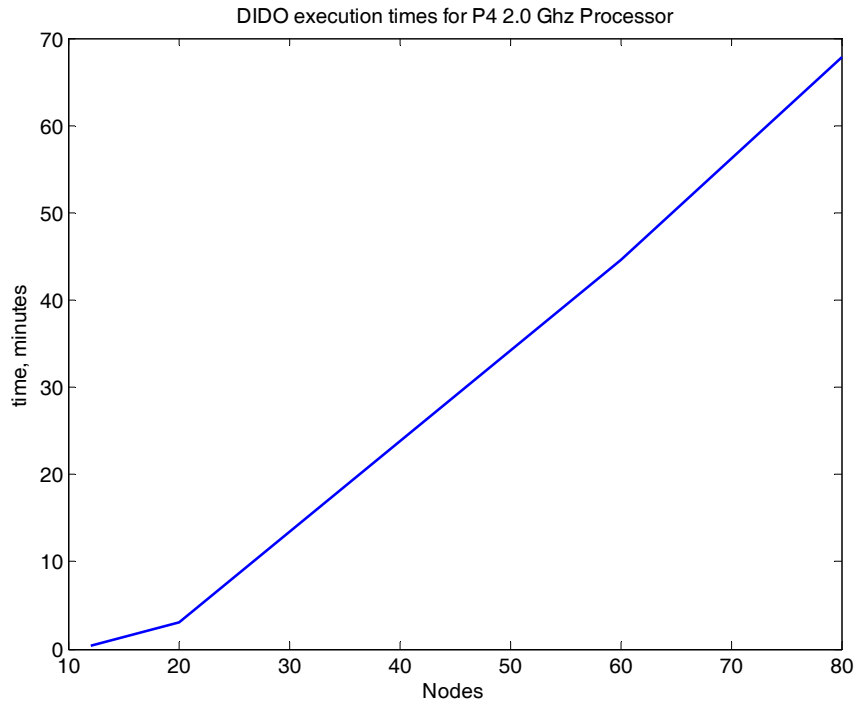


Figure 113 Time to Reach a Solution, Nominal Trajectory for Pentium 4, 2.0 Ghz processor using Windows 2000.

While larger nodes give better propagation performance, the cost is significant. The execution time for an 80-node solution is nearly double that of a 60-node solution. These times were for unoptimized code running on a networked Pentium 4 processor running Matlab 6.0 in a full Windows 2000 environment. Considerable performance increases resulting from speed-optimized code and a faster processor using a dedicated (non-multitasking) computing environment can be expected. Execution times of 70 seconds for 20- node nominal trajectories have been routinely observed on a P4 3.06 Ghz laptop with minimum cpu overhead.

Figure 114 and Figure 115 illustrate the convergence of the “near optimal” solution. Notice that by 60-nodes the final DIDO cross and downrange state variables are nearly identical while altitude convergence is reached immediately. The intent of these graphs is to show the pitfall of choosing a small number nodes to generate faster solutions. The difference between the maximum downrange of a 20 node solution and a 60 node solution is nearly ten miles.

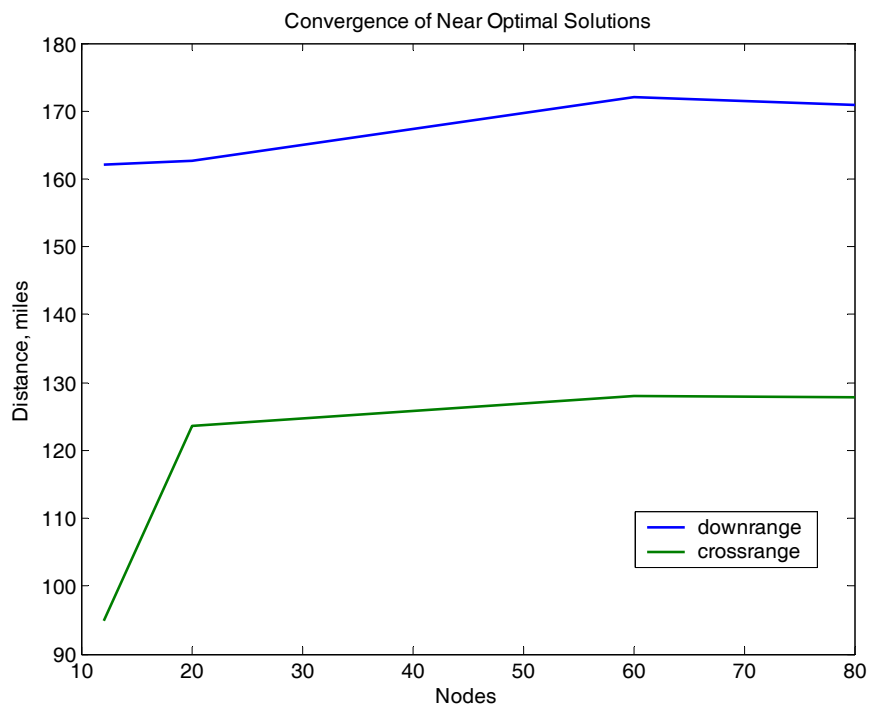


Figure 114 Convergence of Down and Cross Ranges for Near Optimal Solutions

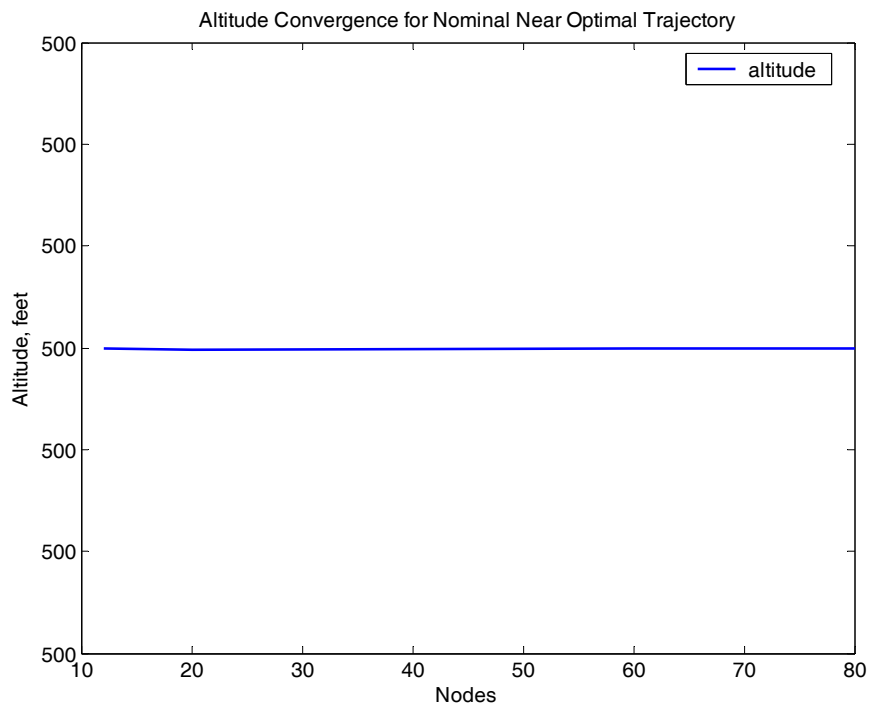


Figure 115 Altitude Convergence for Near Optimal Trajectory

THIS PAGE INTENTIONALLY LEFT BLANK

V. FUTURE WORK

A. CONVERSION TO SI UNITS

This thesis was conducted using the English unit system. The units for velocity, heating rate and pressure do not lend themselves to convenient balancing or scaling. Ross [ref 21] has shown that the use of English units in the problem formulation can result in numerical difficulties leading to infeasible solutions. The metric system is a more intuitive system with all units a subset of the primary distance, mass and time units of meters, kilograms and seconds. Problems formulated using the *mks* system lead to more easily balanced and scaled units with better corresponding numerical results.

B. DATA SMOOTHING

The DIDO software package performance is best with smoothed data that avoids singularities in the gradients of the state variables. The presence of non smooth data results in extremely long calculation times, “near optimal” vice “locally optimal” solutions along with the presence of “sweet spots” where a small range of nodes results in feasible solutions. One way to artificially smooth the data is to increase the number of nodes in the solution; however, the computation penalty can be substantial. The best approach may be to use a more finely meshed lookup C_D and C_L table in the dynamics file. These tables are generated offline and have minor impact on the lookup routine; the extra lookup time is easily offset by the quicker convergence time.

C. TRIM DEFICIENCY MAPPING

The trim deficiency function used in this thesis was a polynomial fitted to the tabular trim deficiency data. This was done to minimize execution time of the solution. The curve fit to the data was not perfect and a better approach may be to use a finely meshed lookup table as discussed in the previous section. This would help automate the trim deficiency process with some penalty in execution time.

D. CLOSED LOOP IMPLEMENTATION

While 80 node solutions can take up to 50 minutes to converge on a Pentium-4 2.0 ghz processor, an optimized code using 40 nodes can achieve convergence in as little as 1 minute on the same machine. While 40-node solutions do not generally provide the necessary accuracy for the endpoints, it may be possible to reduce outer loop execution time using lower order solutions and still meet the accuracy requirements by using feedback. This should be more closely investigated to determine the feasibility of this approach.

E. OPTIMIZING THE DIDO CODE FOR SPEED

The algorithms used in this thesis were constructed with minimal emphasis on computation speed. There are many options available to increase the speed of the algorithm. The first and most significant speed increase can be seen by removing the code from the Windows (multi-tasking) environment and compiling for use on a dedicated real time processor. Additional improvements in the MATLAB code can provide further speed increases; MATLAB 7 shows some speed increase over MATLAB 6.5. As CPU speed continues to increase and the operating code is optimized, execution times should continue to decrease. Additional future improvements to the DIDO software package have the potential of achieving significant decreases in solution times.

F. FULL 6-DOF MODEL WITH INNER AND OUTER LOOP COUPLING

As detailed in the footprint discussion, the decoupled inner and outer loops along with a reduced order model do a satisfactory job of computing the vehicle performance. The true performance of the vehicle; however, is not realized because the two loops are decoupled as illustrated in the differences in the nominal and failed vehicle trajectory footprints. While the use of a 6-DOF model with inner and outer loop may appear to be the more difficult problem to solve, the complex interplay between the dynamical equations and state and path constraints may reduce the problem to one more easily solved. The potential benefits of having a fully integrated inner and outer loop are great enough to warrant further investigation into the feasibility of this approach.

LIST OF REFERENCES

1. "Development of the X-33 Aerodynamic Uncertainty Model", Brent R. Cobliegh, NASA Dryden Flight Research Center, *NASA/TP-1998-206544*
2. "X-33 Hypersonic Boundary Layer Transition", Scott A. Berry, et. al., NASA Langley Research Center, *AIAA 99-3560*.
3. "An Entry Flight Controls Analysis for a Reusable Launch Vehicle", Phillip Calhoun, NASA Langley Research Center, *AIAA 2000-1046*
4. "A Multidisciplinary Performance Analysis of a Lifting-Body-Single-Stage-to-Orbit Vehicle", Paul V. Tartabini, et. al., *AIAA 2000-1045*
5. "X-33, An Educator's Guide with Activities in Math, Science, and Technology", *NASA EG-1999-08-005-DFRC*
6. Spaceflight Dynamics, William E. Weisel, 1989, McGraw-Hill
7. "A Legendre Psuedospectral Method for Rapid Optimization of Launch Vehicle Trajectories", Jeremy R. Rea, MIT Thesis, 2001
8. "Optimization of Low-Thrust Trajectories with Terminal Aerocapture", Scott B. Josselyn, Naval Postgraduate School Thesis. Monterey, CA, 2003
9. Hypersonic Aerothermodynamics, John J. Bertin. AIAA, Washington, DC, 1994.
10. Dynamics of Atmospheric Re-entry, Frank J. Reagan and Satya M. Anandakrishnan. AIAA, Washington, DC, 1993.
11. "Footprint Generation for Reusable Launch Vehicles Using a Direct Psuedospectral Method", F. Fahroo, D. Doman, and A. Ngo, *ACC03-AIAA0007*.
12. Canuto, C., M. Y. Hussaini, A. Quarteroni, and T. A. Zang, *Spectral Methods in Fluid Dynamics*. Springer Verlag, New York, 1988.
13. Gottlieb, D., M. Y. Hussaini, and S. A. Orszag, "Theory and Applications of Spectral Methods," in *Spectral Methods for PDE's*, Philadelphia, PA: SIAM, 1984.

14. Elnagar, J., M. A. Kazemi, and M. Razzaghi, "The Pseudospectral Legendre Method for Discretizing Optimal Control Problems," *IEEE Transactions on Automatic Control*, Vol. 40, No. 10, pp. 1793-1796, 1995.
15. Fahroo, F. and I. M. Ross, " Second Look at Approximating Differential Inclusions," *Journal of Guidance, Control and Dynamics*, Vol. 24, No. 1, 2001, pp. 131-133.
16. Fahroo, F. and I. M. Ross, "Costate estimation by a Legendre Pseudospectral Method," *Journal of Guidance, Control, and Dynamics*, Vol. 24, No. 2, 2001, pp. 270-277.
17. Ross, I. M. and F. Fahroo, "A Direct Method for Solving Nonsmooth Optimal Control Problems," the *Proceedings of the 2002 World Congress of The International Federation on Automatic Control*, Barcelona, Spain, July 2002.
18. "Footprint Generation for Reusable Launch Vehicles Experiences Control Effector Failures", A. Ngo and D. Doman, AFRL/VACA,
19. "A Method for Estimating Control Failure Effects for Aerodynamic Vehicle Trajectory Retargeting", D. Doman, M. Oppenheimer and M Bolender, AFRL Dayton Ohio.
20. L. Pontryagin et al., The Mathematical Theory of Optimal Processes, 1961
21. Ross, I. M. "A Case Study in Solving Optimal Control Problems: Formulations, Solutions and Issues", NASA GRC internal report.
22. Harpold, J.C., and Graves, C.A., "Shuttle Entry Guidance", *Journal of the Astronautical Sciences*, Vol. 27, No. 3, pp. 239-268, Jul-Sep 1979
23. N.X. Vinh, Optimal Trajectories in Atmospheric Flight (Studies in Astronautics), Elsevier, 1981
24. "A Method for Estimating Control Failure Effects for Aerodynamic Vehicle Trajectory Retargeting", D. Doman, et. al.

25. Dennis Jenkins, Space Shuttle, The History of the National Space Transportation System, p2.

26. Internet, NASA Dresden Flight Research Center,
www.dfrc.nasa.gov/Gallery/Photo/x-33/html, last accessed Jul 9, 2004

27. Scott B. Joselyn, "*Optimization of Low Thrust trajectories with Terminal Aerocapture*", Master's Thesis, Naval Postgraduate School, Monterey, CA

28. "Reconfigurable Control Design for the Full X-33 Flight Envelope", M Christopher Cotting, et. al., AIAA-2001-4379.

THIS PAGE INTENTIONALLY LEFT BLANK

INITIAL DISTRIBUTION LIST

1. Defense Technical Information Center
Ft. Belvoir, Virginia
2. Dudley Knox Library
Naval Postgraduate School
Monterey, California
3. AFRL/VACA
Air Force Research Laboratory
WPAFB, Ohio